Circulation du sang dans des architectures microfluidiques : comportements collectifs de particules déformables en écoulement confiné

Zaiyi Shen

Communauté
UNIVERSITÉ Grenoble Alpes

THÈSE

Pour obtenir le grade de

DOCTEUR DE LA COMMUNAUTÉ UNIVERSITÉ GRENOBLE ALPES

Spécialité : **Physique**

Arrêté ministérial : 7 août 2006

Présentée par

Zaiyi SHEN

Thèse dirigée par **Chaouqi MISBAH**

préparée au sein du **Laboratoire Interdisciplinaire de Physique**
dans **l'École Doctorale de Physique de Grenoble**

Circulation du sang dans des architectures microfluidiques: comportements collectifs de particules déformables en écoulement confiné

Thése soutenue publiquement le **11 Mai 2016**,
devant le jury composé de :

Mme. Catherine GHEZZI
DR INSERM, Université Grenoble Alpes, Présidente
M. Christian WAGNER
Professeur, Saarland University, Rapporteur
M. Marc LÉONETTI
HDR, Université d'Aix-Marseille, Rapporteur
Mme. Ying HE
Professeur, Dalian University of Technology, Examinateur
Mme. Sylvie LORTHOIS
DR CNRS, Université de Toulouse, Examinateur
M. Jens HARTING
Professeur, Helmholtz-Institut Erlangen-Nürnberg, Examinateur
M. Chaouqi MISBAH
DR CNRS, Université Grenoble Alpes, Directeur de thèse

Blood flow in microfluidic architectures: collective behaviors of deformable particles in confined flow

Zaiyi Shen

Laboratoire Interdisciplinaire de Physique

Université Grenoble Alpes (Université Joseph Fourier)

A thesis submitted for the degree of

Doctor of Physics

May 25, 2016

Acknowledgements

I would like to express my sincere gratitude to Dr. Chaouqi Misbah for the indispensable guidance, encouragement and support he has provided throughout my research and thesis work. It has been a great pleasure to work with Chaouqi, a smart, supportive, open and friendly advisor, who always offers me all the freedom for my own interests as an independent researcher and also gives me the necessary advice in the forward direction.

I am particularly grateful to Dr. Jens Harting for his guidance on numerics during my stay in Eindhoven, where I enriched my experience in programming. He has been always very patient to answer all my questions.

I also would like to thank my master advisor, Dr. Ying He, who brought me to the academic. Her philosophy has influenced me a lot not only in research but also in life.

I would like to thank the referees of my thesis, Dr. Christian Wagner and Dr. Marc Léonetti for having accepted this task. I also thank the other members of the defense committee, Dr. Catherine Ghezzi, Dr. Sylvie Lorthois, Dr. Ying He and Dr. Jens Harting.

Many thanks to all collaborators. I am indebted to Dr. Badr Kaoui who has shared with me much research experience and very regularly helped me during this period. Dr. Thomas Fischer impressed me by his passion and energy in science at the age of over 70. I thank Dr. Thomas Podgorski and Dr. Gwennou Coupier for having guided me regarding the experimental techniques. Thanks also for many fruitful discussions on the project.

Thanks to Dr. Timm Krüger, for many helpful discussions, and for the 3D simulations. Thanks also to Florian, Maarten, Qingguang and Dennis, for their help about LB3D. Thanks to Vassanti for the advice and assistance on experiments and for the corrections of the French text in the thesis. A very warm thank to Brenna for her careful correction of the thesis manuscript. Thanks to Hengdi, our discussion about numerics really inspires me.

Thanks to many members of Liphy, and especially Alexander, Marine, Yara, Othmane, Hao, Sofia, Mattieu, Weifan, Jocelyn, Philippe, Salima,

Mourad, Nadine, Chantal, Guillaume, Chen, Dongliang, etc ..., during the duration of my PhD, they provided me with a lot of important suggestions and help.

I especially thank Jessie Sitbon. She is the kindest and coolest person. She has helped me a lot not only in administrative part but also in everyday life, when I was starting my life in France.

Finally, I would like to thank all my family members who gave me an atmosphere full of love and encouragement. I am especially grateful to my wife, Yangyang. She is always giving support to me and helps me prepare the French part in the thesis.

I acknowledge the Campus France and CNRS for the finance support.

Abstract

Blood flow in the microcirculation is essential for delivery of nutrients to tissues and organs. To better understand the properties of red blood cell (RBC) flow in microcirculation, this thesis focuses on the collective behaviors of RBCs in confined shear flow and in networks. I) We numerically study the link between spatiotemporal organization of RBC suspension and rheology by using an immersed boundary-lattice Boltzmann method. We show that in a confined blood suspension, RBCs spontaneously organize in a crystal-like structure under the sole effect of hydrodynamic interaction. II) The partition of RBCs at the level of bifurcations is addressed in our computer simulations and in vitro experiments. In the case of extreme hemodilution, our results exhibit a new phenomenon in opposition to the known Zweifach-Fung effect. Finally, the RBC transit is investigated through simulations of a large number of RBCs flowing in a network pattern structured as a honeycomb.

Keywords: blood, self-organization, rheology, network, partition

Résumé

La circulation du sang dans la microcirculation est essentielle pour acheminer des nutriments aux tissus et aux organes. Pour mieux comprendre les propriétés d'écoulement des globules rouges (RBCs) dans la microcirculation, cette thèse se concentre sur les comportements collectifs des RBCs dans un écoulement de cisaillement confiné et dans des réseaux. I) Nous étudions numériquement le lien entre l'organisation spatio-temporelle de la suspension de RBC et la rhéologie en utilisant une méthode de Boltzmann sur réseau combinée à une méthode de frontière immergée. Nous montrons que dans une suspension confinée de sang, les RBCs s'organisent spontanément en une structure cristalline sous le seul effet de l'interaction hydrodynamique. II) La répartition des RBCs au niveau d'une bifurcation est abordée par simulation et en expériences in vitro. Pour des dilutions importantes, nos résultats montrent un nouveau phénomène, en opposition à l'effet Zweifach-Fung. Enfin, le transit de RBC est étudié à travers les simulations d'un grand nombre de RBCs circulant dans un réseau en nid d'abeille.

Mots clés: sang, auto-organisation, rhéologie, réseau, partition

Contents

List of Figures

Chapter 1

Introduction

In this chapter, a brief overview of the human circulatory system is provided in Section 1.1. Introduction of blood components and some illustrations of microcirculatory conditions are presented in Section 1.2 and 1.3, respectively. A brief review of the physics of blood flow in microvessels is provided in section 1.4. Section 1.5 is devoted to the presentation of the main contributions of this thesis.

1.1 Blood flow in circulatory system

The main function of the vascular system is to supply nutrients and oxygen to the tissues and to remove metabolic waste products. Microcirculation plays a central role in these mechanisms. A schematic of the human circulatory system is shown in Figure 1.1. One of the early comprehensive descriptions of blood circulation is due to William Harvey in 1628. A closed vascular system contains arteries, veins and capillaries, where the oxygenated blood is pumped by the left ventricle into the aorta, the first level of the arterial system. A progressively ramified vascular pattern branches off into many major arteries, arterioles and then capillaries, postcapillary venules, veins etc... Microcirculation consists of arterioles, venules and capillaries, where the vital substance exchange takes place. After capillaries, the blood is merged into venules (postcapillary venules) and then into veins. Finally, the major veins bring the blood into the right atrium, then the right ventricle where blood is pumped through the pulmonary circulation, releasing carbon dioxide and wastes, before the re-oxygenated blood is sent back to the left ventricle and the cycle starts again.

Blood flows from arteries to capillaries, experiencing a large spectrum of spatial scales, ranging from centimeters to micrometers. At the scale of an artery, blood flow is often theoretically treated as a homogeneous Non-Newtonian fluid, while at the scale of microcirculation, the individual character of red blood cells (RBCs) must be taken explicitly into account. Since the exchange of oxygen and nutrients

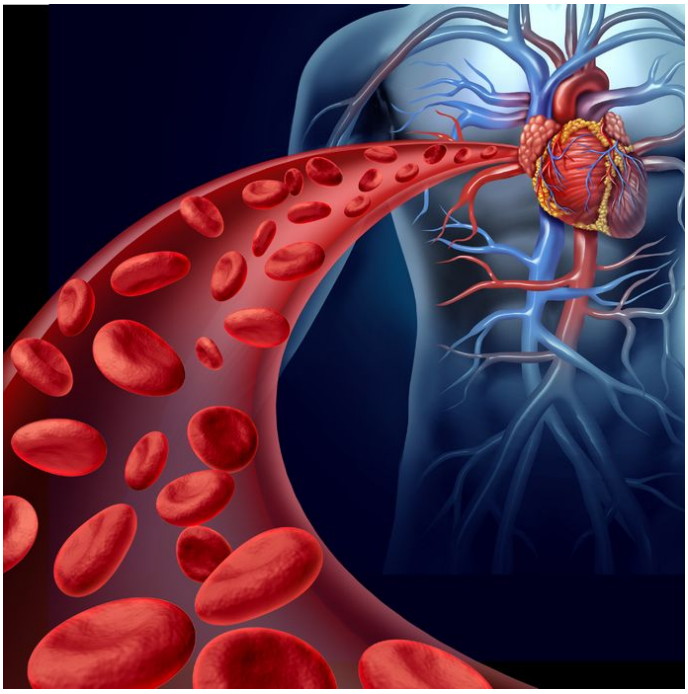

Figure 1.1: A schematic of human circulatory system and RBCs flowing in a vessel. (Picture from http://www.osteopathyny.com/wordpress/wp-content/uploads/2014/06/Blood-Flow.jpg)

takes place in the microvasculature, an abnormal transport of RBCs can have major health consequences. For example, the occurrence of prolonged occlusion zones by RBCs may affect blood vessel perfusion, leading to regression of capillaries, and causing severe diseases, such as induced ischemia [Cokkinos et al., 2006] (tissue deprivation from oxygen leading ultimately to necrosis). The main cause of ischemia is still a matter of debate [Cokkinos et al., 2006]. A possible cause may be related to an endothelial dysfunction. The precise nature of the network (let us say the network topology), as well as the mechanical properties of RBCs, may also affect the perfusion phenomenon, and will be examined in some of our simulations.

Let us also cite some documented facts about the link between the occlusion zones and the nature of RBCs and blood vessels. RBC pathologies, like drepanocytosis (or sickle cell anemia) and malaria, cause variations of RBC shape and deformability, thus presenting serious risks of occlusion. In other diseases, blood vessels can be seriously affected, constituting another potential cause of occlusion. A typical disease is diabetes I, which can affect vessel morphology and mechanical properties[Lorthois and Cassot, 2010]. All of these factors may influence, in a more or less severe way, the flow properties of RBCs with several implications of hematocrit distribution in the vascular network.

As will be seen in this work, the behavior of an even single cell under flow is a complex question, and its understanding will help build the basic blocks regarding blood circulation. An important issue which has known a fundamental focus of the physics, mechanics, and applied mathematics community, concerns the basic understanding of the behavior of individual RBCs under simple flows (such as a linear shear flow and Poiseuille flow) [Abkarian et al., 2007; Fischer et al., 1978; Kantsler and Steinberg, 2006; Keller and Skalak, 1982; Kraus et al., 1996; Misbah, 2006; Noguchi and Gompper, 2004, 2007; Skotheim and Secomb, 2007]. A RBC under a linear shear flow can undergo a tank-treading (the cell orientation is fixed while the membrane undergoes a tank-tread-like motion), vacillating breathing or swinging (the cell orientation oscillates around the flow direction, while the shape shows a breathing behavior), tumbling, and so on. Whether one motion prevails over the others depends on several parameters, like the flow strength, the mechanical properties of the cell, etc... It will be seen here that the nature of the dynamics of a single cell has a strong impact on the collective behavior of the suspension.

1.2 Blood components

Blood is a fluid mainly composed of plasma, RBCs (occupying about half of the volume), white blood cells (WBCs), and platelets, as shown in Figure 1.2. WBCs, platelets and plasma proteins occupy less than 1% of the total blood volume. Blood accounts for 7% of the human body weight with an average density of approximately $1060 kg/m^3$. The average blood volume in an adult human body is about 5 liters. The plasma occupies about 50% of blood volume. The components of plasma are 92% water, 8% plasma proteins and some nutrients and wastes, such as glucose, hormones, carbon dioxide, lactic acid and so on. Albumin is the main protein in plasma, and its function is to control the osmotic pressure of blood.

Figure 1.3 provides a schematic of the main blood cells and their morphologies. The RBCs (also called erythrocytes) are the most abundant cells in blood. The volume fraction of RBC (hematocrit) in the whole blood is about 45%. One microliter of blood contains roughly 5 million RBCs. The typical shape of a healthy RBC is a biconcave disk (approximately) with diameter of $8\mu m$ and thickness of $2.5\mu m$. The RBC membrane encloses hemoglobin, which binds the oxygen from respiratory system and releases it to the tissue when needed. A blood sample observed under a microscope tends to aggregate due to fibrinogen (a plasma protein). The formed aggregation has a rouleaux-like shape and can be reversibly disaggregated by shear forces larger than $1 dyn/cm^2$ [Popel and Johnson, 2005]. The mechanism of aggregation is generally explained by two models. One is based on the assumption that the macromolecules are absorbed on the RBC surface and can thus make the links between neighboring RBCs [Chien and Sung, 1987] (bridging mechanism). The other

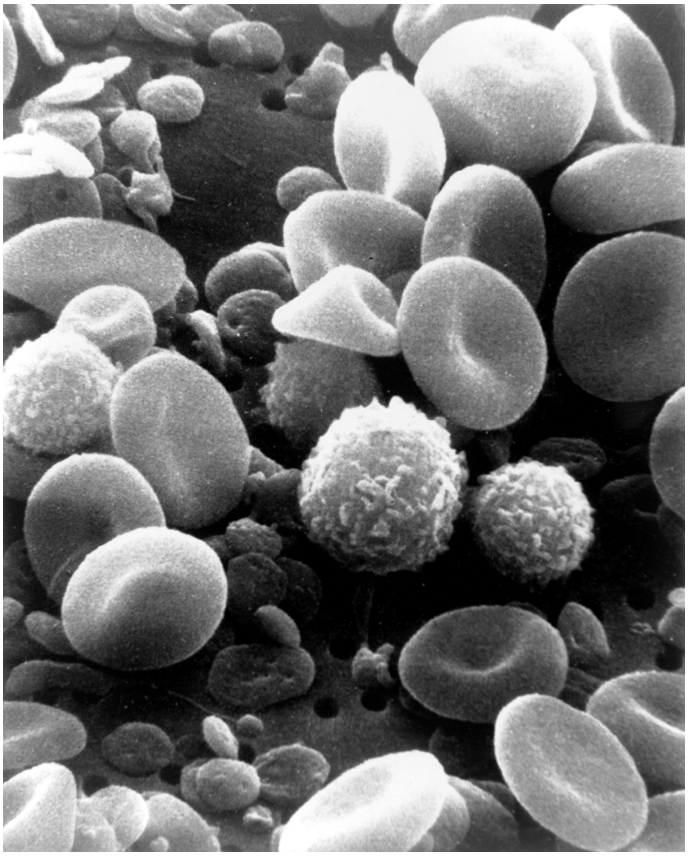

Figure 1.2: A scanning electron microscope image of the main components of blood. It shows red blood cells, white blood cells and platelets. (Picture from https://en.wikipedia.org/wiki/Blood_cell)

proposes that the exclusion of the macromolecules from the fluid gap between two adjacent RBCs leads to an osmotic gradient which presses the RBCs together [Armstrong et al., 2004; Neu and Meiselman, 2002]. While it is often admitted that in the organism rouleaux can be destroyed by shear flow, the situation under microcirculation tends to show the opposite: a physiological concentration of fibrinogen can lead to quite persistent RBCs rouleaux, as shown recently by in vitro experiments and numerical simulations [Brust et al., 2014].

The white blood cells (leukocytes) belong to the immune system. One microliter of blood contains 4000-11000 WBCs. As shown in Figure 1.3, there are typically five kinds of WBCs with different characteristics. In general, the WBC has a spherical shape with a larger size than RBC, approximately $12\mu m$ in diameter. When the WBC is activated by the immune system, it adheres to the endothelial cells, rolls along the vessel wall, and transmigrates the vessel wall to fight infections in the

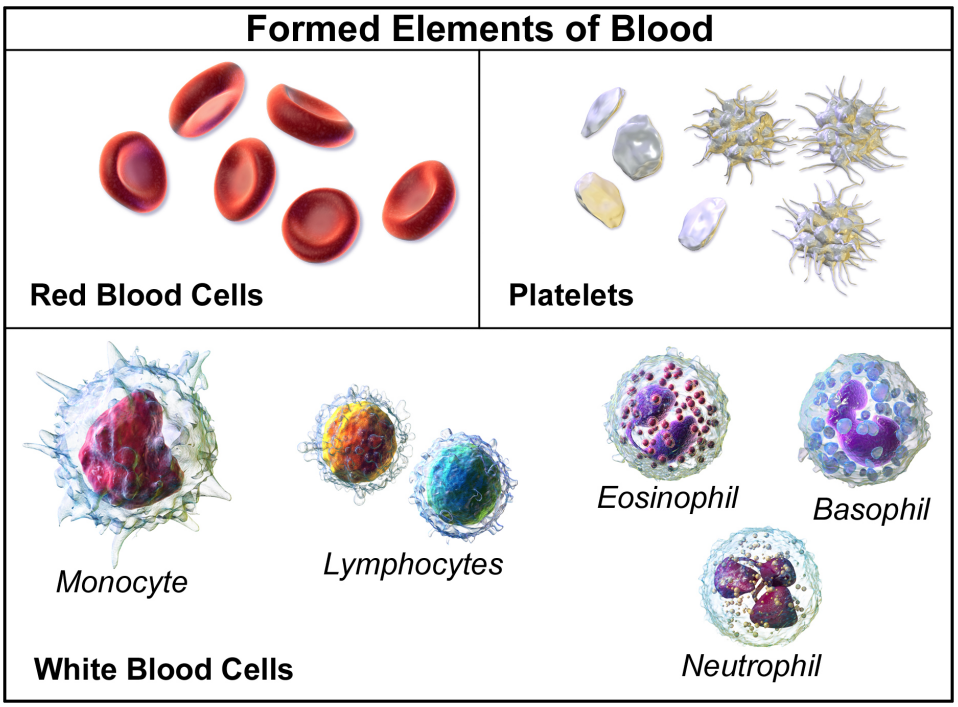

Figure 1.3: A schematic of blood cells: red blood cells, white blood cells and platelets. Red blood cells constitute about 45% of blood volume. The normal RBC has a biconcave disk shape. (Picture from https://en.wikipedia.org/wiki/Blood)

underlying tissues.

The platelets (thrombocytes) take part in blood clotting to stop bleeding. One microliter of blood contains 200,000-500,000 platelets. The inactive platelets have a biconvex discoid shape with a diameter of about $3\mu m$. Once they are activated, several irregular shapes are produced on the surface of the platelet. The platelets can aggregate with each other and adhere to other blood cells and the vessel wall. Besides their intervention in stopping bleeding, platelets can also have undesirable effects, such that they can attach to locally damaged endothelium and elicit thromboembolism.

Since the main components of blood are plasma and RBCs, from a physical viewpoint, we consider in this work that blood can be represented as a suspension of deformable particles for the investigation of the blood flow properties. The plasma, normally, can be treated as a simple fluid. The RBC is modeled as a flexible membrane enclosing a viscous liquid. The volume of a RBC is about $90\mu m^3$ and

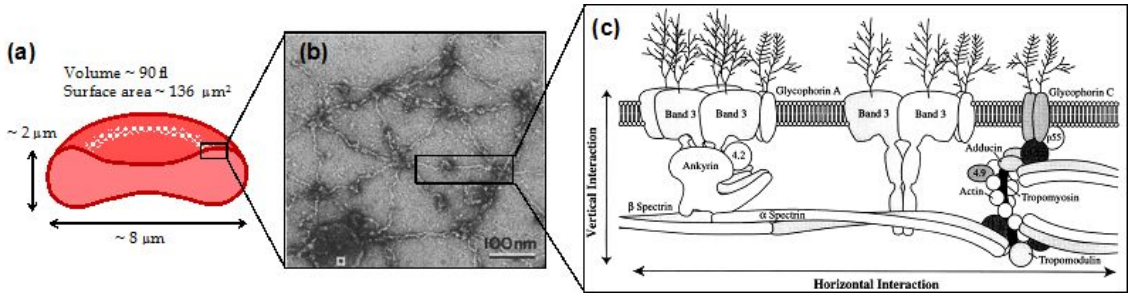

Figure 1.4: A schematic of RBC membrane. (Picture from [Kim et al., 2012])

the surface is about $130\mu m^2$. The internal fluid is basically a hemoglobin solution, which is about 5 times more viscous than the plasma [Skalak et al., 1987; Waugh and Hochmuth, 1995]. As the capillaries have a comparable size to the RBC size, RBCs undergo a strong deformation to squeeze through them. The high deformability of the RBC comes from two factors. (i) The first factor is the biconcave shape, making a small volume to area ratio (reduced volume of normal RBC is about 0.65; see later for a precise definition) and allowing a large deformation, despite the fact that the membrane surface is kept practically constant. (ii) The other factor is the flexibility of membrane. As shown in Figure 1.5, the RBC membrane consists of a lipid bilayer linked with a cytoskeleton (a network of proteins, the spectrin) [Li et al., 2005; Peng et al., 2013]. The lipid bilayer is about $4nm$ in thickness. When compared with the length scale of the RBC size (say its typical radius), the membrane thickness can be ignored, and the membrane can be viewed as a geometrical surface. The membrane resists to bending (bending costs some energy). In addition, the presence of the cytoskeleton [Liu et al., 1987] confers to the membrane resistance against shear elasticity. The RBC membrane is usually modeled as a thin membrane with bending modulus of $2 \times 10^{-19} Nm$ [Discher et al., 1998; Evans, 1983; Scheffer et al., 2001] and a shear modulus of about $4\mu N/m$ [Farutin and Misbah, 2012; Gompper and Schick, 2008]. The RBC membrane also shows a viscous property, and its membrane viscosity plays an important role [Dao et al., 2003; Evans and Hochmuth, 1976; Prado et al., 2015]. In addition, the cytoskeleton can undergo a remodeling in response to shear stress, by separating and reconnecting the lipid layer and cytoskeleton [Li et al., 2007; Park et al., 2010]. The typical dynamics of RBC in simple shear flow is that it tumbles at small shear rates ($< 1s^{-1}$) and tank-treads at larger shear rates ($> 10s^{-1}$) [Schmid-Schönbein and Wells, 1969].

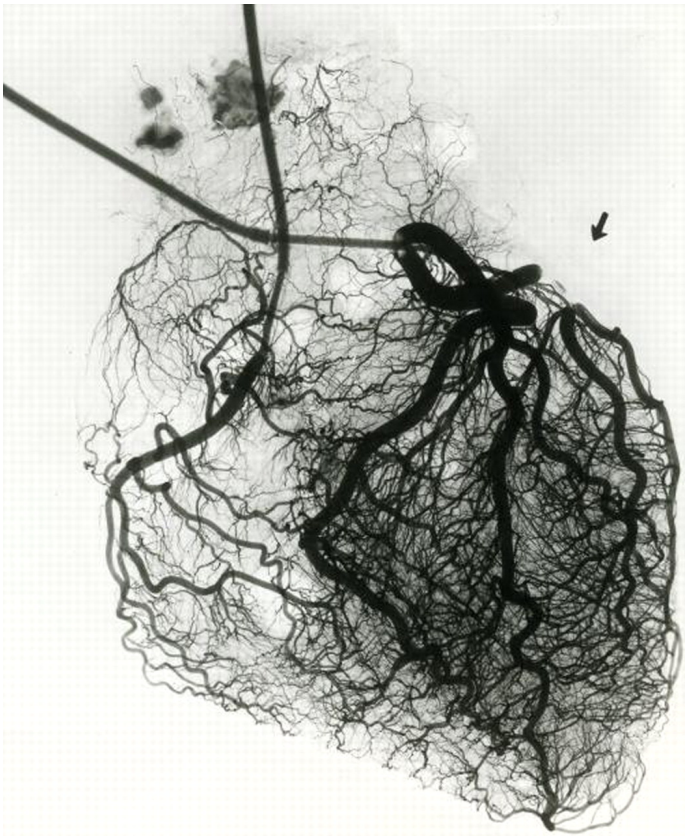

Figure 1.5: Ex vivo arteriogram of a normal human heart showing the microvascular structure. (Picture from [Fulton, 1963])

1.3 Microcirculation

With the advent of optical microscopy in the seventeenth century, Malpighi discovered the capillaries, while van Leeuvenhoek described the complex microvascular morphology. Microcirculation is embedded within organs and tissues and consists of the smallest blood vessels, composed of arterioles, capillaries, and venules. The arterioles are the arterial part of the microcirculation. They are 10-100 μm in diameter. The capillaries have about 4-8 μm in diameter and form complex networks. The venules are 10-200 μm wide, through which blood flows into veins. From aorta to vena, microcirculation bears approximately 80% of the total pressure drop (hemodynamics dissipation) and slows down the blood flow rate. Thus it provides a way to supply nutrients and oxygen to the living tissue.

The arteriole segments exhibit approximately cylindrical configurations. From aorta to capillaries, following the self-similarity, the arterioles branch and form tree-like fractal structures with vessels of decreasing diameter and length. Typically,

the microvascular structures are three dimensional. The architecture regulates the blood flow properties. To satisfy the needs of different organs, such as heart, brain, kidney and so on, the geometries of the vascular network have to comply with these constraints. Figure 1.5 show the microvascular of the heart. The arteriole vessel wall contains vascular smooth muscle, which takes care of the regulation of blood flow in the microcirculation. In a passive way, the increasing pressure dilates the vessel diameter and the decreasing pressure constricts the vessel diameter. In an active way, the vascular muscle can be activated by many factors. Of particular importance is the myogenic mechanism, which acts in the reverse direction as compared to a passive response, in that the vessel diameter constricts when the pressure drops down and dilates when the pressure rises [Popel and Johnson, 2005]. In this way, the blood flow can be maintained nearly constant over a wide enough range of pressure variation. A shear-dependent mechanism [Busse and Fleming, 2003] is also important to regulate the blood flow by reducing the resistance of the vessel through nitric oxide (NO), which is released from endothelium when a rise of shear stress is sensed. Beside these two factors, neural, hormonal and metabolism are also in charge of regulation of blood flow. The internal surface of the blood vessel wall is covered by endothelium, which constitute a periodic wavy surface [Barbee et al., 1994] with approximately $3\mu m$ height fluctuation. This makes the vessel lumen not circular when the vessel diameter is small. When the vessel diameter is constricted, the bulging endothelial cells form a star-shaped cross section of the vessel. These shape adaptations regulated by the endothelium play an essential role in microcirculation.

The capillaries are the smallest vessels of the vascular system. Typically, they are several hundred micrometers in length, about $5\mu m$ in diameter. Abundant capillaries are interconnected in a complex network, which provides a large surface area. These characteristics are beneficial for mass exchange. The capillaries do not have the ability to regulate the flow in an active way, as the arterioles do. This lack of regulation ability is attributed to the absence of smooth muscles. They are made of a thin basement membrane covered internally by an endothelial monolayer. The glycocalyx grows on the endothelial surface and forms a layer on the luminal side with a shear-rate-dependent thickness of about $1\mu m$. The glycocalyx layer takes part in the hemodynamic resistance in capillaries [Lanotte et al., 2012, 2014]. Recently, a back flow at the interface of the glycocalyx layer has been reported [Biagi et al., 2015]. Another prominent property of the capillary wall is the presence of some porous walls, like in the fenestrated capillaries in glomeruli [Deen et al., 2001] or sinusoidal capillaries in lymph nodes, leading to a leakage of the blood flow. The fenestrated capillaries have small pores (60-80 nm in diameter) on the endothelial cells, while the sinusoidal capillaries are not continuous and have large openings [Nagy et al., 2008] (30-40 μm) between the endothelial cells.

The venous network has a structure similar to the arteriolar network, but with shorter, wider and thinner segments. Usually, the venous vessels and arteriolar

vessels are side by side, which is beneficial for the direct exchange between vessels.

1.4 Blood flow in microcirculation

The typical velocity of blood flow in arterioles ranges from $7mm/s$ to $12mm/s$, corresponding to different diameters (from $15\mu m$ to $60\mu m$)[Popel and Johnson, 2005]. The corresponding Reynolds number (measuring the ratio of viscous effects over the inertial effects at the scale of the blood vessel) ranges from 0.03 to 0.2. The Womersley number (which measures the importance of the pulsatile nature of blood flow) ranges from 0.2 to 0.8. These numbers show that inertial effects and the pulsatile nature of blood can not necessarily be safely neglected in the case of arterioles, so these effects must be taken into consideration in the future for a careful study of the flow in arterioles.

The blood velocity in capillaries is quite small, about $0.2mm/s$ [Popel and Johnson, 2005]. The Reynolds number and Womersley number are about 0.0003 and 0.07, respectively. Although venules have a comparable size to arterioles, the blood velocity is much slower due to lower pressure. For example, it is about $0.2mm/s$ and $2.4mm/s$ in the venules with diameters of $18\mu m$ and $72\mu m$, respectively [Popel and Johnson, 2005]. Thus, one characteristic of the blood flow in microcirculation is that both the Reynolds number and Womersley number are small, especially in capillaries. Throughout this work, both inertial and pulsatile effects will be ignored.

As stated above, in the microcirculation (vessels with diameters smaller than $100\mu m$), the discrete nature of blood (suspensions of RBCs) must be taken into account in the flow. In thin tubes, the blood flow shows a blunted velocity profile instead of a parabolic profile (Poiseuille flow). RBCs have the tendency to migrate towards the center, leaving behind a cell-free layer zone. Therefore the RBC velocity (because they migrate towards the center flow line where the velocity is larger) is on average greater than the average blood velocity. If one injects blood from some reservoir into a small tube, there will be fewer RBCs in the tube than in the reservoir, since RBCs move faster than the average blood velocity. Thus the hematocrit in the tube is smaller than that in the reservoir (also called the discharge hematocrit). This effect is known as the Fåhræus effect [Barbee and Cokelet, 1971; Pries et al., 1992]. Because there is a cell-free layer, the blood flow is more efficient than in the absence of that layer. Moreover, since the cell-free layer is reported to be an intrinsic property (its extent does not depend too much on the tube radius), the relative effect of this layer is more important in smaller tubes than in larger ones. Therefore, the smaller tube the blood squeezes in, the better it flows, unless the tube diameter becomes of comparable size to the RBC, in which case blood flow efficiency is reduced. This is the famous Fåhræus-Lindqvist effect: the apparent viscosity of blood in small tube ($< 300\mu m$ in diameter) decreases with decreasing

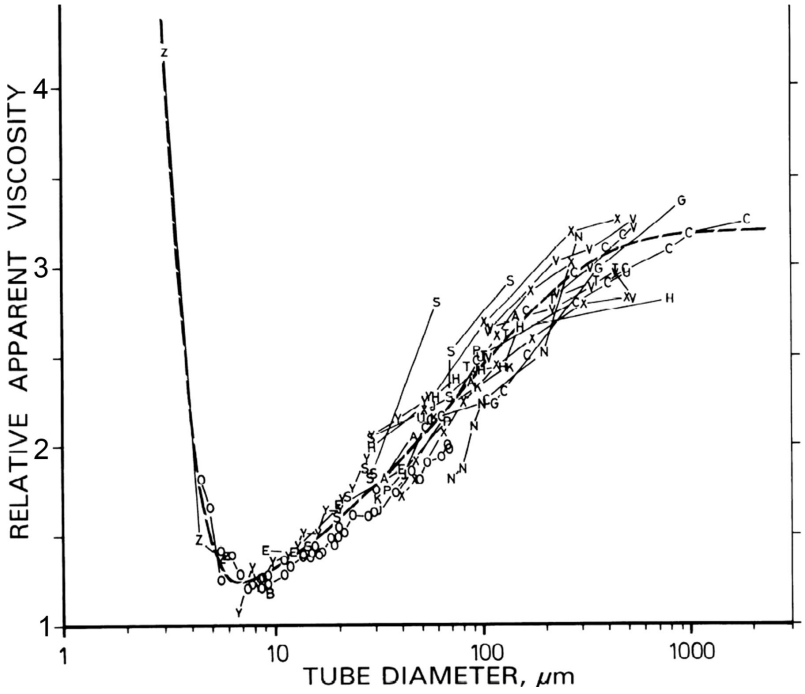

Figure 1.6: Fåhræus-Lindqvist effect. (Picture from [Pries et al., 1992])

diameter [Pries et al., 1992, 1994] (see Figure 1.6).

Another characteristic of microcirculation is the complex vessel network. The principal mechanism that dictates blood heterogeneity in the microvascular networks is the hematocrit partition at the level of bifurcations. RBCs do not behave as passive tracers. Their deformability and dynamics play a decisive role, especially in capillaries, where RBC size is comparable to the size of the capillary. A well known phenomenon in microcirculation is the Zweifach-Fung effect [Dellimore et al., 1983; Fenton et al., 1985; Guibert et al., 2010; Pries et al., 1989]: If we consider a bifurcation, the child branch with the lower flow rate is depleted in RBCs as compared to the parent vessel, while the other, higher flow rate child branch, is enriched. When the flow rate is sufficiently small, the hematocrit in the child branch can even drop down to zero, while it reaches high values in the other branch. The Zweifach-Fung effect results from the existence of a cell-free layer. The feeding flow is divided by a separating streamline into two parts, one feeding the low flow rate branch and the other feeding the high flow rate branch. Due to the cell-free layer, the RBC fraction in the part entering the low flow rate branch is smaller compared to the original RBC fraction in the total feeding flow. The depletion in the low flow rate branch is accompanied by enrichment in the high flow rate branch.

By taking into account the Fåhræus effect, the Fåhræus-Lindqvist effect and the Zweifach-Fung effect, Pries et al. proposed a model based on empirical laws

[Pries et al., 1990], which has been widely used in prediction of blood flow in vessel networks [Huang et al., 2001; Lorthois et al., 2011; Olgac and Kurtcuoglu, 2015]. We shall see in this work that these laws have to be revisited in some flow conditions (see later), since our simulations show a reverse Zweifach-Fung effect.

1.5 Contribution of this thesis

In the past decades, thanks to abundant theoretical, experimental and numerical studies, the dynamics of single RBC in simple flows have been relatively well understood. These results help providing the basic elementary blocks in order to build a fundamental understanding of blood flow properties, and to extract some basic information about the potential implication on physiological functions. Despite the basic progress achieved on single entities, the complex geometries met in reality and the prevalence of many collective phenomena among RBCs, render the understanding of blood flow in microcirculation still a challenging issue. Thanks to the increase of the computational powers during the past two decades, and the development of numerical methods, an interesting field of research regarding a bottom-up approach to blood flow in complex geometries is beginning to emerge. A direct simulation of a large number of RBCs has become possible, which provides an effective way to study the collective behavior of RBCs in complex geometry. In this thesis, a 2D immersed boundary lattice Boltzmann method (developed by myself) has been used in order to investigate the cell-cell and cell-wall interactions in shear flows and in pressure-driven flows in more complex architectures. Due to the 2D nature of the simulations, the notion of shear elasticity in the plane of the RBC membrane looses its meaning, and the vesicle model (a pure phospholipid membrane endowed with a bending elasticity) will be adopted to model a RBC. Thanks to a collaboration with Jens Harting, some 3D simulations have been performed in this thesis, where we have tested the effect of membrane shear elasticity. Several collective behaviors reported here (like rheology in a linear shear flow), will highlight the fact that both the 2D and 3D simulations capture the same essential results. This lends support to our choice of massive 2D simulations at the benefit of strong gain in computational efficiency. It should be kept in mind that we have also performed several simulations in 3D by including the effect of cytoskeleton in the model.

The main contributions of this thesis are directed towards the study of collective behaviors of RBCs in confined shear flow and the distribution of RBCs in complex geometries, where a pressure-driven flow is imposed.

Regarding the collective behavior of RBCs in confined shear flow, the results can be summarized in two parts:

1.5.1 The analysis of hydrodynamic interaction in a shear flow plane (2D) and study of confined rheology

In the first step, we perform numerical simulations in order to study the hydrodynamic interaction between two vesicles in a 2D confined shear flow. In a given flow, we find an equilibrium state of two tank-treading vesicles with constant relative distance, which is regulated by the confinement. In addition, the equilibrium distance increases with the gap between walls following a linear relationship. However, an equilibrium distance between two tumbling vesicles is not observed. Having understood the basic element regarding two body interaction, in a second step, we systematically analyze dynamics and rheology of a suspension of vesicles in a confined shear flow. The combination of the confinement effect and the hydrodynamic interaction, an ordered configuration of tank-treading vesicles is found to be generic, whereas a disordered configuration of tumbling vesicles prevails. Thanks to the ordering, the tank-treading vesicle suspension exhibits a decrease of the normalized viscosity (defined as the difference between the effective viscosity and that of the suspending fluid over the concentration (area fraction in 2D) of the suspension) with increasing concentration. This work is presented in Chapter 3. This work has given rise so far to two publications, one in Physical Review Letters (Thiebaud et al., 2014) and one submitted to Physical Review Fluids (Shen et al., 2016).

1.5.2 The consequence of hydrodynamic interaction between RBCs in 3D

The above ordered structure concerns a 2D suspension, and the question naturally arises of whether order survives in 3D. Suspensions, like emulsions, blood, etc. under shear flow are traditionally viewed as a collection of particles with more or less random positions due to mutual hydrodynamical interactions. By numerical simulations and experiments we show that in a confined blood suspension RBCs spontaneously organize in a crystalline-like structure under the sole effect of hydrodynamic interaction. It is further shown that when RBCs are substituted by rigid particles, order disappears in favor of disorder. Various crystalline orders take place depending on hematocrit and confinement. The intercellular distance of the crystalline structure is a linear function of confinement. Order appears as a subtle interplay between the lift force that pushes RBCs away from walls towards the center and hydrodynamic interactions. This study introduces a new paradigm in the field of dilute non colloidal suspensions where the prevalence of disorder was up until now the rule. This work has given rise to a paper (combining simulations in 3D and experiments) and is to be submitted to Proceedings of the National Academy of Sciences of the United States of America (Shen et al., 2016).

1.5.3 Distribution of RBCs in complex geometry

Two major questions have been analyzed. The first one is dedicated to a simple bifurcation, while the second one treats the case of a complex network.

1.5.3.1 Partition at a bifurcation

After the study of suspension in simple geometry, we directed our work towards complex geometries. A question of major importance in microcirculation concerns the partition of RBCs at the level of bifurcations in the microcirculatory system. We address this problem by using T-shaped microfluidic bifurcations as a model. Our computer simulations and *in vitro* experiments (that I have conducted myself, as well) reveal that the hematocrit (ϕ_0) partition depends strongly on RBC deformability, as long as $\phi_0 < 20\%$ (which corresponds to the normal range in microcirculation), and can even lead to complete deprivation of RBCs in a child branch. Furthermore, we discover a deviation from the Zweifach-Fung effect which states that the child branch with lower flow rate recruits less RBCs than the higher flow rate child branch. At small enough ϕ_0, we get the inverse scenario, and the hematocrit in the lower flow rate child branch is even higher than in the parent vessel. We explain this result by an intricate up-stream RBC organization and we highlight the extreme dependence of RBC transport on geometrical and cell mechanical properties. This work is presented in Chapter 5. This work has given rise to an article which has been published in Microvascular Research (Shen et al., 2016).

1.5.3.2 Perfusion in complex networks

The next natural extension of this work is the study of networks made of many branches in order to analyze the perfusion phenomena at larger scales. We address this problem by simulating the RBCs in a large vessel network with a basic structure of hexagon loops. Our computer simulations reveal that the lateral displacement of RBCs (at the scale of network, not in a given branch) depends strongly on their deformability, as long as hematocrit $\phi < 20\%$ (a normal range in microcirculation), while the cell-cell collisions masks the effect of deformability in the higher hematocrit regime. Furthermore, we discover a deviation of RBC flux in networks as compared to that in straight tubes: in straight channels the flux of rigid RBCs is lower than that of soft RBCs, whereas the opposite happens in the studied network. Finally, diffusion of initially crowded RBCs along the flow direction in the network is analyzed. Rigid RBCs show a faster spreading than soft ones. This work is presented in Chapter 6. This study has given rise to a publication to be submitted to Microvascular Research (Shen et al., 2016).

Chapter 2

Modeling and Materials

This chapter is dedicated to the exposition of the simulation method and the experimental procedure. We first present in Section 2.1 a brief review of various numerical methods used to solve dynamics of RBCs. We then concentrate in Section 2.2 on the method used in this thesis, namely the Lattice Boltzmann method (LBM). Section 2.3 deals with immersed boundary method which is employed to achieve the coupling of fluid flow and RBC membrane interaction. The two dimensional model of RBC used in the present thesis is specified in Section 2.4. The precise numerical procedure is summarized in Section 2.5. In Section 2.6 and Section 2.7, we describe some technical points associated with the numerical method. Equilibrium shapes of vesicles and their dynamics under linear shear flow, tank-treading and tumbling motion, are examined to validate the code in Section 2.8. Finally, a brief introduction of the experimental setup is presented in Section 2.9.

2.1 Current numerical methods of RBC flow simulation

Most theoretical studies of RBC flow are based on numerical approaches. The simulation of the RBC flow is a fluid-structure problem (the structure often referred to is the suspended entity, which is the RBC membrane in the present problem). Many methods have been developed to deal with this problem, however no universal method is available, and each has its own merits and drawbacks. For example, multi-particle collision dynamics is performed by Noguchi et al. to study the dynamics of vesicles [McWhirter et al., 2009; Noguchi and Gompper, 2004, 2005, 2007], dissipative particle dynamics [Pivkin and Karniadakis, 2008] is carried out by Fedosov et al. to investigate the rheology of the RBC suspension [Fedosov et al., 2011b]. Both of them are meshless methods and easy to implement for complex geometries. These methods are akin to molecular dynamics. Another advantage of these two

methods is that the thermal fluctuations of RBC membrane can be naturally taken into account. Other methods, such as level set method and phase field method, are used by Douyex et al. [Doyeux et al., 2011a; Vincent et al., 2012] and Biben et al. [Biben and Misbah, 2003; Biben et al., 2005] to simulate vesicle dynamics in 2D and 3D. These two methods are purely Eulerian. Various fluid solvers, finite difference method or finite element method et al. can be applied with level set and phase field, allowing handling of complex geometries.

Another well adopted method, which enjoys high precision, is the boundary integral method (BIM), which has already been developed in our group for many years and has allowed obtaining a series of fundamental understandings of the dynamics of vesicles in simple flows [Cantat and Misbah, 1999a; Farutin and Misbah, 2011, 2012, 2013, 2014; Ghigliotti et al., 2009, 2010, 2012; Kaoui et al., 2009a,b]. The boundary integral method was used to simulate the capsule deformation in shear flow by Pozrikidis in 1995 [Pozrikidis, 1995]. Many other groups have adopted this method to study vesicles and capsules [Quéguiner and Barthès-Biesel, 1997; Trozzo et al., 2015; Veerapaneni et al., 2009; Zhao et al., 2010]. The principle is to use Green function techniques associated with the Stokes equations where a membrane force (bending and shear elasticity) is localized at the interface. Owing to its high accuracy the BIM has been so far widely adopted to study dynamics of rigid and soft particles in simple flows. The BIM is suitable to perform a simulation of few particles in a free space domain. Because of the integral nature (i.e. nonlocal) the displacement of a given point on the membrane requires the knowledge of the positions of all the discretization points. Hence, the complexity of the algorithm is of the order of n^2 where n is the total number of discretization points. Consequently, the BIM sets severe limitation on computational capacity. The Green function is known explicitly for unbounded flows and in the presence of a single planar wall [Pozrikidis, 1992]. Even in the presence of two straight walls, no explicit form of the Green function is known, but can be expressed in terms of a Fourier integral. The implementation of a Green function for a straight channel has been recently carried out in our group [Thiébaud and Misbah, 2013] and has allowed study of concentrated suspensions [Thiébaud et al., 2014]. When the geometry is complex (like bifurcations) the BIM method is not straightforward, albeit some preliminary results are beginning to emerge.

Another popular way to achieve the coupling of the fluid and membrane is the immersed boundary method (IBM), which has been first proposed by C. Peskin in order to simulate the motion of heart valves [Peskin, 1977]. The principle of IBM is a transfer between a Lagrangian frame (the structure, i.e. the RBC in the present study) and an Eulerian frame (the fluid). Normally, the membrane is described in a Lagrangian frame by following the advection of each membrane point, while the fluid is adequately described in a Eulerian frame. The fluid-structure interaction is accomplished by spreading the force of the membrane to the nearby fluid zones

through a smeared delta function (the force on the membrane acts on the fluids in a band surrounding the membrane; the band follows from the smeared delta function). This force enters the Navier-Stokes equation (NSE) as a body force term, thus the fluid-structure coupling is replaced by solving the NSEs with an additional body force term. The resulting fluid velocities are interpolated back to the Lagrangian system in order to update the membrane positions. The IBM can be combined with any NSE solver in the presence of a body force term, such as finite element techniques, finite differences, etc... A quite popular way for solving the NSEs is the Lattice Boltzmann method (LBM), which has several virtues: (i) very easy to handle complex geometries, such as networks, or even porous media, (ii) its ease of implementation, (iii) its high level of locality regarding parallel computations, and so on.

The use of IBM for deformable capsule simulations has been performed by Eggleton and Popel [Eggleton and Popel, 1998]. Zhang et al. [Zhang et al., 2007] combined the IBM and LBM for the simulation of RBCs. The LBM and IBM are efficient and simple numerical tools but less accurate. LBM lends itself to a relatively easy way to perform complex solid boundaries due to the so called bounce-back condition (see Section 2.2). These properties make the combination of IBM and LBM suitable for our goal, i.e. simulations of a large number of RBCs in complex networks. This thesis uses LBM for the NSEs solver and deals with the fluid-structure interaction by IBM. The description of these two methods are presented in the next two sections.

2.2 Lattice Boltzmann method

LBM was developed from lattice gas cellular automata (LGCA) which was originally introduced by Frisch et al. [Frisch et al., 1986] and by Wolfram [Wolfram et al., 1986]. In LBM, a fluid is treated as a cluster of pseudofluid particles living on a lattice. They collide and spread along discrete directions at each spatial position of the lattice. From another point, the essence of LBM is a numerical way to solve the Boltzmann equation which is based on kinetic theory of gases, but which can allow finding macroscopic properties associated with a continuum medium. In the limit of a small Knudsen number (measuring the ratio of the molecular mean path over the length scale of interest) and small Mach number (ratio of fluid speed to sound speed), the NSEs can be derived from the Boltzmann equation by adopting the Chapman-Enskog analysis [Chen and Doolen, 1998; Krüger, 2012]. The LBM is not a direct solver of the NSEs, but constitutes a good approximation to the NSEs. It is by now widely used in computational fluid dynamics. Actually, the range of application of the Boltzmann equation goes much beyond the NSEs. Indeed, it can be also used to approximate other types of equations, such as advection-diffusion equations [Shan and Doolen, 1996; Wolf-Gladrow, 1995].

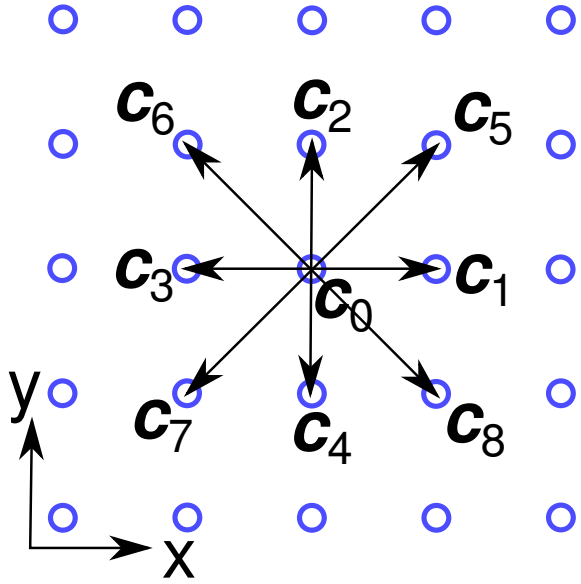

Figure 2.1: D2Q9 lattice model. All the velocity vectors are located in a 2D plane. $\mathbf{c}_{1-4}$ point towards the neighbors along the x and y axes. $\mathbf{c}_{5-8}$ point towards the neighbors along the diagonals. $\mathbf{c}_0$ is zero. The $f_i(\mathbf{r}, t)$ streams in time with velocity $\mathbf{c}_i$ towards the neighbors.

2.2.1 LBGK model

The difficulties in solving the Boltzmann equation come from the complexity of the collision operator. Much work has been carried out on the simplification of the collision operator. The Bhatnagar-Gross-Krook (BGK) approximation is the simplest and most successful model of collision operator. The BGK approximation is to linearize the collision operator based on the idea that all the $f_i(\mathbf{r}, t)$ relax towards a local equilibrium distribution function $f_i^{eq}(\mathbf{r}, t)$ with a constant relaxation time τ. $f_i(\mathbf{r}, t)$ is the distribution function, which is the main quantity in LBM, gives the probability of particles moving with lattice velocity $\mathbf{c}_i$ at position $\mathbf{r}$. The lattice Bhatnagar-Gross-Krook (LBGK) is a discretization for BGK approximation of the Boltzmann equation. The LBGK can recover the Navier-Stokes equations (NSEs) trough a classical analysis in statistical physics, known as the Chapman-Enskog analysis.

A so-called D2Q9 lattice model (2D and 9 lattice velocity vectors) is employed (see Figure 2.1). The choice of 9 points is necessary to recover isotropy of the continuum equations. The time evolution of the distribution function $f_i(\mathbf{r}, t)$ is governed by lattice Boltzmann equation (LBE):

$$f_i\left(\mathbf{r} + \mathbf{c}_i \Delta t, t + \Delta t\right) - f_i\left(\mathbf{r}, t\right) = \Delta t \left(\Omega_i + F_i\right) \tag{2.1}$$

Here Δt is the time step. Ω_i is the collision operator, which is simplified by (BGK) approximation:

$$\Omega_i = -\frac{1}{\tau}\left[f_i\left(\mathbf{r},t\right) - f_i^{eq}\left(\mathbf{r},t\right)\right] \tag{2.2}$$

where τ is a relaxation time and it is related with the kinematic viscosity of the fluid $\upsilon = \frac{1}{2}c_s^2\Delta t\left(2\tau - 1\right)$. $c_s = \frac{1}{\sqrt{3}}\frac{\Delta x}{\Delta t}$ is the local lattice sound speed for D2Q9 model. In this thesis, we set $\Delta x = 1$, $\Delta t = 1$ and $\tau = 1$ (LBM units).

The equilibrium distribution f_i^{eq} is obtained from an approximation of the Maxwell distribution and can be expressed as

$$f_i^{eq} = \omega_i\rho\left[1 + \frac{1}{c_s^2}\left(\mathbf{c}_i\cdot\mathbf{u}\right) + \frac{1}{2c_s^4}\left(\mathbf{c}_i\cdot\mathbf{u}\right)^2 - \frac{1}{c_s^2}\left(\mathbf{u}\cdot\mathbf{u}\right)\right] \tag{2.3}$$

Notice that the collision operator is not really linear since the non-linearity is hidden in $f_i^{eq}(\mathbf{r},t)$.

F_i is the bulk force term in LBE, it can be written as [Guo et al., 2002]

$$F_i = \left(1 - \frac{1}{2\tau}\right)\omega_i\left(\frac{\mathbf{c}_i - \mathbf{u}}{c_s^2} + \frac{\mathbf{c}_i\cdot\mathbf{u}}{c_s^4}\mathbf{c}_i\right)\cdot\mathbf{F} \tag{2.4}$$

where $\mathbf{F}$ is the bulk force term in NSE.

For the D2Q9 model, the nine lattice velocities $\mathbf{c}_i$ and weight factors ω_i are $\mathbf{c}_i = (0,0)$, $\omega_i = 4/9$ for $i = 0$; $\mathbf{c}_i = \left(\cos\left[i-1\right]\pi/2, \sin\left[i-1\right]\pi/2\right)\Delta x/\Delta t$, $\omega_i = 1/9$ for $i = 1,2,3,4$; $\mathbf{c}_i = \left(\cos\left[2i-9\right]\pi/2, \sin\left[2i-9\right]\pi/2\right)\Delta x/\Delta t$, $\omega_i = 1/36$ for $i = 5,6,7,8$.

In the limit of small Mach number and Knudsen number it can be shown that, through Chapman-Enskog expansion, the LBE can recover the incompressible NSEs [Chen and Doolen, 1998; Krüger, 2012]

$$\nabla\cdot\mathbf{u} = 0 \tag{2.5}$$

$$\rho\left(\frac{\partial\mathbf{u}}{\partial t} + \mathbf{u}\cdot\nabla\mathbf{u}\right) = -\nabla p + \mu\nabla^2\mathbf{u} + \mathbf{F} \tag{2.6}$$

The macroscopic quantities can be obtained from f_i. The fluid density is given by

$$\rho = \sum_i f_i \tag{2.7}$$

while the fluid velocity is given by [Guo et al., 2002]

$$\mathbf{u} = \frac{1}{\rho}\sum_i \mathbf{c}_i f_i + \frac{1}{2}\Delta t\mathbf{F} \tag{2.8}$$

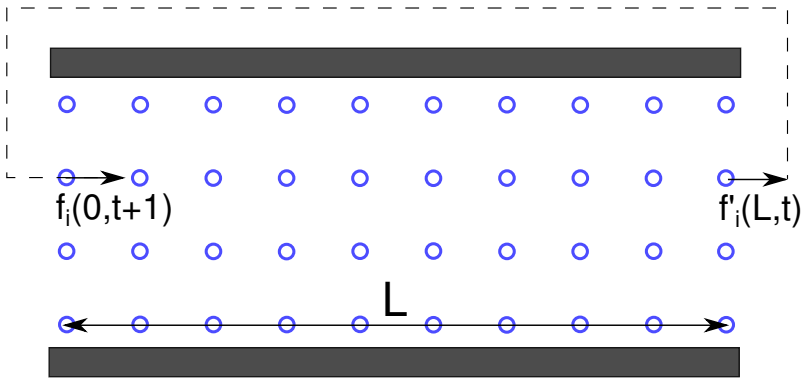

Figure 2.2: A schematic of implementation of periodic boundary in LBM.

and finally the fluid pressure is obtained as $p = c_s^2\rho$. The LBE does not exactly describe an incompressible fluid. However, in the case of sufficient small Mach number and pressure difference, the fluid can be treated as incompressible.

2.2.2 Boundary conditions and initial condition

Since the LBM solves the LBE instead of the NSEs through the evolution of the f_i, all the macroscopic variables for the initial and boundary condition (BC) should be converted in terms of the distribution function. However, unlike the calculation of macroscopic quantities which are directly calculated from the distribution functions, here we want to impose a BC (like the BCs on pressure or velocity) which stems from a macroscopic variable (e.g. pressure) which involves nine values of f_i. Therefore the question amounts, knowing the condition on the macroscopic quantity, how to choose the BCs on these nine variables. This is a challenging issue, since, while transferring information from microdynamics (knowledge of f_i) towards a macroscopic one (pressure, for example) is straightforward, the reverse is far from being true. This issue has been the source of many papers [Chen et al., 1996] devoted to the question of how to implement BCs in the LBM.

We introduce the following BCs in LBM (used in present thesis):

Periodic boundary conditions

The periodic BC is easy to perform in LBM, and states that when the fluid particles leave one side of the computation domain boundary, they enter the domain again from the opposite side of the domain boundary. As en example shown in Figure 2.2, calling the domain length L, the periodic BC can be implemented as

$$f_i\left(0, t+1\right) = f_i'\left(L, t\right) \tag{2.9}$$

The f_i' is called post-collision distribution function. The periodic BC is used for production of the concentrated suspension in this thesis. It should be careful to

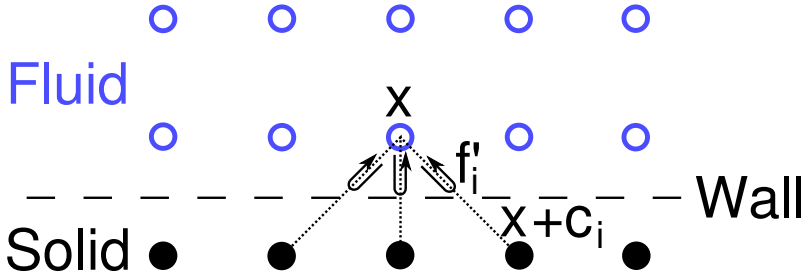

Figure 2.3: A schematic of bounce-back boundary condition in LBM. The wall (dash line) divides the domain into fluid nodes (hollow point) and solid nodes (solid point). For example, the distribution function f_i' of fluid node at $\mathbf{x}$ propagates towards the solid nodes at $\mathbf{x}+\mathbf{c}_i$. It is bounced back to the fluid node $\mathbf{x}$ when it hits the wall.

choose L in order to prevent numerical artefacts.

Bounce-back boundary condition

Bounce-back is a common way to deal with the no-slip boundary at the fluid solid interface. The idea of bounce-back is that the distribution functions are bounced back in the direction they come from when they hit the wall [Ginzbourg and Adler, 1994]. Figure 2.3 shows a process of bounce-back when the wall is located in the middle of fluid nodes and solid nodes. Due to the simple implementation, a complex geometry can be easily handled. A curved boundary is presented by a stepped shape. Therefore a refined bounce-back combined with interpolation is proposed to accurately handle the curved boundary [Bouzidi et al., 2001]. Note that many ways to implement the bounce-back exist, as show in the Figure 2.3. A half-way bounce-back is used in this thesis,

$$f_{i^*}\left(\mathbf{x}, t+1\right) = f_i'\left(\mathbf{x}, t\right) \tag{2.10}$$

here i^* means the direction which is opposite to i. The half-way bounce-back has a second-order accuracy [He et al., 1997]. It is important to emphasize that the wall is at the middle of the fluid nodes and the solid nodes. The half-way bounce-back boundary condition is applied to produce a T-shaped bifurcation in Chapter 5 and a network in Chapter 6.

Zou and He boundary

Zou et al. [Zou and He, 1997] proposed a velocity and pressure boundary condition based on the assumption of bounce-back of the non-equilibrium distribution. As shown in Figure 2.4, take the left edge for example, the distribution functions f_1, f_5 and f_8 are unknown after streaming, for velocity boundary, the velocities at the edge are known, thus the following relations can be obtained

$$f_1 + f_5 + f_8 = \rho - \left(f_0 + f_2 + f_3 + f_4 + f_6 + f_7\right) \tag{2.11}$$

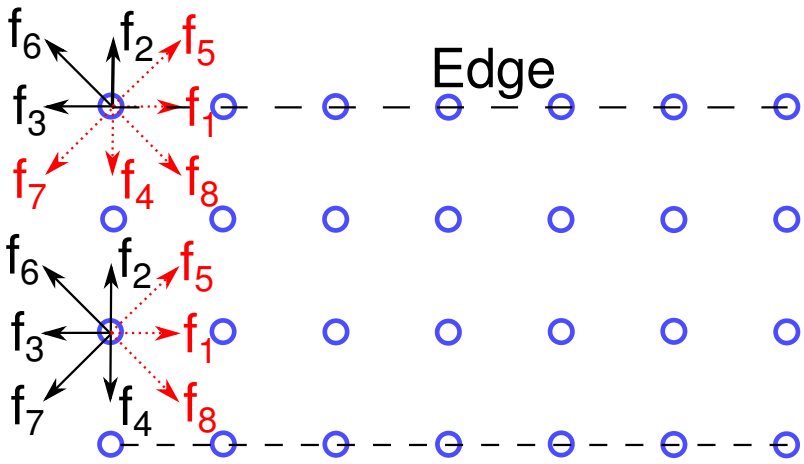

Figure 2.4: A schematic Zou and He boundary in LBM. The unknown distribution functions after streaming are presented by red dot line.

$$f_1 + f_5 + f_8 = \rho u_x + (f_3 + f_6 + f_7) \tag{2.12}$$

$$f_5 - f_8 = \rho u_y + (-f_2 + f_4 - f_6 + f_7) \tag{2.13}$$

There are four unknowns but only three equations, an extra condition from bounce-back of the non-equilibrium distribution is used [Zou and He, 1997]

$$f_1 - f_1^{eq} = f_3 - f_3^{eq} \tag{2.14}$$

Consistency of Equation 2.11 and Equation 2.12 gives

$$\rho = \frac{1}{1 - u_x} \left[f_0 + f_2 + f_4 + 2 \left(f_3 + f_6 + f_7 \right) \right] \tag{2.15}$$

From Equation 2.14, f_1 can be obtained

$$f_1 = f_3 + \frac{2}{3} \rho u_x \tag{2.16}$$

With f_1 known, combining Equation 2.12 and Equation 2.13 we get

$$f_5 = f_7 - \frac{1}{2} \left(f_2 - f_4 \right) + \frac{1}{2} \rho u_y + \frac{1}{6} \rho u_x \tag{2.17}$$

$$f_8 = f_6 + \frac{1}{2} \left(f_2 - f_4 \right) - \frac{1}{2} \rho u_y + \frac{1}{6} \rho u_x \tag{2.18}$$

The corner nodes need some special treatment. Take the top node at the inlet for example. After streaming, only f_2, f_3 and f_6 are known. Because of the no-slip condition the velocity at corner are $u_x = 0$ and $u_y = 0$, the bounce-back of the non-equilibrium distribution are both considered at x and y direction, which yields $f_1 = f_3$ and $f_4 = f_2$. Combined with Equation 2.17 and Equation 2.18, we get $f_8 = f_6$ and $f_5 = f_7$. The density ρ is expected to be constant at the inlet. By taking the value on its neighboring node as ρ, all the variables are known at this stage. With a similar trick, a pressure boundary condition can be carried out. Zou and He boundary condition is second order accurate. The velocity boundary condition will be referred to in order to apply a linear shear flow in Chapter 3 and Chapter 4.

The choice of the initial condition is very important, especially for unsteady flow and in some nonlinear problems where sensitivity to initial conditions has been reported. This is the case for turbulence, multiphase flow and so on. The implementation of initial conditions in LBM is discussed in details in literature [Mei et al., 2006; Skordos, 1993]. In this thesis, the initial condition did not show a significant influence on the results. The main reason is traced back to the absence of unsteady dynamics. The initial condition is fixed by setting the distribution function to the equilibrium value, and accordingly to set the velocity to zero and density to a constant value in all of our simulations.

2.2.3 Selection of parameters in LBM

Here we briefly summarize the selection of parameters based on the examination of the stability, accuracy and efficiency in LBM with LBGK model. More details can be found elsewhere [Holdych et al., 2004; Krüger, 2012].

The conditions set in LBM in order to accurately reproduce the results of NSEs are small Knudsen number and Mach number (Ma) (continuous medium and incompressible flow, respectively). The error in the LBM is proportional to $\mathcal{O}(\Delta x^2) + \mathcal{O}(Ma^2)$ [Krüger, 2012]. The relaxation time τ should be larger than 0.5 to keep numerical stability. However, τ should not be too large. A value of τ larger than 1 deteriorates the quality of accuracy [He et al., 1997]. The LBM is suitable for flows with intermediate Reynolds numbers, approximately from 0.1 to 100 [Succi, 2001]. The high Reynolds number causes instability while the low Reynolds number results in a large computational time.

In the LBM simulation, the parameters are chosen in lattice units. Conversion into physical units will be performed later. For example, for LBGK with D2Q9, the sound speed is fixed to $c_s = 1/\sqrt{3}$. If the fluid is treated as water, the kinematic viscosity and sound speed are about $10^{-6} m^2 s^{-1}$ and $1500 m s^{-1}$. Conversion of LBM units into physical units can be made as follows. Firstly, the Reynolds number in LBM units can be defined as ul/υ (where u,l and υ are velocity, length and

kinematic viscosity, respectively). If we use the same notations with a subscript p (which stands for "physical") for the physical units, we can also write $ul/\upsilon = u_p l_p/\upsilon_p$. Similarly, Mach number reads $u/c_s = u_p/c_{sp}$. Using the above relations, we can write $l_p = (\upsilon_p c_s/\upsilon c_{sp})l$. In LBM, $\upsilon = \frac{1}{2}c_s^2\Delta t\,(2\tau - 1)$, considering stability, τ is always chosen around 1, so that υ can be estimated by taking $\Delta t = 1$. υ_p, c_{sp} are known for water, while $c_s = 1/\sqrt{3}$ is stated above for the D2Q9 lattice. From this information we find $l_p \approx 2.3 \times 10^{-9} l$, which means one lattice length in LBM is approximately equal to 2.3 nm [Narváez et al., 2010]. This clearly raises a numerical problem. Indeed, the typical scale of our physical problem (RBC flowing in a channel) is $10^{-4}m$, which is about five orders of magnitude larger than the physical length of one lattice, meaning a computational domain of about $10^5 \times 10^5$ lattice points is needed in 2D simulation. This exceeds the computer memory capability. To circumvent this difficulty, we have to make some assumptions. i) The numerical Mach number is not necessarily corresponding to the reality. For example, a typical flow velocity in microcirculation is about $1mm/s$, while the sound speed is about $1500m/s$, leading to a huge ratio between sound speed and flow speed, of the order of 10^6. We only require the fluid to be incompressible, a small Ma (< 0.3) is sufficient to maintain the physical essence. The lattice Mach number is usually much larger than in reality, but still less than 0.1 in our simulations. ii) When RBCs flow in the microcirculation, the typical Reynolds number is 0.01-0.1 in arterioles and 0.0001 in capillaries, which leads to that the flow is in the viscous regime and inertia effects are not relevant. For this reason, the lattice Reynolds number for simulation is chosen as large as it is accepted by the small Reynolds number assumption (< 1 in our simulations) for enhancing the efficiency. Thus the Ma and Re are usually not calibrated to reality in our cases, but still are chosen acceptable values so that the inertia and compressibility are not relevant. Giving the lattice length scale (taken to be unity), we have to decide the size of the RBCs in terms of lattice points (depending on the required precision), and this will fix the length scale of interest (in LBM units). The kinematic viscosity in LBM is known, and in order to determine the Reynolds number, we need a velocity scale, which is fixed by the driving force, or by the capillary number. So the capillary number will serve as a way of monitoring the Reynolds number. Once the velocity scale is fixed, we can also determine our Mach number.

If we take the bending elasticity of membrane, for example, the capillary number is defined as $C_a = \mu\dot{\gamma}R^3/\kappa$, meaning the ratio between the membrane relaxation time and shear time associated to the flow $(1/\dot{\gamma})$. κ is the bending modulus of the membrane. In the present thesis, for a RBC flow, a reasonable resolution of the mesh is usually chosen as $l_p = 2 \times 10^{-7} l$ for the simulations in shear flow and $l_p = 5 \times 10^{-7} l$ for the simulations in network by considering the balance of the accuracy and efficiency. Then we can get $Re = \rho C_a \kappa/(\mu^2 R)$ by the definition of Reynolds number as $\rho\dot{\gamma}R^2/\mu$, where we have $\mu = 1/6$, $\rho = 1$ and approximately

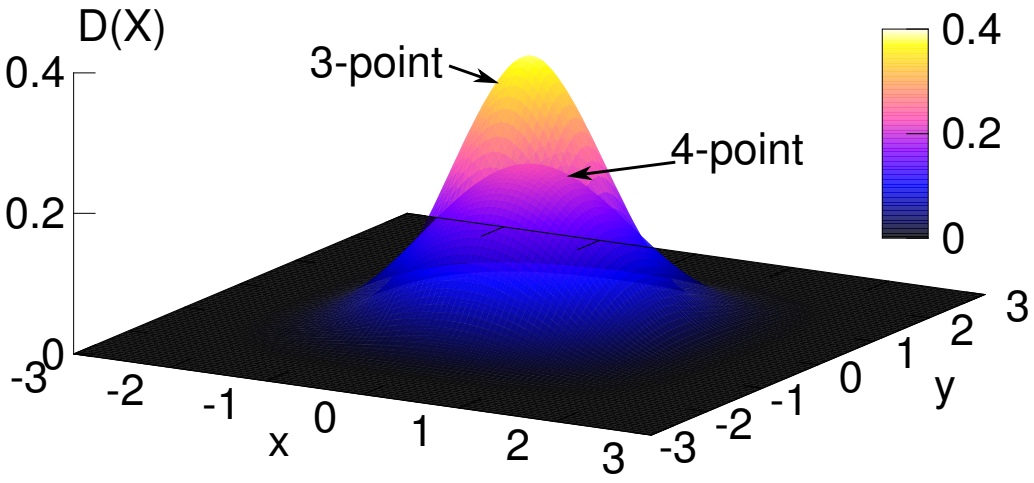

Figure 2.5: The discrete delta function for 3-point scheme and 4-point scheme.

$R = 12$ by using $l_p = 2 \times 10^{-7} l$. Once the capillary number of the problem is fixed, the Reyonlds number can be calculated from the relation $Re = 3\kappa C_a < 1$. C_a is taken to correspond to physical values, and the small Re assumption is satisfied by choosing adequately κ (Re have the order of 0.1 in our simulations).

2.3 Immersed boundary method

The immersed boundary method is employed to deal with the coupling of fluid and RBC in LBM[Kaoui et al., 2011; Zhang et al., 2007]. The IBM was firstly proposed by Peskin and is useful to simulate flexible membranes in fluid flows [Peskin, 2002]. The principle of IBM is a transfer between Lagrangian system and Eulerian system. Normally the membrane is described in Lagrangian system and the fluid is described in Eulerian system. The basic idea is to spread the force of membrane points to nearby fluid points and to interpolate the velocity of membrane points from the nearby fluid points. Instead of dealing with the interface as a geometrical entity (with zero thickness), the fluid-structure interaction is achieved by solving the NSEs in band of width around the interface, in other words, the forces associated with the membrane are rather bulk force. The mathematical derivation of the IBM has been provided by Peskin [Peskin, 2002]. Here we just introduce its numerical implementation in our simulations.

Both the force spreadings and velocity interpolation are achieved by a smeared delta function. The discrete delta function has to obey a list of restrictions which have been given by Peskin. The discrete delta function in 2D is written as

$$D(\mathbf{X}) = \varphi(x)\,\varphi(y)\,, \tag{2.19}$$

where φ is a smeared function that is specified below. It is possible to use various discrete delta functions. The discrete delta function is an important issue in IBM which is related with the numerical accurate and efficiency. The classical and widely used scheme is the cosine function, which is written as

$$\varphi(x) = \begin{cases} \frac{1}{4}\left(1+\cos\left(\frac{\pi x}{2}\right)\right) & |x| \le 2 \\ 0 & 2 \le |x| \end{cases} \tag{2.20}$$

Yang et al. [Yang et al., 2009] developed several smoothed discrete delta functions to suppress the non-physical oscillations of the body forces in moving boundary simulations. A so-called smoothed 3-point scheme is given by

$$\varphi(x) = \begin{cases} \frac{17}{48} + \frac{\sqrt{3}\pi}{108} + \frac{|x|}{4} - \frac{x^2}{4} + \frac{1-2|x|}{16}\sqrt{-12x^2+12|x|+1} & \\ -\frac{\sqrt{3}}{12}\arcsin\left(\sqrt{3}|x| - \frac{\sqrt{3}}{2}\right) & |x| \le 1 \\ \frac{55}{48} - \frac{\sqrt{3}\pi}{108} - \frac{13|x|}{12} + \frac{x^2}{4} + \frac{2|x|-3}{48}\sqrt{-12x^2+36|x|-23} & \\ +\frac{\sqrt{3}}{36}\arcsin\left(\sqrt{3}|x| - \frac{3\sqrt{3}}{2}\right) & 1 \le |x| \le 2 \\ 0 & |x| \ge 2 \end{cases} \tag{2.21}$$

Also a smoothed 4-point scheme is provided by

$$\varphi(x) = \begin{cases} \frac{3}{8} + \frac{\pi}{32} - \frac{x^2}{4} & |x| \le 0.5 \\ \frac{1}{4} + \frac{1-|x|}{8}\sqrt{-4x^2+8|x|-2} - \frac{1}{8}\arcsin\left(\sqrt{2}|x| - \sqrt{2}\right) & 0.5 \le |x| \le 1.5 \\ \frac{17}{16} - \frac{\pi}{64} - \frac{3|x|}{4} + \frac{x^2}{8} + \frac{|x|-2}{16}\sqrt{-4x^2+16|x|-14} & \\ +\frac{1}{16}\arcsin\left(\sqrt{2}|x| - 2\sqrt{2}\right) & 1.5 \le |x| \le 2 \\ 0 & |x| \ge 2 \end{cases} \tag{2.22}$$

The named n-point is related with the interpolation degree. The smoothed 3-point and 4-point discrete delta function are plotted in Figure 2.5. Considering the numerical efficiency and the numerical width of the membrane, the smoothed 3-point is used in our simulations.

The force spreading and velocity interpolation is shown in Figure 2.6. The $\mathbf{x}_f$ denotes fluid points (hollow points in Figure 2.6). Consider the star-marked fluid point for example. The force contributed by the membrane can be collected within the blue square area in Figure 2.6, so that

$$\mathbf{F}(\mathbf{X}_f) = \sum_m D(\mathbf{X}_f - \mathbf{X}_m)\,\mathbf{F}(\mathbf{X}_m) \tag{2.23}$$

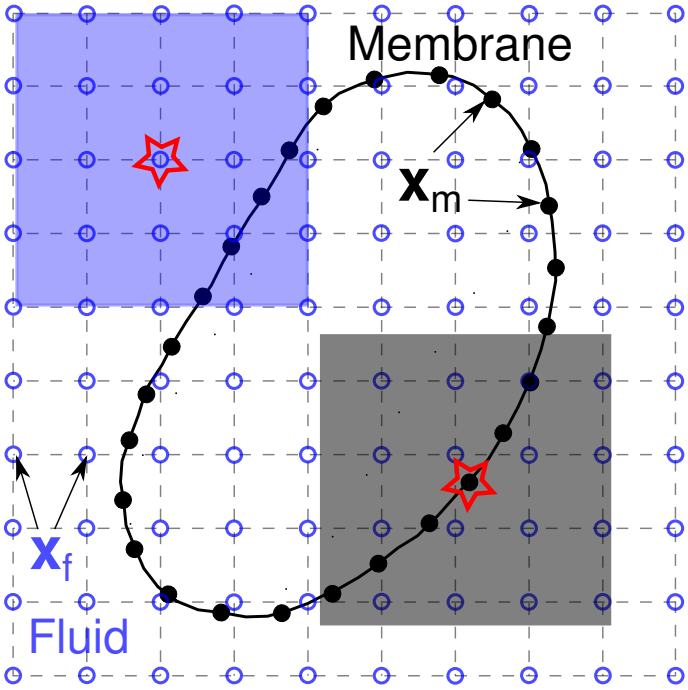

Figure 2.6: A schematic of force spreading and velocity interpolation in the IBM. The fluid is denoted by the hollow points (Eulerian coordinate). The membrane is denoted by the solid points (Lagrangian coordinate).

The $\mathbf{x}_m$ denotes membrane points (solid points in Figure 2.6). Take the star-marked membrane point for example. The velocity on the membrane point can be interpolated from lattice to membrane by taking the fluid points within the gray square area in Figure 2.6

$$\mathbf{u}\left(\mathbf{X}_m\right) = \sum_f D\left(\mathbf{X}_m - \mathbf{X}_f\right)\mathbf{u}\left(\mathbf{X}_f\right) \tag{2.24}$$

The evolution of fluid flow and membrane position is performed alternately with the same time step. Normally the IBM provides a first order spatial accuracy. The ratio between Eulerian mesh resolution and Lagrangian mesh resolution $\Delta X_m/\Delta X_f$ is suggested to be smaller than 1/2 by Peskin [Peskin, 2002] in order to avoid fluid leakage through the membrane. The real value of $\Delta X_m/\Delta X_f$ in our simulations is selected from 0.5 to 1, normally around 0.65. A too large value may cause leakage, while a too small value may cause numerical "stick" since if the Lagrangian mesh is much smaller than the Eulerian mesh, the neighboring points on the membrane get similar velocities [Krüger, 2012]. The numerical stick also happens when two membranes get too close or when the membrane gets close to the solid boundary. The membrane may adhere artificially to each other or on the solid boundary due

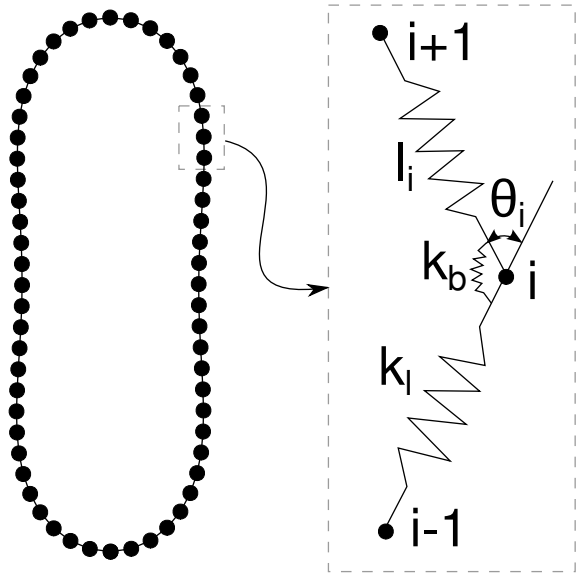

Figure 2.7: The spring model of RBC. The membrane is presented by several points. The neighboring points are connected by a spring. The angle between adjacent springs is also controlled by a spring.

to similar velocities of the two interacting interfaces. A useful way is to refine the resolution of the domain. However, this is done at a certain price: a significant increase of computational time. A repulsive force is added in our simulations in order to keep the distance between two interfaces larger than the interpolation range. This force is given by the the Morse potential [Liu et al., 2004]

$$\Phi(r) = D_e \left[e^{2\beta(r_0 - r)} - 2e^{\beta(r_0 - r)} \right] \tag{2.25}$$

r_0 denotes the repulsion range that is set to 2 lattice lengths in the simulations. The effect of this potential is cut off beyond the repulsion range where the interaction changes sign. Note, in passing, that if we were interested in RBC aggregation we could extend the range of the interaction beyond the repulsion range [Liu et al., 2004]. We must mention that the numerical stick evoked above can be, in principle, removed by introducing the repulsion. However, this is not always obvious. One drawback is that the real effective radius of RBC is made artificially larger, and this might be a source of errors, especially in the highly concentrated suspensions. How to circumvent this problem, is still an ongoing matter for debate in the literatures.

2.4 Model of RBC membrane

Now we will specify the membrane force $F(\mathbf{X}_m)$. In this thesis, a spring model [Tsubota and Wada, 2010; Tsubota et al., 2006] is used for 2D simulations. As shown in Figure 2.7, the RBC is modeled by N membrane points and each point is connected to its neighbors with the potential

$$E_l = \frac{1}{2} k_l \sum_{i=1}^{N} \left(\frac{l_i - l_0}{l_0} \right)^2 \tag{2.26}$$

where k_l is the spring constant, which is set as large as possible in the simulation in order to keep the membrane perimeter constant. l_0 is the equilibrium spring length. To maintain the area of the internal fluid of RBC constant, the following potential is used

$$E_s = \frac{1}{2} k_s \left(\frac{s - s_0}{s_0} \right)^2 \tag{2.27}$$

where k_s is the area constant, and its value is also as large as possible in order to keep the variation of s, the area of internal fluid, small. We define reduced area $\nu = 4\pi s/C^2$. C is the perimeter of the membrane. $\nu = 0.7$ is chosen to get a biconcave shape for RBC in most of our simulations. $s_0 = \nu N^2 l_0^2 / 4\pi$ is the equilibrium area of RBC. The model also contains a bending energy

$$E_b = \frac{1}{2} k_b \sum_{i=1}^{N} tan^2 \left(\frac{\theta_i - \theta_{0i}}{2} \right) \tag{2.28}$$

where k_b is the bending constant and θ_i is the supplementary angle between two adjacent springs. θ_{0i} is the spontaneous angle for the RBC membrane, which is set to 0 in this thesis (for simplicity)[1]. To characterize the flow, we define the capillary number $C_a = \eta_{ext} R^3 \dot{\gamma} / 4 k_b l_0$. $\dot{\gamma}$ is the shear rate of the flow, $R = \sqrt{s_0/\pi}$ is the radius of RBC, η_{ext} is the viscosity of ambient fluid. Normally, C_a is kept at 1 in most of our simulations. With these potentials, we can calculate the force applied on membrane points at each time step by

$$\mathbf{F} = -\frac{\partial (E_l + E_b + E_s)}{\partial \mathbf{r}} \tag{2.29}$$

The force arising from each part of the energy can be presented by the membrane coordinates directly. For example, in Figure 2.8, the derivation of force on the point (x_i, y_i) is given below.

[1] Setting this angle to a nonzero value allows, for example, to induce tank-treading of a tumbling RBC upon an increase of shear rate. Since we are interested in transition phenomena in details, we have decided to keep the number of parameters to a minimum.

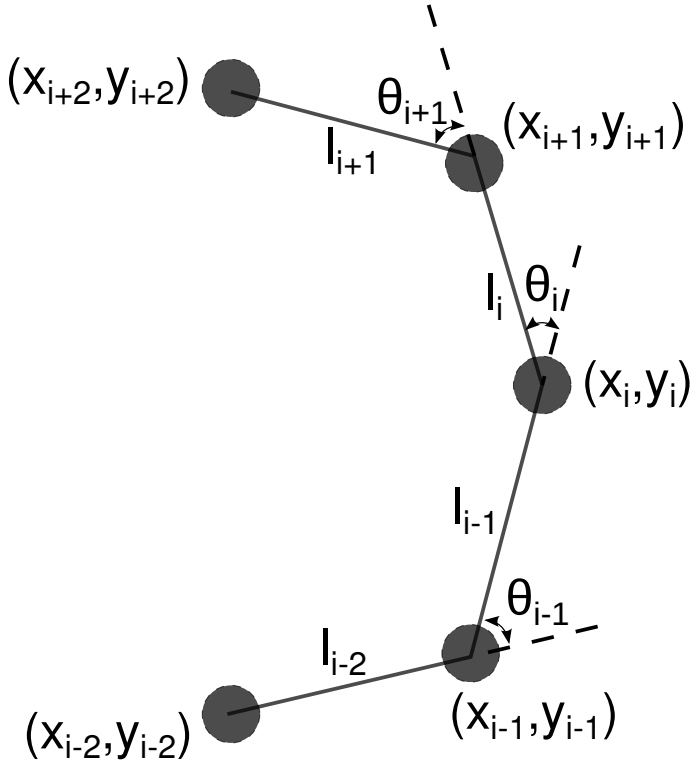

Figure 2.8: A schematic for force calculation in the spring model.

For the stretching energy

$$F_{lx}\Big|_{x=x_i,y=y_i} = -\frac{\partial E_l}{\partial x}\Big|_{x=x_i,y=y_i} = -k_l\frac{l_i - l_0}{l_0^2 l_i}(x_i - x_{i+1}) - k_l\frac{l_{i-1} - l_0}{l_0^2 l_{i-1}}(x_i - x_{i-1}) \tag{2.30}$$

$$F_{ly}\Big|_{x=x_i,y=y_i} = -\frac{\partial E_l}{\partial y}\Big|_{x=x_i,y=y_i} = -k_l\frac{l_i - l_0}{l_0^2 l_i}(y_i - y_{i+1}) - k_l\frac{l_{i-1} - l_0}{l_0^2 l_{i-1}}(y_i - y_{i-1}) \tag{2.31}$$

For the bending energy

$$F_{bx}\Big|_{x=x_i,y=y_i} = -\frac{\partial E_b}{\partial x}\Big|_{x=x_i,y=y_i} = -\frac{k_b}{\left[1+\cos\left(\theta_i-\theta_{0i}\right)\right]^2}\left(\cos\theta_{0i}\frac{\partial\cos\theta_i}{\partial x}+\sin\theta_{0i}\frac{\partial\sin\theta_i}{\partial x}\right)$$
$$-\frac{k_b}{\left[1+\cos\left(\theta_{i+1}-\theta_{0i+1}\right)\right]^2}\left(\cos\theta_{0i+1}\frac{\partial\cos\theta_{i+1}}{\partial x}+\sin\theta_{0i+1}\frac{\partial\sin\theta_{i+1}}{\partial x}\right)$$
$$-\frac{k_b}{\left[1+\cos\left(\theta_{i-1}-\theta_{0i-1}\right)\right]^2}\left(\cos\theta_{0i-1}\frac{\partial\cos\theta_{i-1}}{\partial x}+\sin\theta_{0i-1}\frac{\partial\sin\theta_{i-1}}{\partial x}\right)\Big|_{x=x_i,y=y_i} \tag{2.32}$$

$$\frac{\partial\cos\theta_i}{\partial x}\Big|_{x=x_i,y=y_i} = \frac{x_{i+1}+x_{i-1}-2x_i}{l_i l_{i-1}}$$
$$-\frac{\left(x_{i+1}-x_i\right)\left(x_i-x_{i-1}\right)+\left(y_{i+1}-y_i\right)\left(y_i-y_{i-1}\right)}{l_i^3 l_{i-1}}\left(x_i-x_{i+1}\right)$$
$$-\frac{\left(x_{i+1}-x_i\right)\left(x_i-x_{i-1}\right)+\left(y_{i+1}-y_i\right)\left(y_i-y_{i-1}\right)}{l_i l_{i-1}^3}\left(x_i-x_{i-1}\right) \tag{2.33}$$

$$\frac{\partial\cos\theta_{i+1}}{\partial x}\Big|_{x=x_i,y=y_i} = \frac{x_{i+1}-x_{i+2}}{l_i l_{i+1}}$$
$$-\frac{\left(x_{i+2}-x_{i+1}\right)\left(x_{i+1}-x_i\right)+\left(y_{i+2}-y_{i+1}\right)\left(y_{i+1}-y_i\right)}{l_i^3 l_{i+1}}\left(x_i-x_{i+1}\right) \tag{2.34}$$

$$\frac{\partial\cos\theta_{i-1}}{\partial x}\Big|_{x=x_i,y=y_i} = \frac{x_{i-1}-x_{i-2}}{l_{i-1} l_{i-2}}$$
$$-\frac{\left(x_i-x_{i-1}\right)\left(x_{i-1}-x_{i-2}\right)+\left(y_i-y_{i-1}\right)\left(y_{i-1}-y_{i-2}\right)}{l_{i-1}^3 l_{i-2}}\left(x_i-x_{i-1}\right) \tag{2.35}$$

$$\frac{\partial\sin\theta_i}{\partial x}\Big|_{x=x_i,y=y_i} = \frac{y_{i+1}-y_{i-1}}{l_i l_{i-1}}$$
$$-\frac{\left(x_i-x_{i+1}\right)\left(y_i-y_{i-1}\right)+\left(x_i-x_{i-1}\right)\left(y_{i+1}-y_i\right)}{l_i^3 l_{i-1}}\left(x_i-x_{i+1}\right)$$
$$-\frac{\left(x_i-x_{i+1}\right)\left(y_i-y_{i-1}\right)+\left(x_i-x_{i-1}\right)\left(y_{i+1}-y_i\right)}{l_i l_{i-1}^3}\left(x_i-x_{i-1}\right) \tag{2.36}$$

$$\frac{\partial \sin\theta_i}{\partial x}\Big|_{x=x_i,y=y_i} = \frac{y_{i+1}-y_{i+2}}{l_i l_{i+1}} - \frac{(x_{i+1}-x_{i+2})(y_{i+1}-y_i)+(x_{i+1}-x_i)(y_{i+2}-y_{i+1})}{l_i^3 l_{i+1}}(x_i-x_{i+1}) \quad (2.37)$$

$$\frac{\partial \sin\theta_i}{\partial x}\Big|_{x=x_i,y=y_i} = \frac{y_{i-2}-y_{i-1}}{l_{i-1} l_{i-2}} - \frac{(x_{i-1}-x_i)(y_{i-1}-y_{i-2})+(x_{i-1}-x_{i-2})(y_i-y_{i-1})}{l_{i-1}^3 l_{i-2}}(x_i-x_{i-1}) \quad (2.38)$$

$$F_{by}\Big|_{x=x_i,y=y_i} = -\frac{\partial E_b}{\partial y}\Big|_{x=x_i,y=y_i} = -\frac{k_b}{\left[1+\cos(\theta_i-\theta_{0i})\right]^2}\left(\cos\theta_{0i}\frac{\partial\cos\theta_i}{\partial y}+\sin\theta_{0i}\frac{\partial\sin\theta_i}{\partial y}\right) - \frac{k_b}{\left[1+\cos(\theta_{i+1}-\theta_{0i+1})\right]^2}\left(\cos\theta_{0i+1}\frac{\partial\cos\theta_{i+1}}{\partial y}+\sin\theta_{0i+1}\frac{\partial\sin\theta_{i+1}}{\partial y}\right) - \frac{k_b}{\left[1+\cos(\theta_{i-1}-\theta_{0i-1})\right]^2}\left(\cos\theta_{0i-1}\frac{\partial\cos\theta_{i-1}}{\partial y}+\sin\theta_{0i-1}\frac{\partial\sin\theta_{i-1}}{\partial y}\right)\Big|_{x=x_i,y=y_i} \quad (2.39)$$

$$\frac{\partial \cos\theta_i}{\partial y}\Big|_{x=x_i,y=y_i} = \frac{y_{i+1}+y_{i-1}-2y_i}{l_i l_{i-1}} - \frac{(x_{i+1}-x_i)(x_i-x_{i-1})+(y_{i+1}-y_i)(y_i-y_{i-1})}{l_i^3 l_{i-1}}(y_i-y_{i+1}) - \frac{(x_{i+1}-x_i)(x_i-x_{i-1})+(y_{i+1}-y_i)(y_i-y_{i-1})}{l_i l_{i-1}^3}(y_i-y_{i-1}) \quad (2.40)$$

$$\frac{\partial \cos\theta_{i+1}}{\partial y}\Big|_{x=x_i,y=y_i} = \frac{y_{i+1}-y_{i+2}}{l_i l_{i+1}} - \frac{(x_{i+2}-x_{i+1})(x_{i+1}-x_i)+(y_{i+2}-y_{i+1})(y_{i+1}-y_i)}{l_i^3 l_{i+1}}(y_i-y_{i+1}) \quad (2.41)$$

$$\frac{\partial \cos\theta_{i-1}}{\partial y}\Big|_{x=x_i,y=y_i} = \frac{y_{i-1}-y_{i-2}}{l_{i-1} l_{i-2}} - \frac{(x_i-x_{i-1})(x_{i-1}-x_{i-2})+(y_i-y_{i-1})(y_{i-1}-y_{i-2})}{l_{i-1}^3 l_{i-2}}(y_i-y_{i-1}) \quad (2.42)$$

$$\frac{\partial \sin\theta_i}{\partial y}\Big|_{x=x_i,y=y_i} = \frac{x_{i-1}-x_{i+1}}{l_i l_{i-1}} - \frac{(x_i-x_{i+1})(y_i-y_{i-1})+(x_i-x_{i-1})(y_{i+1}-y_i)}{l_i^3 l_{i-1}}(y_i-y_{i+1}) - \frac{(x_i-x_{i+1})(y_i-y_{i-1})+(x_i-x_{i-1})(y_{i+1}-y_i)}{l_i l_{i-1}^3}(y_i-y_{i-1}) \quad (2.43)$$

$$\frac{\partial \sin\theta_i}{\partial y}\Big|_{x=x_i,y=y_i} = \frac{x_{i+2}-x_{i+1}}{l_i l_{i+1}} - \frac{(x_{i+1}-x_{i+2})(y_{i+1}-y_i)+(x_{i+1}-x_i)(y_{i+2}-y_{i+1})}{l_i^3 l_{i+1}}(y_i-y_{i+1}) \quad (2.44)$$

$$\frac{\partial \sin\theta_i}{\partial y}\Big|_{x=x_i,y=y_i} = \frac{x_{i-1}-x_{i-2}}{l_{i-1} l_{i-2}} - \frac{(x_{i-1}-x_i)(y_{i-1}-y_{i-2})+(x_{i-1}-x_{i-2})(y_i-y_{i-1})}{l_{i-1}^3 l_{i-2}}(y_i-y_{i-1}) \quad (2.45)$$

For the incompressibility of membrane enclosed area

$$F_{sx}\Big|_{x=x_i,y=y_i} = -\frac{\partial E_s}{\partial x}\Big|_{x=x_i,y=y_i} = -\frac{1}{2}k_s\frac{s-s_0}{s_0^2}(y_{i+1}-y_{i-1}) \quad (2.46)$$

$$F_{sy}\Big|_{x=x_i,y=y_i} = -\frac{\partial E_s}{\partial x}\Big|_{x=x_i,y=y_i} = -\frac{1}{2}k_s\frac{s-s_0}{s_0^2}(-x_{i+1}+x_{i-1}) \quad (2.47)$$

2.5 Numerical procedure

LBM is performed in two stages, called collision and streaming. The IBM also has two steps called force spreading and velocity interpolation. The details of the procedure for the combination of IBM and LBM is briefly described below.

1. Initialize the distribution functions $f_i(\mathbf{x}_f, 0)$, the positions of RBCs $\mathbf{x}_m(0)$ and the solid boundaries.

2. At time step t, the RBC positions $\mathbf{x}_m(t)$ are known . The forces on membrane $\mathbf{F}(t)$ can be calculated from the knowledge of $\mathbf{x}_m(t)$, as given above by the RBC model.

3. Spread the $\mathbf{F}(t)$ to the nearby fluid nodes.

4. Do collision in the LBM, get the distribution $f_i'(\mathbf{x}_f, t)$.

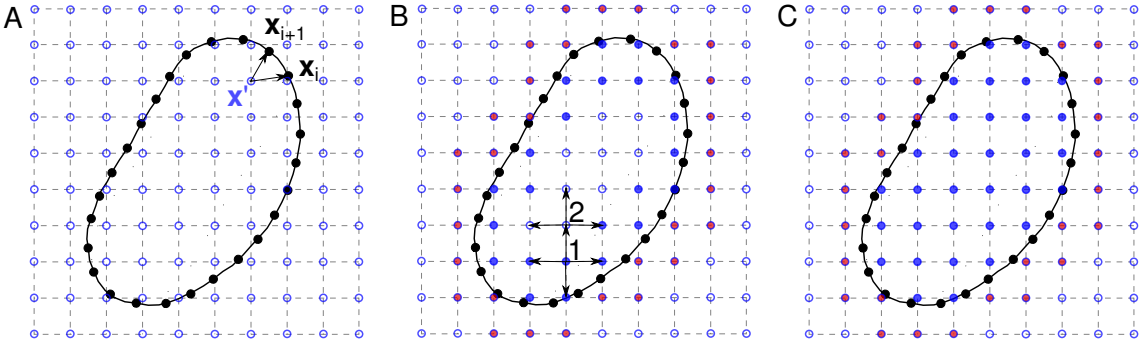

Figure 2.9: The proceeding to find the internal fluid nodes. A: The fluid node $\mathbf{X}'$ is the neighbor of the membrane. The membrane nodes $\mathbf{X}_i$ and $\mathbf{X}_{i+1}$ are the neighbors of the fluid node $\mathbf{X}'$. The cross product of $\mathbf{X}_i - \mathbf{X}'$ and $\mathbf{X}_{i+1} - \mathbf{X}'$ is calculated to decide whether the node $\mathbf{X}'$ is internal or not. B: All the neighbors of the membrane have been identified. The internal nodes are marked by blue solid points. The external nodes are marked by red solid points. The internal fluid node 1 is chosen as a seed. It searches the neighboring nodes along both of x axis and y axis. Once an unidentified node (node 2) is found, it is chosen as a new seed. C: The new seed continues to search until all the unidentified nodes inside the membrane are found.

5. Do streaming in the LBM, get the distribution $f_i(\mathbf{x}_f, t+1)$ at time step $t+1$.
6. Implement boundary conditions.
7. Calculate the macro variables, get the fluid velocities $\mathbf{u}_f(t+1)$ at time step $t+1$.
8. Interpolate the RBC velocities $\mathbf{u}_m(t+1)$ from fluid velocities and update the RBC positions $\mathbf{x}_m(t+1)$.
9. Go to step 2 for next time step

We have also performed 3D IB-LBM simulations. The code is provided by J. Harting Group. The presentation of the methods can be found in T. Krüger's thesis [Krüger, 2012].

2.6 Identification of the internal fluid nodes

A dimensionless parameter $\lambda = \eta_{int}/\eta_{ext}$, called viscosity contrast, is defined as the ratio between viscosity of internal fluid and external fluid. For the physiological condition, the hemoglobin solution is more viscous than the plasma with a viscosity contrast of about 5. In our simulations, the value of λ is changed by varying the relaxation time τ in LBM for internal fluid, since we have seen that the viscosity is fixed by that time. The technical task is not easy in practice, since this requires

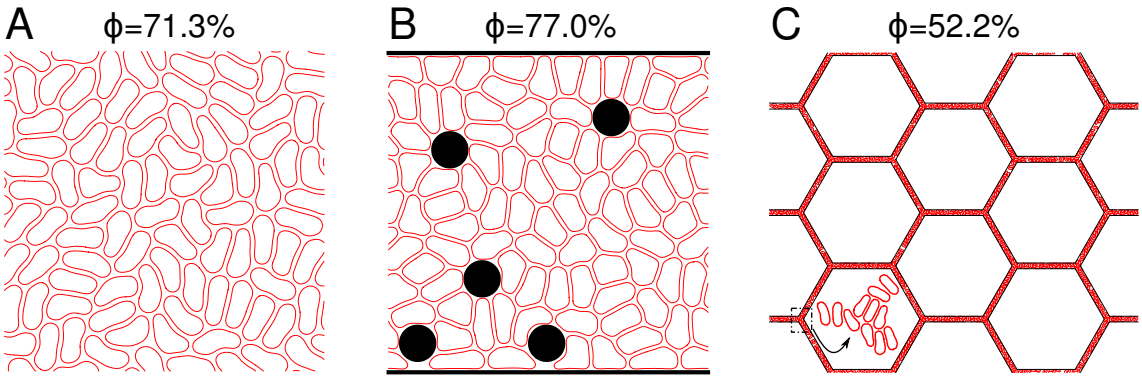

Figure 2.10: Some cases of the initialization of RBCs in high concentration situation. ϕ is RBC concentration (area fraction). A: In the periodic domain. B: In a wall bounded channel with some obstacles. The black region means obstacles. C: In a network.

identification of the internal fluid nodes at every time step, which is computationally expensive with a traditional algorithm when a large number of RBCs are simulated. We developed a so-called seed algorithm which has high efficiency. The procedure is described in Figure 2.9. The first step is to identify all the neighbors of the membrane. Take, for example, a fluid node $\mathbf{X}'$, and the internal fluid is fixed by the direction of the cross product of the vector from $\mathbf{X}'$ pointing to the neighboring membrane node $\mathbf{X}_i$ and the vector from $\mathbf{X}'$ to $\mathbf{X}_{i+1}$ which is the anti-clockwise neighbor of $\mathbf{X}_i$. The internal fluid has the paper out cross product while the external fluid has the paper in cross product. After all the neighbors are identified, the identified nodes form a closed boundary, where the enclosed nodes are internal fluid nodes (the hollow points inside of the membrane in Figure 2.9). To find these enclosed nodes, one identified internal fluid node is chosen as the seed. The seed grows to its neighbors and marks the unidentified node as the next seed until all the enclosed nodes are found. With this algorithm, the internal fluid nodes can be quickly found, then the τ on these nodes are reset for the viscosity contrast. Because a large τ causes low accuracy and a small τ causes instability, the practical viscosity contrast is usually less than 10 in our simulations. Higher viscosity contrasts can be carried out by our simulations, but the result can be trusted at best only qualitatively.

2.7 Initialization of RBC positions

The initial position of RBCs can be created manually or randomly with a natural biconcave shape for diluted situation. It is also possible to get a large concentration with a regular arrangement of the initial positions. However it is quite time consum-

ing to get the random initial position for high concentration, because the biconcave shapes with random orientations make it difficult to fill the space in an efficient way. It has seemed necessary to develop a way to position the RBCs randomly for high concentration flow. We firstly position a large number of RBCs randomly by representing each cell initially as a small circle (the small circular shape helps getting a dense enough suspension). Once a circle is positioned, the circle occupancy in the computational domain is marked. When a new circle is created, we check if it overlaps with an old circle or with the solid boundary. If not, it will be positioned, otherwise, a new circle will be re-created until meeting the non-overlapping requirement. This process goes on until the desired number of cells is reached. Since we are interested in having biconcave shapes, not circular ones, the next step is to transform the circles into a biconcave shape. This task is achieved thanks to two energetic terms of the model implemented into the IB-LBM: in the Equations 2.26 and 2.27 the parameters are chosen so that the perimeter and area should correspond to those of a RBC (approximately). Therefore the circle will naturally evolve towards those value. Finally the Equation 2.28 is responsible for the selection of the biconcave shape. Since we are interested at this stage in getting the initial configuration, the real hydrodynamical dissipation does not matter. Therefore, in order to accelerate the convergence towards biconcave shape we use an artificial dissipation by resetting at every 1000 time steps the distribution function in a way to keep the fluid quiescent. The RBCs adapt their shape during the circle extension process, making the filling of space quite adequate and quite efficient. This procedure only costs less than one hour to position hundreds of RBCs in a complex network for a concentration of 52.2% as shown in Figure 2.10.

2.8 Benchmarking tests

The first test is to compare the equilibrium shape of a vesicle obtained by IB-LBM and simple molecular dynamics model. Figure 2.11 shows the equilibrium shape for different reduced area. The shapes produced by these two methods agree with each other and the shapes shown in Figure 2.11 are indistinguishable.

The second test is to reproduce the tank-treading and tumbling motion of a vesicle. The dynamics of single vesicle show the typical motions, tank-treading (TT) and tumbling (TB), which are influenced by the deformability of the membrane. Here we explore viscosity contrast while keeping the capillary number to 1 and reduced area to 0.7. The computational domain is $48R$ in flow direction and $12R$ in shear gradient direction. With a so large domain, the effect of periodic boundary and bounding walls are so small that it becomes legitimate to compare the results with previous ones obtained in unbounded linear shear flow. The viscosity contrast λ plays the role in transition from TT to TB. Below a critical λ_c, the vesicle membrane

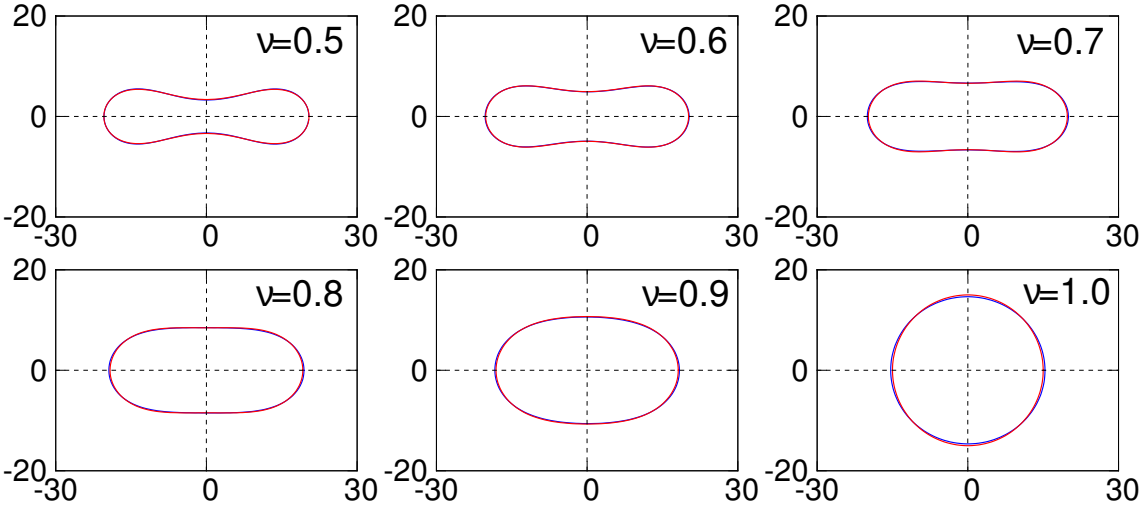

Figure 2.11: Vesicle shape for different reduced areas. The red line is obtained by IB-LBM. The blue line is obtained by simple molecular dynamics model. ν is reduced area. The coordinate is using LBM unit.

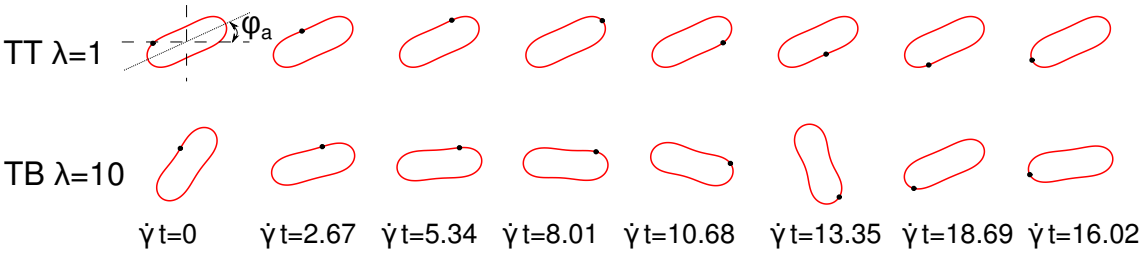

Figure 2.12: The tank-treading motion and tumbling motion. φ_a is the inclination angle. $\dot{\gamma}$ is shear rate. The black point is a mark on the membrane.

moves as the tread of a tank with a fixed shape and orientation. This is shown in Figure 2.12 for $\lambda = 1$. By increasing λ, the inclination angle φ_a decreases as shown by for $\lambda = 1$ and $\lambda = 3$ in Figure 2.13. When λ is close to a critical value, λ_c, φ_a tends to 0 and undergoes cyclic motion (tumbling) for $\lambda > \lambda_c$ (see Figure 2.12). The transition value λ_c is obtained approximately for 5 in our tests. When λ increases, the tumbling frequency increases as well, as presented in Figure 2.13 for $\lambda = 5$, $\lambda = 7$ and $\lambda = 9$.

Then next test has consisted in studying rheology. The normalized viscosity is defined as $[\eta] = (\eta - \eta_{ext})/(\eta_{ext}\phi)$. η is the effective viscosity of the vesicle suspension and the η_{ext} is the viscosity of the suspending solution. The rheology of the suspension shows a macro/micro link, in that the behavior of $[\eta]$ is intimately linked with the microscopic dynamics, namely tank-treading and tumbling. Figure

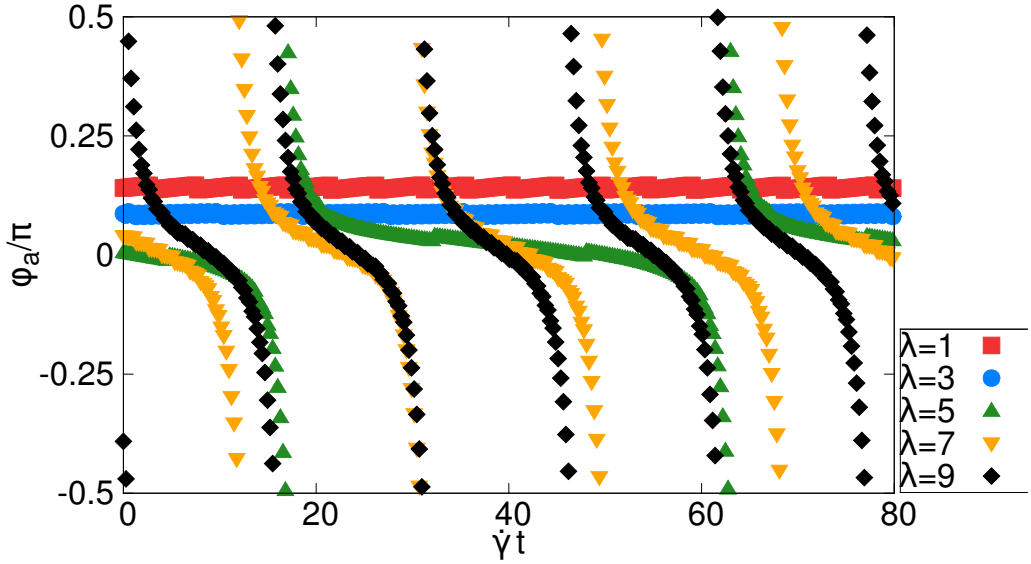

Figure 2.13: Time evolution of the inclination angle for different viscosity contrast.

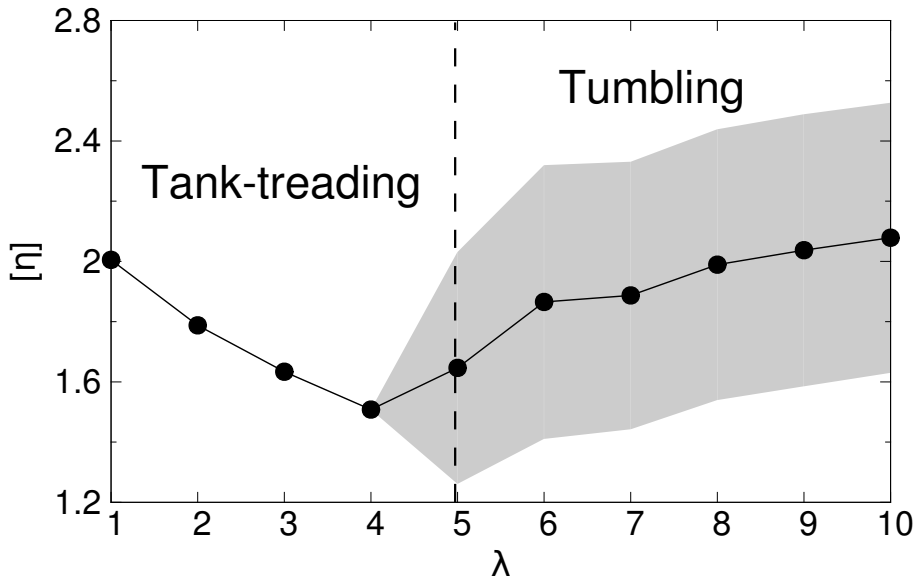

Figure 2.14: The normalized viscosity as a function of viscosity contrast.

2.4 shows the normalized viscosity which exhibits a decrease with increasing λ in tank-treading regime. This decrease is linked with a decrease in inclination angle which lowers resistance against overall flow. When λ tends to λ_c, the inclination angle gets close to 0, so that the normalized viscosity is minimal at the TT-TB

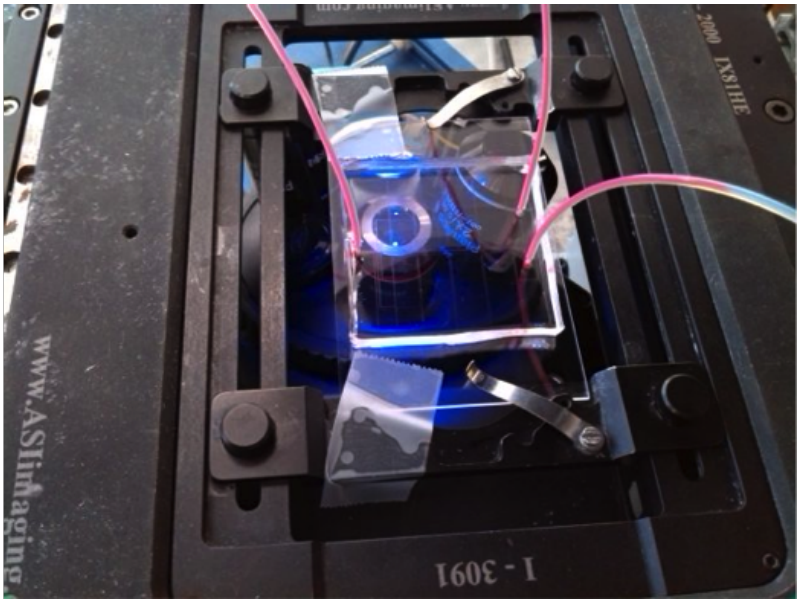

Figure 2.15: A schematic of experimental set up.

transition point. In the tumbling regime, the normalized viscosity increases with increasing λ. The rotation of the inclination results in more resistance against flow. As shown in Figure 2.13, when λ is close to the λ_c, the vesicle spends most of time in the state aligned with the flow and less time in rotation. By increasing λ, the time spent on the aligned state is reduced, inducing thus an increase of the normalized viscosity.

All above results are in a good agreement with previous studies [Ghigliotti et al., 2010; Kaoui et al., 2009b], thus supporting validation for our numerical method.

2.9 Microfluidics set-up

We have performed experiments for the validation of the simulations in Chapter 5 regarding the hematocrit partition at a bifurcation. Microfluidic channels are produced by standard soft lithography techniques, with molded PDMS bonded to glass. As shown in Figure 2.15, the RBC suspensions are perfused by a syringe pump (KDS Legato 180) and imaging are performed by a video camera (Imaging Source DMK 31AF03) mounted on an inverted microscope with motorized stage (Olympus IX71) and a blue filter (434 ± 25 nm) corresponding to an absorption peak of hemoglobin.

Blood samples are provided by the Etablissement Français du Sang (EFS Rhône-Alpes) from healthy donors. RBCs are isolated by centrifugation after being washed

twice in phosphate buffer saline (PBS) supplemented by 0.1 % bovine serum albumin (BSA). To prevent sedimentation of RBCs in channels, the RBCs are re-suspended in density-matching PBS and BSA solutions in a mixture of water and iodixanol (Optiprep from Axis-Shield).

More details of the experimental set-up will be presented in Section 5.2 in Chapter 5.

Chapter 3

Interaction and rheology of blood suspension in confined shear flow

In this chapter, we perform 2D simulations of a blood suspension in confined shear flow to study the hydrodynamic interaction between cells and the rheology of suspension. The introduction of this work is given in Section 3.1. The parameters of computation are given in Section 3.2. The interaction between two tank-reading vesicles is discussed in Section 3.3. Then the interaction between two tumbling vesicles is discussed in Section 3.4. In Section 3.5, we talk about the order and disorder of vesicle suspension. At last, the link between the order and the rheology of suspension is presented in Section 3.6.

3.1 Introduction

Red blood cells (RBCs) achieve their main functions in the microcirculation, such as oxygen supply to tissues and organs and removal of metabolism wastes. Through their individual motions and mutual interactions, RBCs play an important role in the regulation of the blood flow properties, and are consequently expected to have an impact on the physiological function of organisms. Therefore, understanding blood flow in a confined geometry is a basic key element in order to extract some information that are likely to play a role in a more complex configuration. Besides the obvious interest in studying RBCs in the microcirculation, there are also fundamental questions related to the rheology of complex fluids where the effect of confinement can drastically alter the flow properties, as we will see in this work.

Blood is traditionally viewed as a collection of deformable particles suspended in a fluid (plasma). The dynamics of a single deformable particle (vesicle, capsule, etc) is relatively well understood thanks to a series of theoretical [Keller and Skalak, 1982; Kraus et al., 1996; Misbah, 2006; Noguchi and Gompper, 2004, 2007; Skotheim and

Secomb, 2007], experimental [Abkarian et al., 2007; Fischer et al., 1978; Kantsler and Steinberg, 2006; Mader et al., 2006] and numerical [Bagchi and Kalluri, 2009; Biben et al., 2011; Pozrikidis, 2003] studies (see also reviews [Barthès-Biesel, 2016; Fedosov et al., 2014; Seifert, 1997; Vlahovska et al., 2009]). For example, in simple shear flow, the typical motions of RBC, tank-treading, tumbling and vacillating breathing (or swinging) have been extensively studied. Understanding of these dynamics has guided understanding of the rheology of dilute suspension of vesicles [Danker and Misbah, 2007; Ghigliotti et al., 2010] and capsules [Bagchi and Kalluri, 2010, 2011].

However, in physiological conditions, blood is highly concentrated with an average hematocrit of 45% in human body (in microcirculation, the hematocrit is lower, in the range of $10 - 20\%$ [Fung, 2013]). Thus hydrodynamic interaction among RBCs, as well as the presence of bounding walls, should be taken into account for a better description of situations which are relevant to blood flow [Breyiannis and Pozrikidis, 2000; Zhao and Shaqfeh, 2013]. Semi-dilute and concentrated suspensions exhibit a diffusion-like process leading to a mixing of cells [Farutin and Misbah, 2013; Grandchamp et al., 2013; Tan et al., 2012], as well as depletion layers (cell-free layer) in a pressure-driven flow. As a first fundamental question of the collective dynamics, the interaction between two bodies in simple flow has been carried out by several groups [Doddi and Bagchi, 2008; Gires et al., 2014; Lac et al., 2007; Le and Chiam, 2011]. Fox example, a lateral shift (i.e; orthogonal to the flow direction) in trajectory of the particles is observed when they meet in the shear flow, which results in the so-called shear-induced diffusion.

Another characteristic of blood flow in the microcirculation is that the diameter of blood vessels has a comparable size to the RBC size. This makes RBCs always flow in a confined environment, which has been shown to impact blood flow properties. A prominent example is the Fåhræus-Lindqvist effect [Barbee and Cokelet, 1971; Pries and Secomb, 2003; Pries et al., 1994] in small vessels, where the apparent viscosity of blood decreases with decreasing diameter of the tubes. This effect is attributed to the existence of a cell-free layer near the tube wall. The cell-free layer is attributed to a lift force due to the bounding walls that tend to push the cells towards the center of the tube [Abkarian et al., 2002; Cantat and Misbah, 1999a; Coupier et al., 2008a; Farutin and Misbah, 2013; Seifert, 1999]. Recently, several studies have revealed that the confinement can have a significant influence on the dynamics of a single deformable particle [Kaoui et al., 2011, 2012] as well as on the rheology of the suspension [Kaoui et al., 2014; Lamura and Gompper, 2013; Thiébaud et al., 2014] in simple shear flow.

Recently, we have provided a brief report on the rheology of a confined suspension in a linear shear flow [Thiébaud et al., 2014]. In this work, besides an extensive discussion, we investigate several novel aspects, which we summarize as follows: (i) the flow field created by a vesicle is analyzed under close scrutiny and this provides a clear image of the existence of an equilibrium state between two confined and

tank-treading vesicles. This equilibrium state will be shown to play a key role in the spatial organization. (ii) We analyze the role of a viscosity contrast and show that even vesicles with very viscous internal fluids can organize into a regular pattern, due to a tank-treading regime triggered by confinement, but disorder prevails if confinement is weak enough for leading a tumbling motion of vesicles. (iii) We provide a link between spatial organization and the signature of rheology, in that the normalized viscosity either shows ample oscillation (associated with order), or a monotonous behaviors (associated with disorder). We find that the effective viscosity exhibits plateaus with concentration in some regimes accompanied with order.

3.2 Methods and parameters

Here we recall the definition of some important parameters and give the values of these parameters used in this work. A dimensionless parameter $\lambda = \eta_{int}/\eta_{ext}$, called viscosity contrast, is defined as the ratio between viscosity of the fluid inside the vesicle and that of the suspending fluid. Two values of λ (1 and 10) are used in this work for tank-treading and tumbling motion (when confinement is weak, otherwise tank-treading is triggered by confinement). The value of λ can be varied in the LMB by adopting two different relaxation time scales inside and outside the vesicles in the BGK expression. We define the reduce area as $\nu = 4\pi s/C^2$, where C is the vesicle perimeter. For a circle we have $\nu = 1$, whereas $\nu < 1$ for any other shape. In this study we have mainly explored the case $\nu = 0.7$ that provides a biconcave equilibrium shape, albeit other values have also been tested as reported below. The capillary number $C_a = \mu_{ext}R^3\dot{\gamma}/4k_b l_0$ is kept at 1. The computation model is a suspension of vesicles sheared between two counter-moving rigid plane walls, which are located at $Y = -W/2$ and $Y = W/2$ (W is the gap between the two bounding walls). Periodic boundary conditions are applied at the two lateral boundaries which are orthogonal to the flow direction. The computational domain along the flow direction (X) is fixed to a length equal to $63.7R$, while the gap is varied in some interval of values, to be specified below.

3.3 Interaction between two tank-treading vesicles

The interaction between two tank-treading vesicles in unbounded shear flow has been investigated in many previous works [Doddi and Bagchi, 2008; Gires et al., 2014; Lac et al., 2007; Le and Chiam, 2011]. When two vesicles move towards each other along the flow directions and pass each other, their mutual hydrodynamic interaction induces a lateral migration along the direction of shear gradient, that

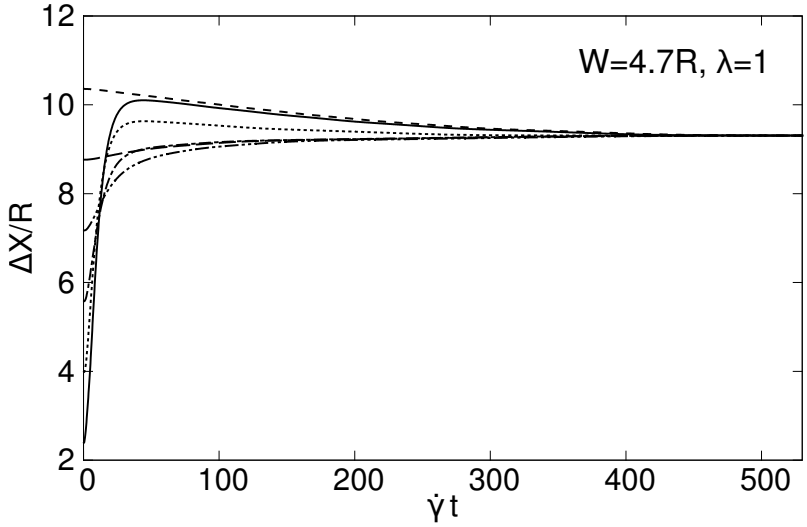

Figure 3.1: The distance between two tank-treading vesicles as a function of time in several cases of different initial positions. Finally, the two vesicles can go to an equillibium state with a constant interdistance. The W is the distance between two shearing wall. The λ is viscosity contrast.

pushes them away from each other. This interaction plays an important role in the shear-induced diffusion of deformable particle suspensions.

The situation is quite different in the presence of walls. When the flow is confined between two walls, a lateral migration of the vesicle is caused by the lift from one of the two walls (which tends to push the vesicle away from that wall). Due to symmetry, both of the walls have opposite effects and one expects the vesicle to stop at the centerline (of course, if the shape of the vesicle undergoes a parity-symmetry-breaking, as discovered in [Farutin and Misbah, 2012], this expectation may be violated since the shape breaks the up-down symmetry). For all situations explored so far we find that the vesicle always settles in the flow centerline. Additionally, we find that two vesicles always keep a constant relative distance when they stop at the center. As shown in Figure 3.1, with several different initial positions, the pair of vesicles always reach the same terminal interdistance. This means that we have an interplay between a repulsion due to hydrodynamic diffusion but an attraction due to the wall lift force. If a balance occurs between these two mechanisms, then an equilibrium state may take place leading to a stable pair of vesicles in the channel. This is what we have observed for all simulations with tank-treading vesicles.

In order to dig into the consequences expected from the presence of confinement, the velocity field created by a single confined vesicle is analyzed first. We focus only on the induced field (which is nothing but the total flow from which the imposed

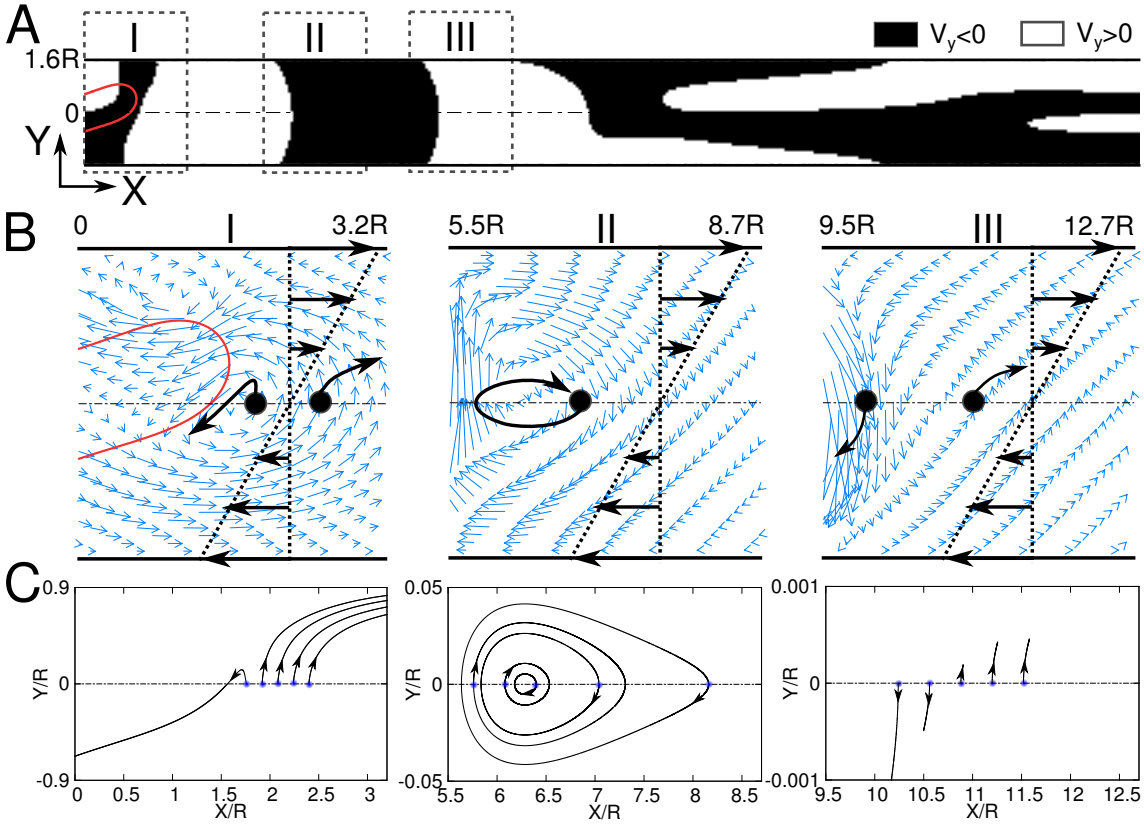

Figure 3.2: (A) The flow field around a single tank-treading vesicle in confined linear shear flow (only right half part of the domain is presented because of the symmetry). The regions for upward flow and downward flow are highlighted by black and white respectively. (B) The induced flow (total flow subtracted by the imposed linear shear flow) in region I, II and III, and the schematics of the motion of a tracer are plotted. Compared to region I, the vectors are amplified by 400 times in region II and by 60000 times in region III. (C) The trajectories of the tracers with the starting at the center in region I, II and III.

linear shear flow is subtracted). The result is presented in Figure 3.2 in the presence of a single vesicle performing a tank-treading motion. In Figure 3.2 B, we visualize the flow field in different adjacent regions on the right side of the vesicle under consideration. We first notice the presence of vortices in the form of a quadrupole-like pattern (also see the structure of the flow field in Figure 3.3) surrounding the vesicle. This recirculation is a direct consequence of confinement. In the region denoted as I in Figure 3.2 B, and on the right side far from the vesicle, we see that the flow field points upwards. Fluid particles that are at the extreme right of region

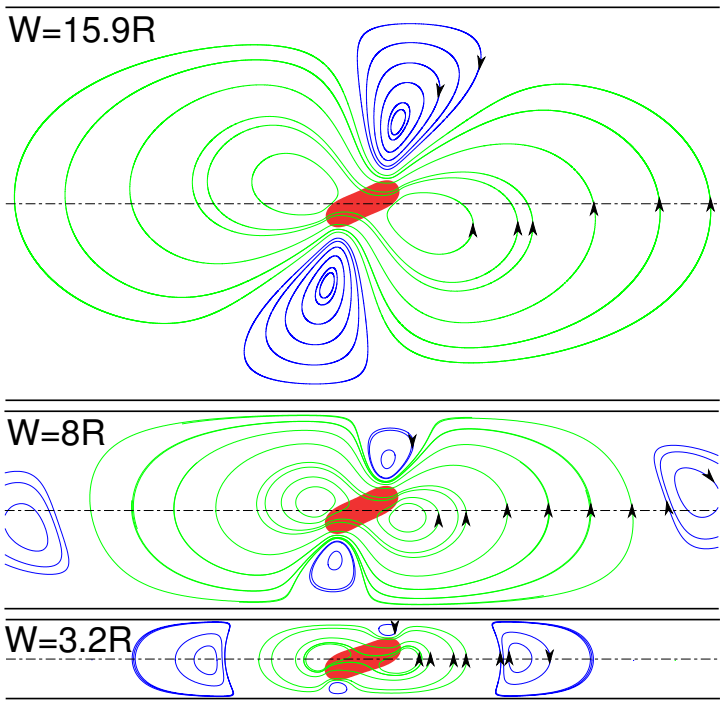

Figure 3.3: The structure of the induced flow in different confinements. A clockwise vortex (blue streamlines) appears due to the confinement. When W decreases, the clockwise vortex gets closer to the vesicle.

I (most of them below centerline) will ascend with an inclined trajectory to the right. They will hit the upper wall and bounce backwards, as shown in region II. We see there, on the right part of region II, that close to centerline, the flow field is downward, and that we have a clockwise vortex, while in region I the vortex is anti-clockwise. These flow patterns in regions I and II constitute the key element in order to understand the possibility for the formation of an equilibrium state made of two vesicles. Figure 3.2 A represents regions where the vertical fluid velocity is upward (white regions) and regions where it is downward (dark regions).

To highlight the effect of the above flow pattern, we consider a tracer (the points in Figure 3.2 B and C) which is initially put on the center line and near the interface between a dark and a white area. The schematics of the possible trajectories of the tracer are given in Figure 3.2 B and the real trajectories of the tracers in region I, II and III are plotted in Figure 3.2 C. Only in region II, where a clockwise vortex takes place, does the trapping of the tracer occurs. As the example shown in region II in Figure 3.2 B, firstly the tracer goes down and left following the tank-treading

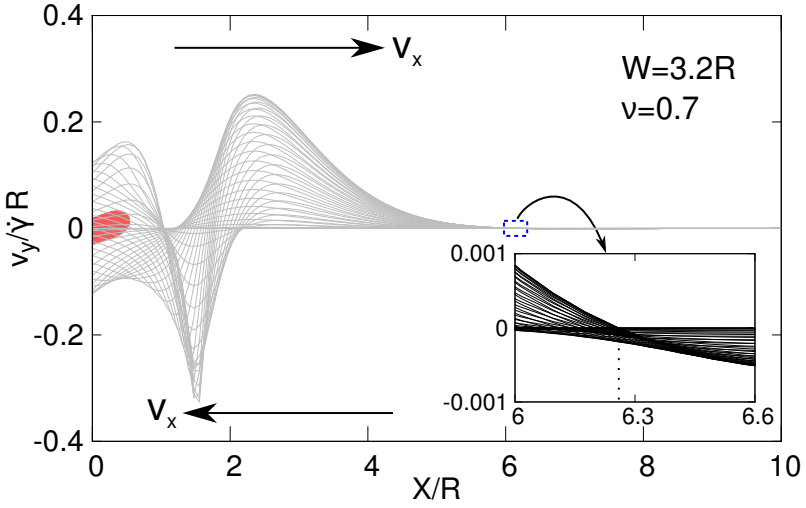

Figure 3.4: Velocity in Y direction as a function of the distance to the mass center of the vesicle. The inset is an amplification of a local region, which is approximately corresponding to the region II in Figure 3.2. Each line shows the V_y distribution at one Y coordinate. These lines give an approximate place where the V_y direction change sign at $X = 6.3R$ in the case of $W = 3.2R$. The reduced area of the vesicle is $\nu = 0.7$.

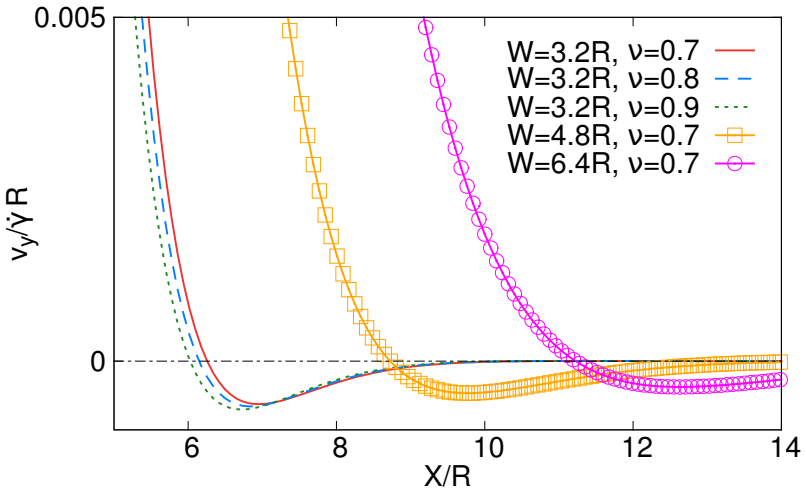

Figure 3.5: For different confinements and reduced areas, the V_y along the flow direction at center is plotted in a local region where the tank-treading induced flow shows a clockwise vortex.

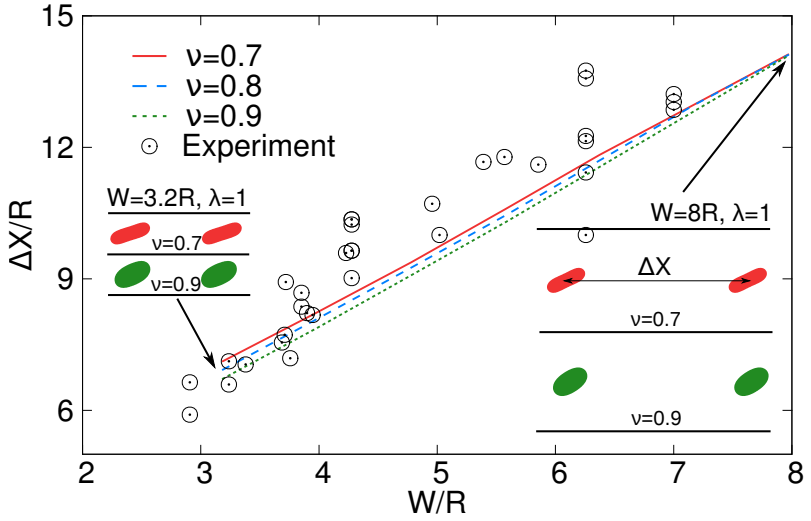

Figure 3.6: The equilibrium distance between two vesicles increases linearly with the W. The insets are the final configurations of the vesicles in the cases of $W = 3.2R$ and $W = 8R$.

induced flow and the shear flow below the center line (left). When it crosses the interface of the black and white region, the tank-treading induced flow changes the direction, the tracer goes up and then crosses the center line, where it follows the shear flow above the center line (right) and turn back in the X direction. It crosses the interface of the black and white region again, where the tank-treading induced flow becomes downward, which makes the trace finally flow back to the starting position. While in the cases in region I and region III, in an anti-clockwise vortex, the tracer can't be trapped, the flow field shows that the tracer flows away following the shear flow (see the trajectories in Figure 3.2 C). If the tracer is substituted by a vesicle, one is tempted to expect qualitatively a similar situation, though a vesicle can not be viewed as a tracer, since it perturbs the flow field around. However, we may consider the reasoning above as a crude vision of the possible existence of a bound state between the two vesicles. When the vesicle is trapped by the other one, different from the tracer doing circulation, the vesicle is always pushed to the center by the wall induced lift, which decays the circulation and finally makes it stop at a certain place on the center line. It must be noted that more equilibrium positions can be found along the center line with farther positions. However, the induced velocity is so small at these positions that the interaction can be ignored (actually the decay of velocity field in two dimensions is exponential with X).

In order to lend further support to the above analysis, we have performed the following analysis. We first take a single vesicle and compute at what distance the

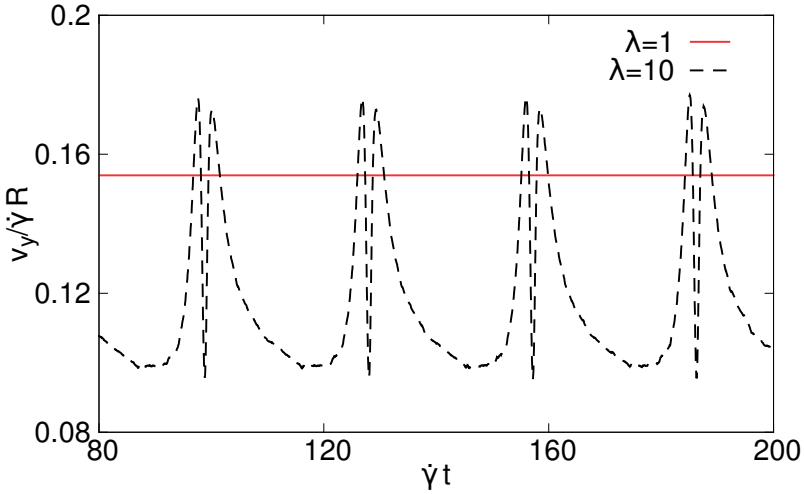

Figure 3.7: Velocity in Y direction at a given position in the flow field created by a single vesicle of tank-treading and tumbling. The velocity is measured at the position $4R$ away from the vesicle center and located on the center line of the domain.

first occurrence of a dark region (flow inversion), which is disconnected from the dark part containing the vesicle, takes place. We then introduce two vesicles in the domain and ask what is the equilibrium distance of the bound state. For a single vesicle, we plot the V_y distribution along the X axis in the whole computational domain, as shown in Figure 3.4. We find that the transition position of flow inversion in Y direction (region II) in Figure 3.4 is located around $X = 6.3R$. Interestingly enough, the equilibrium interdistance of two vesicles (see Figure 3.6) is quite close to that obtained by the analysis of the flow field with a single vesicle. This supports both qualitatively and quantitatively the explanation of the generation of the equilibrium state of two tank-treading vesicles. Since the transition of V_y direction is caused by the wall bounce-back, it is expected that when W increases, the position at which an ascending fluid particles meet the wall becomes farther, thus the transition position of V_y inversion also gets farther, which can be found in Figure 3.3. This means the larger W the higher interdistance between two vesicles in an equilibrium state. Figure 3.5 presents evolution of V_y along the center line for different confinements and reduced areas. This figure supports the idea that the transition position of V_y inversion becomes farther with increasing W. When W takes values $3.2R$, $4.8R$ and $6.4R$, V_y changes direction approximately at $X = 6.3R$, $8,7R$ and $11.3R$ respectively, pointing to a quasi-linear dependence. However, the reduced area has a very weak effect on the transition of V_y direction. The location of V_y inversion gets slightly closer when ν increases. This means that a less deflated vesicle (higher ν) disturbs the flow in a stronger manner promoting thus attraction.

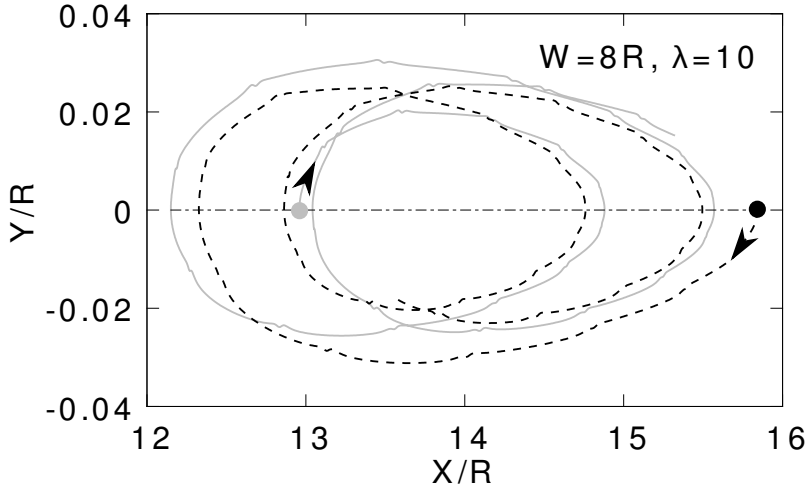

Figure 3.8: The chaotic trajectories of two tracers in the flow of a tumbling vesicle.

A systematic study is then undertaken in order to analyze the behavior of a pair of vesicles in a confined shear flow. We have explored several confinements and several values of the reduced area. All simulations have confirmed the tendency discussed above, in that the presence of a clockwise vortex is the source of the formation of a bound state between the pair of vesicles. The results are summarized in Figure 3.6. We find a linear relationship between the equilibrium distance of the two vesicles and the confinements. Let us compare the equilibrium distance of the pair with the distance at which the Y component of the velocity field created by a single vesicle (the distance is counted from the center of mass of the vesicle) crosses zero from positive to negative values. The corresponding results are presented in Figure 3.5. Interestingly enough, we find the two distances agree reasonably well for all confinements and reduced area explored so far. These results highlight the fact that the simple reasoning based on the analysis of the velocity field due to a single vesicle already captures the essential features. This observation is interesting as much as it offers a simplified basis for future analytical calculations where only a single vesicle can be taken into account in order to draw general conclusions on the behavior of pairs of vesicles (or even a collection of vesicles) in a channel.

3.4 Interaction between two tumbling vesicles

Besides tank-treading vesicles are known to exhibit tumbling provided by the large enough viscosity contrast λ. A tumbling vesicle creates a temporally oscillating flow pattern. Figure 3.7 shows V_y at a given position ($X = 4R$) from the center of mass

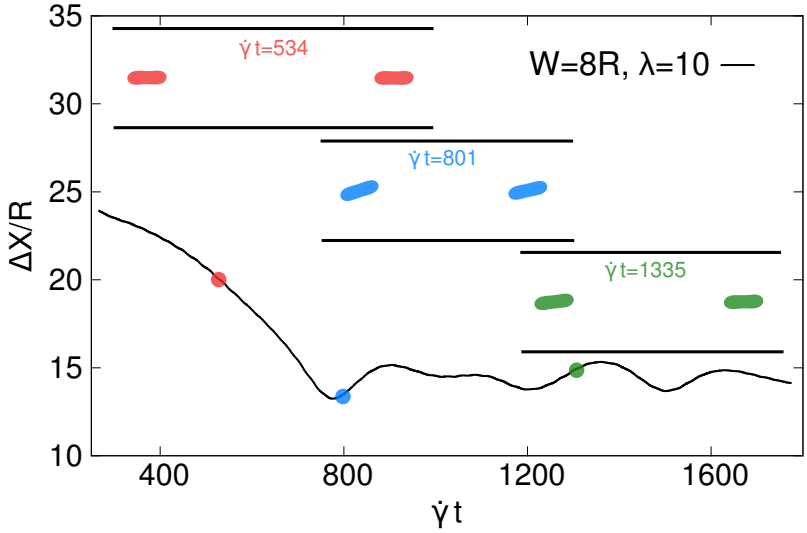

Figure 3.9: The relative distance between two tumbling vesicles as a function of time. The insets are the configurations of the vesicles at the time of $\dot{\gamma}t = 534$, $\dot{\gamma}t = 801$ and $\dot{\gamma}t = 1335$. $\dot{\gamma}$ is the shear rate.

of a vesicle and evaluated at the flow centerline for a given confinement ($W = 8R$). This result (obtained for $\lambda = 10$ where the vesicle tumbles) is compared to that of a tank-treading vesicle ($\lambda = 1$). We see a clear difference between the two fields: it is constant in time for a tank-treading vesicle, while it is oscillating in time for a tumbling vesicle. A tracer located at some distance from the tumbling vesicles would oscillate both vertically and horizontally in time, and exhibit a chaotic trajectory as shown in Figure 3.8. In principle, one expects the second vesicle position to oscillate irregularly in time as well.

The relative distance and relative orientation angle (taken as the difference between the two orientation angles) between two vesicles for the tumbling case are presented in Figure 3.9 and Figure 3.10. The difference in angles shows no correlation and one sees an apparently erratic motion. In Figure 3.9 we also show the distance along X between the two mass centers of the two vesicles. While the pair of vesicles remain at some interdistance on average, the instantaneous interdistance varies with time in an irregular fashion. We can not talk of an equilibrium state in the same sense as we did for tank-treading vesicles. We thus do not expect a suspension of tumbling vesicles to exhibit any kind of order. The configurations of the pair of vesicles at different time are given in the insets of Figure 3.9.

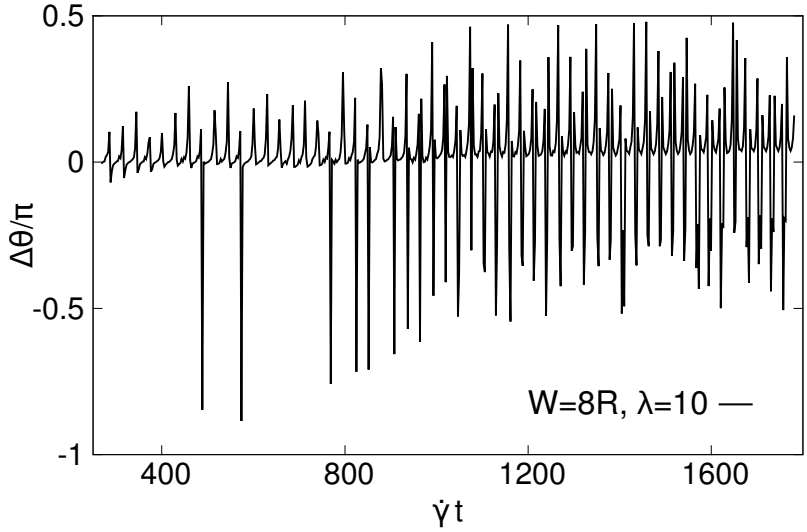

Figure 3.10: The relative orientation angle between two tumbling vesicles as a function of time.

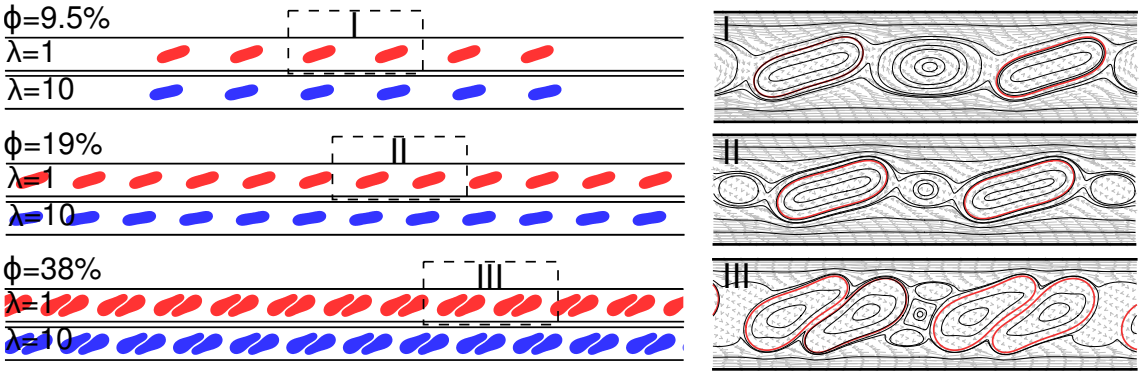

Figure 3.11: Left column: Configurations of a vesicle suspension in the confinement of $W = 3.1R$. Vesicles form one file in low concentration. Two vesicles couple a doublet in high concentration. Right column: The structure of the flow field in region I, II and III. ϕ is the vesicle concentration (area fraction in 2D). The recirculation between two vesicles decreases when concentration increases as shown in region I and II.

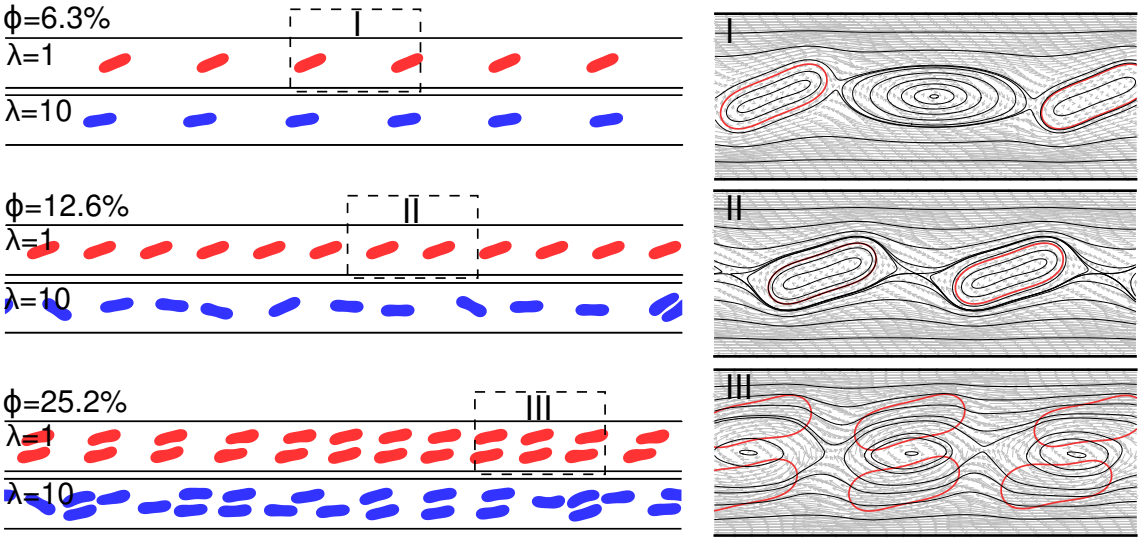

Figure 3.12: Left column: Configurations of a vesicle suspension in the confinement of $W = 4.7R$. For low viscosity contrast $\lambda = 1$, vesicles form one file in low concentration and two sliding files in high concentration. For high viscosity contrast $\lambda = 10$, vesicles form one file in very low concentration, then they are disordered with increasing concentration. Right column: The structure of the flow field in region I, II and III.

3.5 Spatiotemporal organization of a vesicle suspension

Based on the understanding of the interaction between two vesicles, it is hoped to extract some general conclusions on the behavior of a suspension. We would like to see how confinement influences the configuration of a vesicle suspension. We have systematically analyzed this question by exploring concentrations from 0 to 40% for three different confinements: $W = 3.1R$, $4.7R$ and $6.3R$. Different configurations of the suspension are displayed in Figure 3.11, Figure 3.12 and Figure 3.13 for low viscosity contrast ($\lambda = 1$) and high viscosity contrast ($\lambda = 10$).

A general observation is that for a strong enough confinement, the viscosity contrast plays no special role. Indeed, even if λ is large, where a weakly confined vesicle would exhibit tumbling, the presence of a strong enough confinement prevents tumbling. In other words, both for small as well as large λ vesicles undergo tank-treading as the case of $W = 3.1R$ shown in Figure 3.11. Starting from an initial configuration of the suspension chosen randomly within the channel, vesicles first experience a lift force due to the walls. Because of symmetry, the vesicles settle at the centerline

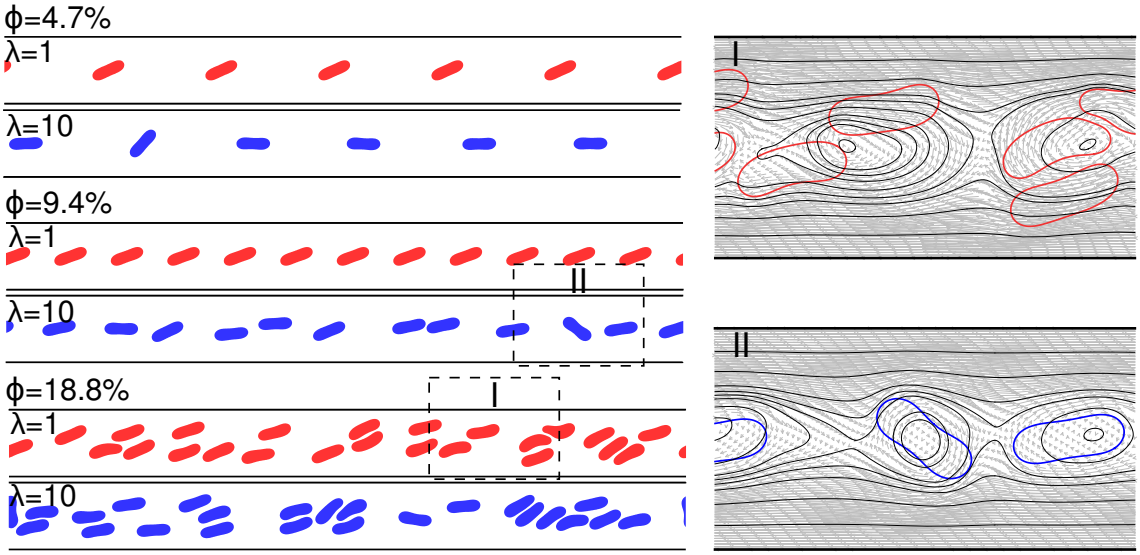

Figure 3.13: Left column: Configurations of a vesicle suspension in the confinement of $W = 6.3R$. For $\lambda = 1$, vesicles form one file in low concentration, but they are disordered in high concentration. For $\lambda = 10$, vesicles are disordered under this confinement. Right column: The structure of the flow field in region I and II

exhibiting an ordered alignment along a single file in the case of a dilute enough suspension. The configuration tends to a stable state with an equilibrium distance between two neighbors. At a larger concentration, in the semi-dilute regime, the intensity of vortex between vesicles becomes smaller (see Figure 3.11 right column) when an additional vesicle would settle in there. But in high concentration, the insertion of an additional vesicle makes its position become unstable. It is absorbed by the nearby vesicle so that they tend to form a doublet. Now each doublet can be viewed as a single entity, and the doublets form a regular arrangement (see the configuration of $\phi = 38\%$ in Figure 3.11). In other words, we have a symmetry breaking bifurcation from an array of vesicles towards an array of doublets. This type of ordering may be referred to as a superstructure with spatial period doubling. For this strong confinement we obtain the same overall behavior for both $\lambda = 1$ and $\lambda = 10$.

In the case of a weaker confinement ($W = 4.7R$, Figure 3.12), and for $\lambda = 1$, we have another type of bifurcation upon increasing concentration ϕ. For a small ϕ we form a single ordered file, while at larger ϕ the single file splits into two lines which are approximately symmetric with respect to the flow centerline. The two files slide with respect to each other in a quite regular way. The situation is more complex for $\lambda = 10$. Indeed at small ϕ we have a single ordered file. Upon increasing ϕ we first

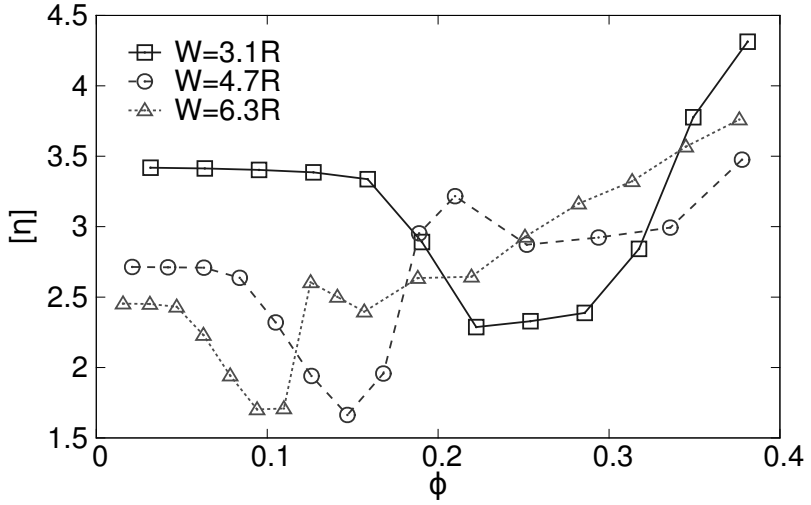

Figure 3.14: Normalized viscosity of a vesicle suspension for $\lambda = 1$ in different confinements.

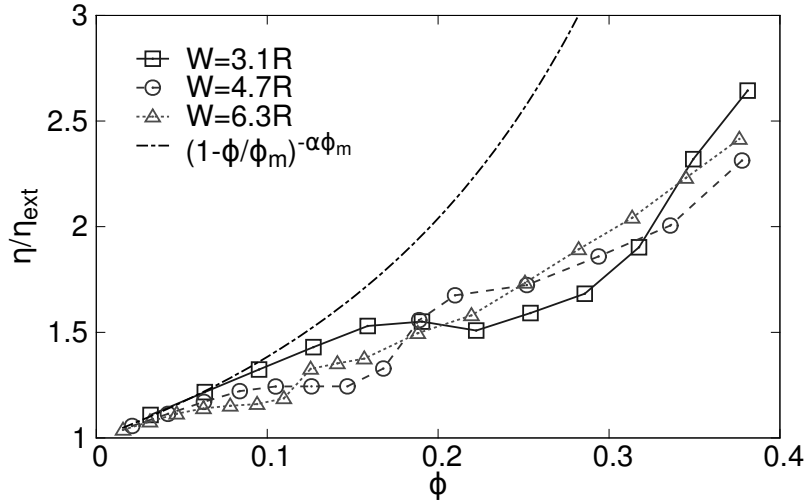

Figure 3.15: Effect viscosity of a suspension of vesicles with $\lambda = 1$ in different confinements. $\alpha = 3$ and $\phi_m = 0.67$ for the normal human RBC at low shear rate [Pal, 2003].

see a destabilization of order due to the fact that interaction among vesicles triggers tumbling (while for small ϕ each vesicles undergoes tank-treading). While order is partially destroyed the single file maintains its identity. Upon increasing ϕ the file splits into two files containing several defects.

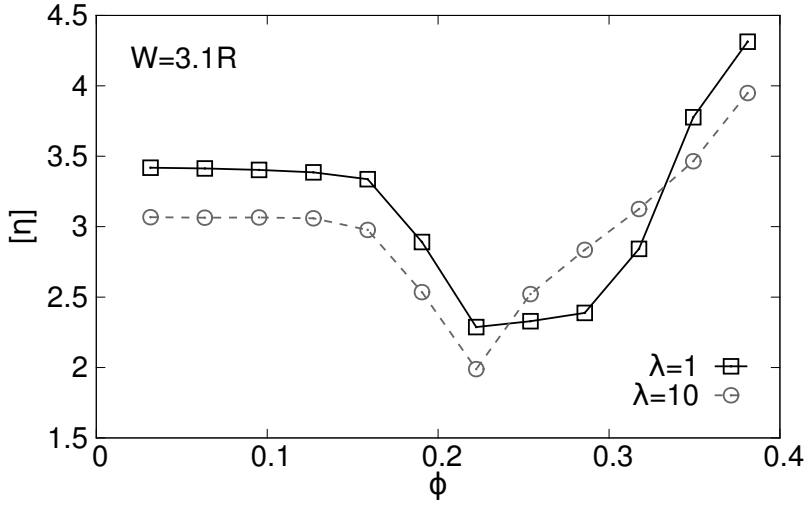

Figure 3.16: Normalized viscosity of a vesicle suspension as a function of concentration for low and high viscosity contrast. $W = 3.1R$

For a weak enough confinement ($W = 6.3R$, Figure 3.13), the vesicles with $\lambda = 1$ form single ordered file for small ϕ. For larger ϕ a single file is unstable and is destroyed in a somewhat disordered fashion. In the case of $\lambda = 10$ we have a single file, with some tumbling events accompanied with the relative motion between vesicles. When ϕ reaches a critical value, the single file is destroyed in favor of disorder, in a quite similar way as for the case of $\lambda = 1$.

3.6 Rheology of vesicle suspension

Once the spatial organization has been discussed, we are in a position to establish a link between this organization and rheology. A property that is commonly of interest for unbounded suspensions is the viscosity as a function of the volume fraction ϕ. In the dilute regime, when hydrodynamic interactions between suspended entities can be neglected, the viscosity of suspension takes the generic form $\eta = \eta_{ext}(1 + \alpha\phi)$, where η_{ext} is the viscosity of the suspending fluid and α is the so-called intrinsic viscosity, that depends on the properties of the suspension. For example, α is equal to 2.5 for rigid sphere (in an unbounded domain), which is the famous Einstein result. α was calculated by Taylor for emulsions [Taylor, 1934] and extended to vesicle suspensions more recently [Misbah, 2006]. When the volume fraction increases, hydrodynamic interactions among suspended entities have to be taken into account, leading to an increase of the suspension viscosity. The classical picture is that there is "jamming" accompanied by a divergence of the viscosity at the maximum volume

fraction ϕ_m corresponding to close packing. A commonly used phenomenological law for rigid particles is that of Krieger and Dougherty $\eta = \eta_{ext}(1 - \phi/\phi_{ext})^{-\alpha\phi_m}$ [Krieger and Dougherty, 1959]. The normalized viscosity $[\eta] = (\eta - \eta_{ext})/(\eta_{ext}\phi)$ increases monotonically with ϕ. In a confined vesicle suspension, it will be shown that the ordering configuration due to the confinement can lead to a very different behavior of the rheology.

We shall determine below the effective viscosity of the suspension. It is defined as $\eta =< \sigma_{xy} > /\dot{\gamma}$, where σ_{xy} is the wall shear stress. The symbol $< ... >$ designates here a double average over the bounding wall and over time. The shear stress tensor σ_{xy} in LBM can be expressed in terms of the distribution functions as [Krüger et al., 2009]

$$\sigma_{xy} = -\left(1 - \frac{1}{2\tau}\right) \sum_i c_{ix} c_{iy} \left(f_i - f_i^{eq}\right) \tag{3.1}$$

First we investigate the behavior of $[\eta]$ and η with ϕ for $\lambda = 1$ (Figure 3.14 and Figure 3.15). In the dilute regime ($\phi < 16\%$ for $W = 3.1R$, $\phi < 8\%$ for $W = 4.7R$ and $\phi < 5\%$ for $W = 6.3R$), the single file configuration with an equilibrium distance between two neighbors leads to a plateau of $[\eta]$. This means that the effective viscosity η is linear with ϕ. In this regime the vesicles interact very weakly with each other and this weak interaction is not significantly reflected on the rheology. Note that the dilute regime definition depends on W: the interval of ϕW over a dilute regime is higher for small W than for large W. The reason is that when W is small the hydrodynamic interaction is screened by the presence of the walls (recall that the velocity field created by a force at a given point decays exponentially with X/W). The smaller W, the stronger the decay.

At larger ϕ, the semi-dilute regime ($\phi < 22\%$ for $W = 3.1R$, $\phi < 15\%$ for $W = 4.7R$ and $\phi < 10\%$ for $W = 6.3R$), $[\eta]$ decreases in a quasi-linear manner (Figure 3.14), while η exhibits a plateau around that concentration (Figure 3.15). This means that the confinement has dramatically altered the rheological behavior. In this regime, the additional vesicles (an increase of ϕ) reduce the distance between two neighbors. Each insertion of a new vesicle destroys a large vortex and creates a vortex with a smaller amplitude as shown the region I and II in Figure 3.11 and Figure 3.12. This explains the collapse of $[\eta]$ with ϕ. When the single file is saturated, an additional vesicle will not be able to integrate the file and will wander in the fluid gap surrounding the file. This wandering close to the walls will create more resistance against the overall flow, and thus $[\eta]$ shows a sudden increase within a very narrow interval of ϕ while the η also increases fast with ϕ after the plateau. The saturation of a single file is a precursor for its instability in favor of either the formation of a doublets (strong confinement, $W = 3.1R$ in Figure 3.11), or the formation of two files (intermediate confinement, $W = 4.7R$ in Figure

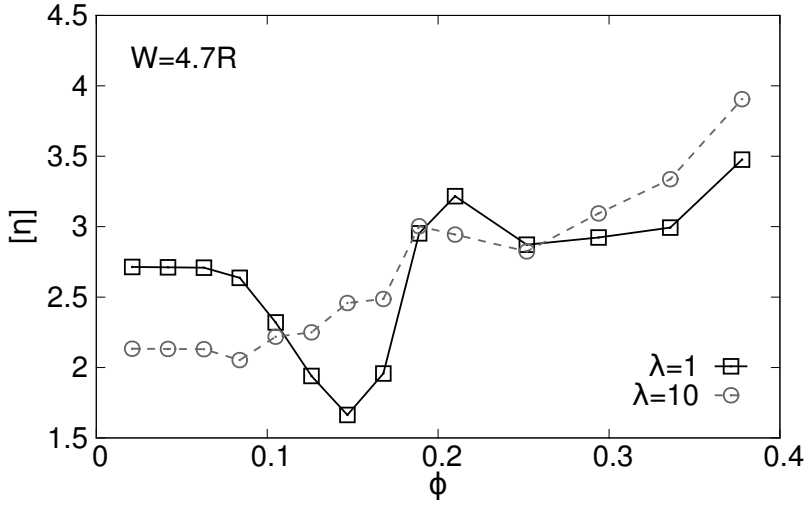

Figure 3.17: Normalized viscosity of a vesicle suspension as a function of concentration for low and high viscosity contrast. $W = 4.7R$

3.12). In the first case, we have a formation of doublets and this always leads to an increase of $[\eta]$. The doublet formation is accompanied by a stronger dissipation within the (thin) fluid gap separating the two vesicles in the doublet. Indeed, within that gap the two membranes tank-tread in opposite directions, which generates a quite significant dissipation. The situation in a weaker confinement ($W = 4.7R$ in Figure 3.12, $W = 6.3R$ in Figure 3.13) is significantly different. When the single file is saturated, here also there is first a sudden increase of $[\eta]$ in a narrow interval $\phi \in [15\%, 21\%]$ for $W = 4.7R$ and $\phi \in [10\%, 12\%]$ for $W = 6.3R$, due to wandering of a single vesicle in the fluid gap. Once ϕ is increased beyond this interval, instead of doublet formation (as happens for $W = 3.1R$), the file splits into two files disposed symmetrically with respect to the centerline ($W = 4.7R$). Addition of new vesicles will be inserted into either of the two files, destroying larger vortices in favor of smaller ones, precisely as in the single unsaturated file regime. This destruction of larger amplitude vortices lowers the dissipation and the normalized viscosity of the two-file regime shows a decrease with ϕ. There is however, another source of dissipation which is due to the sliding of the two files against each other, so that a further increase of ϕ will lead to an increase of $[\eta]$. For a weaker confinement ($W = 6.3R$) the ordered nature of the suspension is less pronounced, leading to a weaker decrease of $[\eta]$ in the range $\phi \in [12\%, 15\%]$, before an increase for higher values of ϕ where a disordered structure prevails.

A comparison of normalized viscosity between low and high viscosity contrast suspension is plotted in Figure 3.16, Figure 3.17 and Figure 3.18. In the strong confinement ($W = 3.1R$), these two situations exhibit tank-treading and form similar

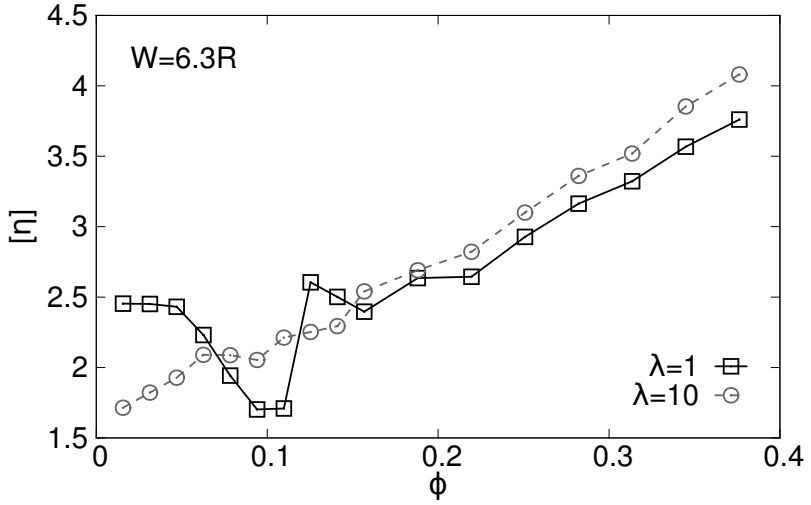

Figure 3.18: Normalized viscosity of a vesicle suspension as a function of concentration for low and high viscosity contrast. $W = 6.3R$

orderings of vesicles. Thus a similar behavior of rheology is obtained.

It is noticed that the normalized viscosity for λ=10 is smaller than for λ=1 in the one file configuration regime (i.e. $[\eta]$ in the small ϕ regime where there is a plateau). This result might at first glance seem counter-intuitive since the fluid inside the vesicles is more viscous (it is 10 times more viscous than before). A close inspection shows that the tank-treading angle for $\lambda = 10$ is smaller than that for $\lambda = 1$ so that in the $\lambda = 10$ case the vesicles are more aligned with the flow. This explains the origin of less dissipation and its impact on overall rheology. However, for $W = 6.3R$, because the stability of a single file is broken by tumbling, the normalized viscosity exhibits an increase with ϕ instead of the plateau of $[\eta]$ obtained for stronger confinement ($W = 3.1R$ and $W = 4.7R$). In semi-dilute regime, the occurrence of tumbling suppresses the collapse of $[\eta]$ observed for $W = 4.7R$ and $W = 6.3R$ after the plateau regime in the case of $\lambda = 1$. In the quite concentrated regime, say beyond about 30%, the prevailing configuration are disordered and $[\eta]$ increase with ϕ regardless of the value of the viscosity contrast. Compared with λ=1 suspension, λ=10 suspension shows a larger normalized viscosity $[\eta]$.

To confirm the picture, we conduct a systematic analysis in 3D, on which we provide here only a brief account. We apply an immersed boundary lattice Boltzmann method for capsules. The system size is given by $L_x = 40.5R$, $W = 5R$, and $L_z = 5R$. Periodic boundaries are used along x and z. The cell membrane energy density (per unit area) is composed of the shear elasticity energy $\kappa_s(I_1^2 + 2I_1 - I_2)/12 + \kappa_\alpha I_2^2/12$, where κ_s is the shear elastic modulus and κ_α is the area dilation modulus. I_1 and I_2 are the in-plane strain invariants. $\kappa_\alpha/\kappa_s = 200$

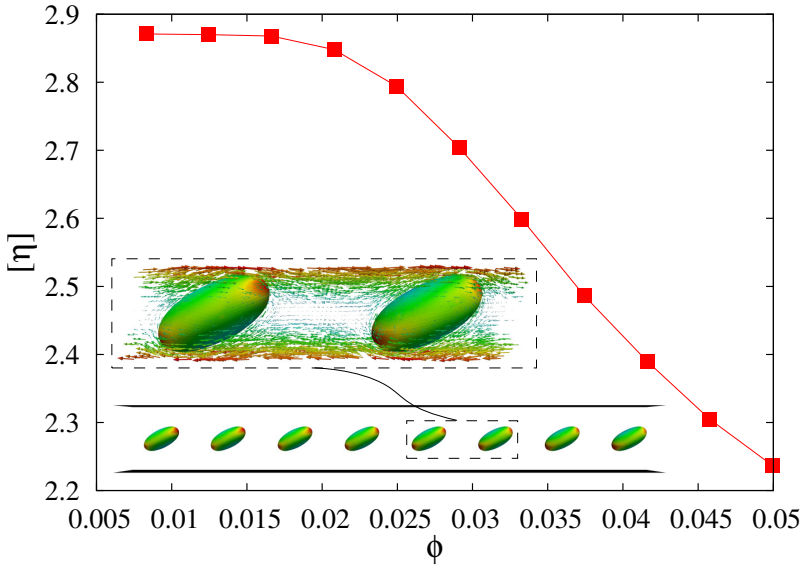

Figure 3.19: Normalized viscosity $[\eta]$ as a function of ϕ and the spatial configuration for $\phi = 3.3\%$. ϕ is the capsule concentration (volume fraction in 3D). Each capsule is steady (center of mass fixed in time) and the membrane undergoes tank-treading, with the velocity field visible on the magnified capsules.

is chosen large enough to preserve local area conservation. The reduced volume $\nu \equiv [V/(4\pi/3)]/[A/4\pi]^{3/2}$ (V and A are the actual volume and the area of the cell) is taken to be 0.9. The viscosity contrast is set to 1. We define the capillary number as $C_s = \eta_0 \dot{\gamma} R/\kappa_s$ with $R = [V/(4\pi)/3]^{1/3}$. In most simulations, $C_s = 0.14$ and the suspended entities exhibit tank-treading motion. The 3D rheology follows the same trends as in 2D, conferring to the present results a robust character. Figure 3.19 shows $[\eta]$ as a function of ϕ and the corresponding spatial organization. Note that both the absolute value and the amplitude of viscosity decrease are comparable to those obtained in 2D. Only one file ordering is obtained in 3D, as a more complex interaction between capsules in the x-z plane results in a different regulation of the ordering structure. This issue will be discussed in the chapter 4.

Chapter 4

Blood crystal in confined shear flow

This chapter is concerned with 3D simulations and experiments in order to investigate the transverse interaction between RBCs and their collective behaviors in confined linear shear flow. The introduction and the methods are presented in Section 4.1 and Section 4.2 respectively. The generation of the crystal-like order of capsules is explained in Section 4.3. Then, possible ordered patterns are discussed in Section 4.4. The effect of confinement and deformability on the ordering is explored in Section 4.5. Finally, Section 4.6 is devoted to the effect of ordering on rheology of the suspension.

4.1 Introduction

A major problem in the study of suspensions is to understand the occurrence of micro-structures and their impact on the overall properties of the suspension, like rheology. Up until now, dilute non-colloidal suspensions, including particulate suspensions, emulsions, blood and so on, under shear flow, are traditionally represented by a disorder-like pattern. Experiments and simulations for non-colloidal suspensions in shear flow have indicated chaotic particle dynamics leading to irreversibility even at a very small Reynolds number[Metzger et al., 2013a; Pine et al., 2005]. Experimental and numerical investigations show that the trajectories of non-Brownian particles exhibit irregular and apparently random displacements, or effective diffusion, when a suspension is sheared unidirectionally between concentric cylinders with the inner cylinder is rotating while the external one is fixed (Taylor-Couette flow). The origin of this irregular motion lies in the interactions between particles mediated by the fluid [Eckstein et al., 1977; Metzger et al., 2013a,b]. The question of whether or not particles can escape disorder and settle into other configurations, like

order, under the sole effect of hydrodynamics, is little addressed [Beatus et al., 2006; Janssen et al., 2012; Shani et al., 2014]. In colloidal dilute suspensions, crystalline-like phases can occur [Ackerson and Pusey, 1988; Cheng et al., 2012; Schall et al., 2007; Wu et al., 2009] and are stabilized by Coulomb interactions due to surface electric charge. In non-colloidal system, in the presence of parallel walls or with a square cross section, self-organization due to hydrodynamic interactions have been reported [Baron et al., 2008; Beatus et al., 2007; Goto and Tanaka, 2015; Humphry et al., 2010; Lee et al., 2010]. By conducting systematic simulations of a suspension of RBC model in confined shear flow, we discover the occurrence of a crystalline-like phase of RBCs which is only regulated by hydrodynamics. This self-organization takes place when the RBCs perform tank-treading. In addition to tank-treading we find that the presence of walls plays an essential role in this self-organization.

A complex behavior is discovered, where RBCs can undergo both repulsion and attraction in a subtle way and the interplay between a long range attraction and a small range repulsion is able to stabilize the RBCs into an equilibrium state with ordered pattern. We shall see that the investigation of two body interaction serves as a useful basis in order to identify the basic mechanism of self-organization process.

A tank-treading RBC produce a quadrupole-like flow in the center plane, which provides the attractive and repulsive forces leading to the self-organization of the RBCs. The nature of this interaction depends both on the deformability of the particles and on the confinement. We shall see that if rigid particle suspension are considered under the same conditions, then order disappears in favor of disorder. T. Fischer, who has spent several months in our Institute to perform a systematic experimental study on confined RBCs under shear flow has found several interesting experimental results which comply with our simulations, as we shall describe in this chapter.

4.2 Methods and parameters

4.2.1 Experimental setup

The experiments were performed in a home-made rheoscope with cone-plate geometry. The observation of suspended cells was along the gradient of the shear flow using an inverted microscope (Diavert, Leica Microsystems GmbH, Wetzlar, Germany) with interference contrast optics (40/0.75). Microscopic images were taken with a CCD Kamera (DMK 41BF02.H, The Imaging Source Europe GmbH, Bremen, Germany). Normal blood samples were obtained from the EFS (Etablissement Francais du Sang) and kept refrigerated until use. Solid spherical particles were produced by suspending red cells in an isotonic solution of sodium salicylate (Sigma-Aldrich) thus converting the biconcave red cells into spheroechinocytes. This shape was then

conserved by fixation with 0.25% glutaraldehyde (Alfa Aesar, Karlsruhe, Germany). Red cells and fixed spheres were washed three times with isotonic PBS (Dulbecco, biowest, Nuaille, France). Red cells or spheres were suspended in an isotonic solution of dextran (MW 500000 D, figma-Aldrid, saint-Queutiu Fallavier, France) plus PBS. Its viscosity at room temperature (25°C) was 50mPas (Anton Paar, Rheoplus, graz, Austria). Suspensions of red cells or spheres were prepared with volume fractions between 0.002 and 0.01 and were loaded into the cone-plate chamber.

4.2.2 Simulation method

In simulations, the lattice Boltzmann method (LBM) was used to solve the quasi-incompressible Navier-Stokes equations for fluid flow [Krüger, 2012]. The deformable particle is described as a capsule with a closed massless membrane. The membrane is discretized into 1620 triangle elements. The natural shape of the particle without external force is a sphere with radius R. The shear elasticity energy is given by Skalak law $\kappa_s(I_1^2 + 2I_1 - I_2)/12 + \kappa_\alpha I_2^2/12$, where κ_s is the shear elastic modulus and κ_α is the area dilation modulus. I_1 and I_2 are the in-plane strain invariants. $\kappa_\alpha/\kappa_s = 30$ is chosen large enough to preserve local area conservation. The immersed boundary method (IBM) was used to couple of fluid flow and particle deformation [Krüger, 2012]. This allows to distribute the forces on membrane nodes to nearby fluid nodes, thereby avoiding an explicit representation of the interface while permitting to access to the dynamics of particle deformation and motion.

4.2.3 Parameters in simulation and experiment

As shown in Figure 4.1 A, the particles are sheared between two rigid plane walls located at $X = -W/2$ and $X = W/2$. The flow is applied along Z direction. Y direction is called as transverse direction in this work. The system is periodic along the Y and Z direction. The computational domain for Y direction (L_Y) is fixed at 18R. There are two sizes of computational domain along Z direction (L_Z), $25R$ for diluted suspension and $18R$ for concentrated suspension. Along X direction, We explore the confinements by changing the distance between two walls (W) from $2.4R$ to $4.9R$. The concentration is calculated by the volume fraction $\phi = N_{RBC}(4\pi R^3/3)/(L_Y L_Z W)$, where N_{RBC} is the total number of particles in the system. The shear capillary number is defined as a ratio of typical shear stress magnitude to the characteristic particle elastic stress: $C_{as} = \eta_{ext}\dot{\gamma}R/\kappa_s$, η_{ext} is the viscosity of suspending fluid. In all the simulations, $C_{as}$is set to 0.05 (with shear elastic modulus set to $4\mu N/m$) and the typical radius is chosen as R equal to 4μm. In experiments, the shear rate varies from 15 to $60s^{-1}$, and C_{as} is approximately in a range of 0.8-3. The reason for a higher capillary number in experiments is that the RBCs in experiments are significantly more deflated than in simulations

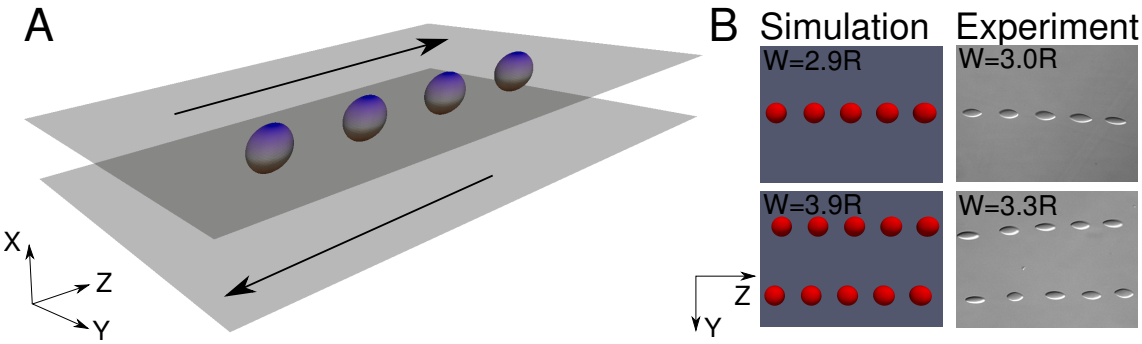

Figure 4.1: A: The schematic of simulation model. Z direction is the shear flow direction, X direction is the shear gradient direction and Y direction is the transverse direction. B: Both of simulations and experiments show configurations of particles as strings along the flow direction.

and thus they require a higher shear rate in order to maintain them in the tank-treading regime. The viscosity contrast as a ratio of viscosity between internal fluid of particle and external fluid is fixed to 1 in simulations and is about 0.4 in experiments (hemoglobin solution of healthy RBC being around $20mPa.s$ at room temperature 25°C) [Kelemen et al., 2001]. In both of simulation and experiment, the dynamic of particles exhibits a tank-treading. We define Reynolds number as $Re = \rho\dot{\gamma}R^2/\eta_{ext}$, which is set to 0.5 in all simulations and its magnitude of about 10^{-5} in the experiments.

4.3 Birth of a flow-aligned string ordering

When deformable particles, like capsules, vesicles, RBCs etc. are suspended in the fluid sheared between two rigid planes, the particles firstly follow the shear flow with a tank-treading motion of the membrane. The intercellular interaction makes a shift in the trajectory of the particles by pushing away each other when they are getting close, which causes the so-called shear induced diffusion in the suspension. In the meantime, the lift from the walls forces the particles going to the center plane between the two walls and stop in the center due to the symmetry. If the suspension is diluted enough to allow all the particles to stay in the center, then once they settle in the center, the particles organize themselves thanks to hydrodynamics interactions. The crystalline-like orderings of the particles are observed in both numerical simulations and experiments. The typical and most probable configurations of the particles, flow-aligned strings, are shown in Figure 4.1 B.

In order to get further insight towards understanding how the interactions organize the particles, we implement the numerical simulations by using the system

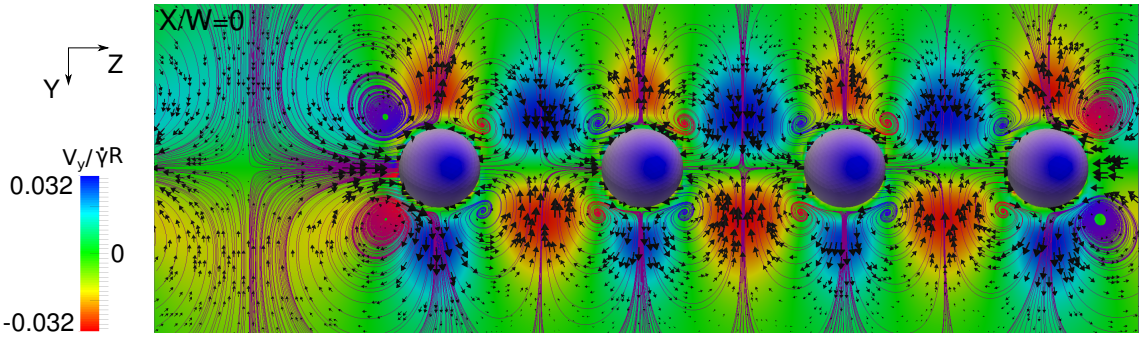

Figure 4.2: The flow field around the particles in the central plane. Recall that the flow is along Z, while the rigid walls are located at $X = \pm W/2$.

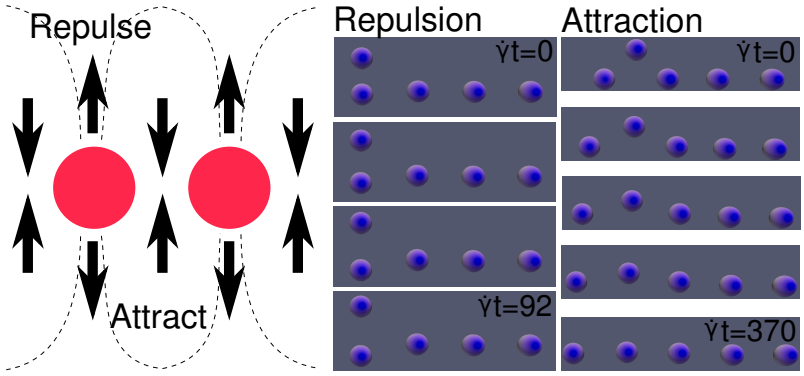

Figure 4.3: A schematic of repulsive regime and attractive regime for a flow-aligned string configuration of particles. Simulations show the motion of particles in repulsion and attraction. The confinement is $W = 2.9R$.

shown in Figure 4.1 A. We firstly study the flow field in the central plane when a string of four particles is formed in a confinement of $W = 2.9R$. Figure 4.2 gives the in-plane velocity vectors, which exhibit the flow coming from the particles and returning back to the gap between the particles. With this kind of induced flow, the string is expected to provide repulsive and attractive force to the nearby particles. Figure 4.3 schematically gives the repulsion regime where an inserted particle will be pushed away from the string, and an attraction regime where an inserted particle will be pulled into the gap. We have numerically tested the repulsion and attraction by inserting an additional particle either on top of a pre-existing particle or in a gap between two particles along the string. As shown in Figure 4.3, in the first case we have a repulsion, while in the second case we have an attraction.

We will now show that analyzing a two body interaction problem provides a certain basis towards understanding of the self-organization process of multi-particles. Consider first a single particle in the tank-treading regime. This particle induces a

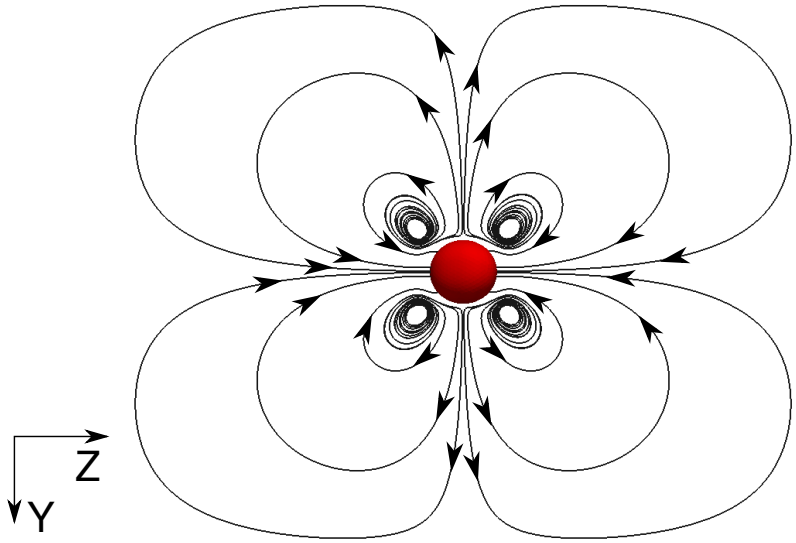

Figure 4.4: The flow field around a single tank-treading particle in the central plane. The structure of the flow shows a quadrupole-like form. Recall that the flow is along Z, while the rigid walls are located at $X = \pm W/2$.

quadrupole-like flow field in the central plane as shown in Figure 4.4. The two body interaction amounts to interactions between two quadrupoles. Two situations can occur depending on the relative position between two particles. Consider case A in Figure 4.5. There the particles are separated along transverse direction and flow to the computational boundary. We have a repulsion. In case B, the particles get close along transverse direction and form a string along the flow direction with a constant equilibrium interdistance. In this case we have an attraction. By exploring different initial relative positions of the particles in simulations, we qualify the regime of repulsion and attraction as given in Figure 4.5. This Figure also shows examples of the evolution of the relative trajectories between particles in the repulsion and attraction regimes. It is noticed that the regime of attraction is much larger than the regime of repulsion, which means that the attraction plays a main role in the transverse interaction. Thus we have a larger probability to observe particles form flow-aligned strings.

4.4 Patterns of crystal-like ordering

Since the repulsion and attraction depends on the relative positions of each particle, additional particles can added to the two particle system with some special positions, and by tuning their position we can balance the repulsive and attractive forces. By this way we can obtain several possible stable configurations for three,

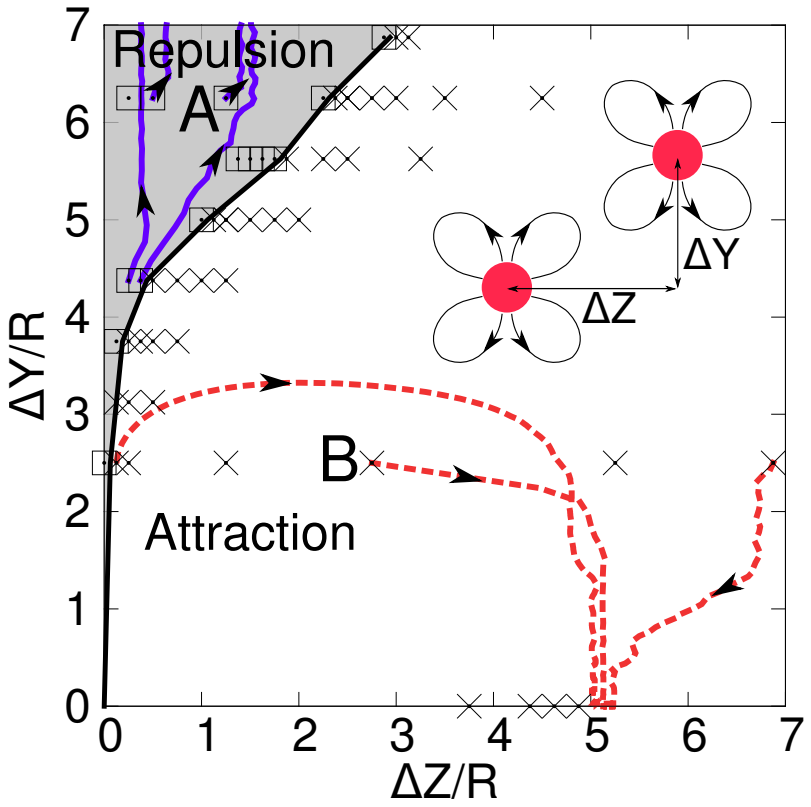

Figure 4.5: The qualitative regime of repulsion and attraction for transverse interaction between two particles with confinement of $W = 2.9R$. Some examples of the relative trajectories between two particles are plotted by solid line for repulsion and dashed line for attraction. With the initial positions in gray region the two particles exhibit repulsion, while they exhibit attraction with the initial positions in white region. The inset shows a schematic of the interacting particles.

four and five particles, as shown in Figure 4.6. These orderings are all symmetrical about the flow direction. It is expected that various orderings can be found for a larger number of particles. The stability of these configurations are examined by making a small perturbation to the equilibrium position. The simulations show that the particles go back to the equilibrium position. However, to get an ordering different from the strings pattern (which seems to have the largest basin of attraction), the initial relative positions should be close enough to the equilibrium configuration. For example, in the case of $N_{RBC} = 3$ and $W = 2.9$, we performed 60 simulations with random initial positions, 75% of the final states show a string ordering, while in the other cases the particles are pushed to computational boundary and no ordering is found. The triangular ordering was not observed in those 60 simulations, except if the initial positions are adequately chosen close enough to the equilibrium

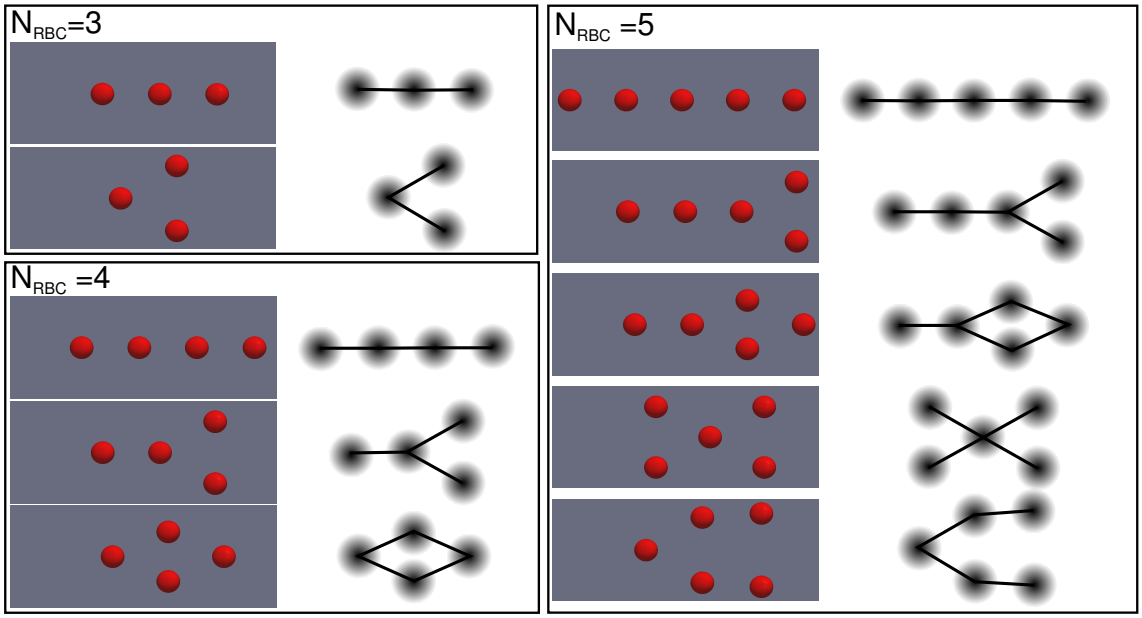

Figure 4.6: All possible patterns of the ordering of 3, 4 and 5 interacting particles with confinement $W = 2.9R$.

configuration.

Consider now a higher concentration regime. Figure 4.7 shows typical results. Additional particles make them extrude each other and tend to force others depart from the center plane. With strong confinements, the particles can still be kept in the center plane with an adaptive ordering to balance the interactions between particles. In Figure 4.7, we show some orderings for high concentration in strong confinements ($W = 2.9R$ and $W = 3.9R$). Most of the results give a configuration with several moving strings ($W = 3.9R, Act = 16\%$). Act is the particle area fraction in the central plane, which is calculated by the total area of the particle cross section in the simulation domain divided by the area of that. Other types (than parallel chains along flow) of static orderings are also found, as for $W = 2.9R, Act = 23\%$ and $W = 3.9R, Act = 23\%$. When the confinement decreases, the wall effect weakens, so that particles can escape from the center towards the periphery, and a disordering configuration prevails. In the case with $W = 3.9R, Act = 12\%$ in simulation and $W = 4.6R, Act = 6\%$ in experiment, a local disordering is found in one of the strings. When the string has packed maximum particles, an insertion of additional particle forces other particle to leave the center plane, destroying thereby the ordered string. In the case of $W = 4.9R, Act = 22\%$ in simulation and $W = 6.1R, Act = 18\%$ in experiment, the weak confinement and high concentration cause the particles to never stop in the center plane, thus no ordering is observed in these situations.

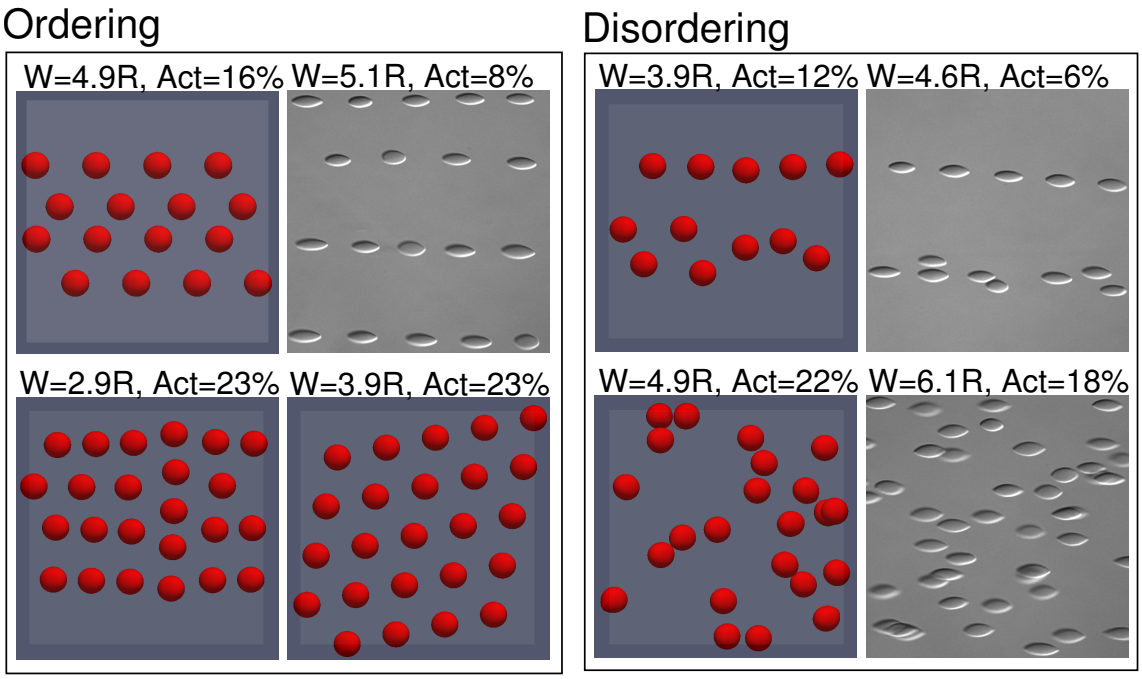

Figure 4.7: In concentrated suspension, particles are ordered with strong confinement and disordered with weak confinement. *Act* is the particle area fraction in the central plane.

4.5 Effect of confinement and deformability

To measure the effect of confinement on the ordering, we determine the interdistance between two and three particles by changing the distance between the two walls. Figure 4.8 A and C show the equilibrium distance between two particles, which shows a linear increase with W and the corresponding configurations both in simulations and experiments. The generation of the equilibrium state comes from the fact that in the shear plane, the tank-treading induced flow bounces back at the wall and produces an equilibrium position along the flow direction, as discussed in detail in Chapter 3. When W increases, the bounce-back flow appears at larger distances away from the particle. Since the only length scale is W, we expect the interdistance to scale with W. This is what we find indeed, both by numerical simulation and experimentally (Figure 4.8 A and C). Figure 4.8 B and D shows the case of triangular ordering, where the interdistance along the flow direction (ΔZ) also exhibits a linear relationship with W. The triangular ordering is formed thanks to an interplay between repulsion in some position and attraction in other positions, as discussed earlier. When W increases, the increase of ΔZ makes the attractive force on the two symmetrical particles decrease, which make them repel each other in the transverse

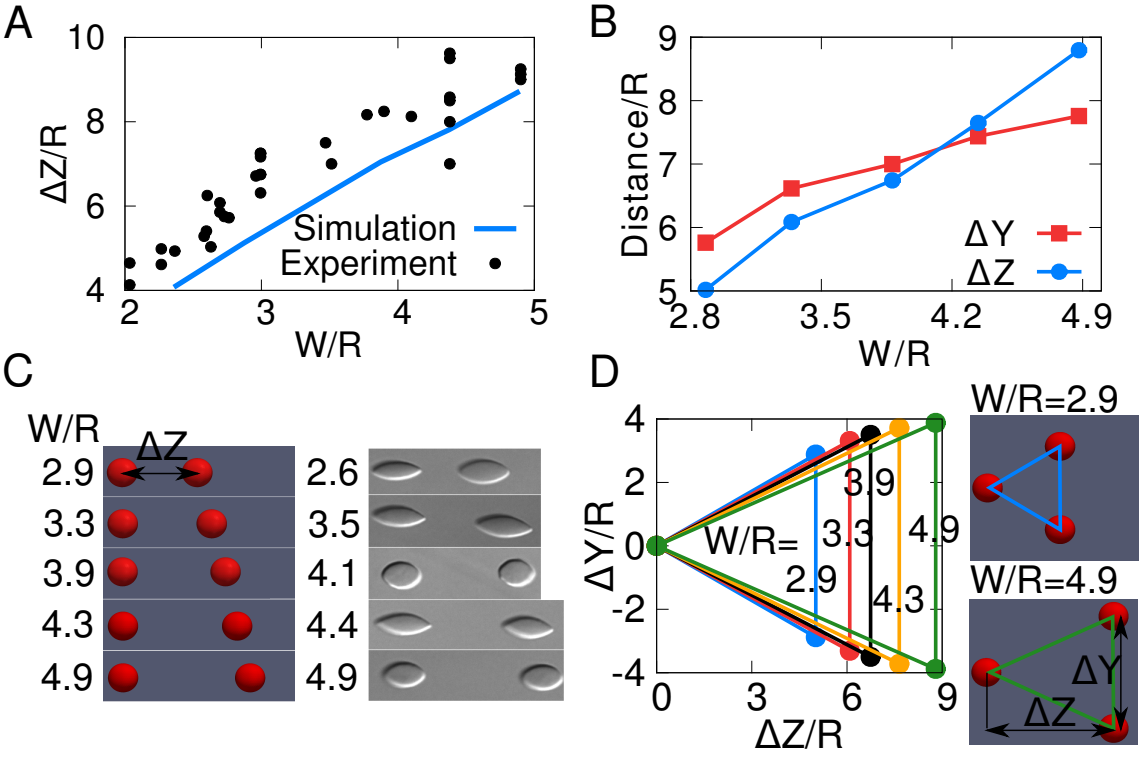

Figure 4.8: Effect of confinement on the configuration. A: Equilibrium distance between two particles increase with W. B: Size of triangle configuration increase with W linearly. C: Configurations of two particles for different confinements corresponding to A. D: Configurations of three particles for different confinements corresponding to B.

direction towards new positions with larger ΔY.

The effect of deformability on the ordering has been analyzed and the results are reported in Figure 4.9. Five particles are considered in the simulation with $W = 4.9R$, and for each case studied we considered the same initial positions. For deformable particles, due to the lift from the walls, cells are pushed towards the center and form a string as shown in Figure 4.9 C, and discussed earlier. For rigid particles, in small Reynolds number flow ($Re = 0.05$), as shown in Figure 4.9 A and B, the distance between two given particles always evolves in the course of time, the particles do not settle in the center plane (due to the absence of lift force), so that disorder prevails (Figure 4.9 F).

We have performed experiments by hardening RBCs (see the experiment setup in Section 4.2). Because Re is very small in the experiment, the lift force on these rigid RBCs is practically absent. We never observed orderings for these rigid RBCs (Figure 4.9 G). These results agree with our simulations, and support the idea that

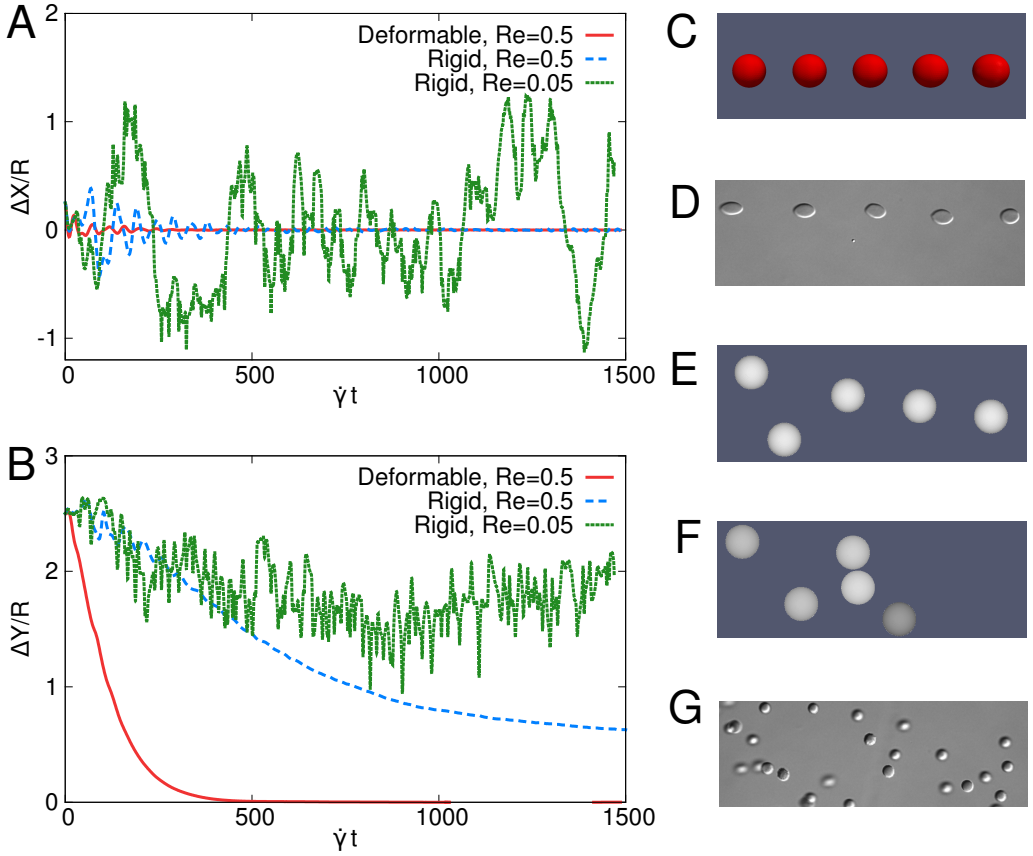

Figure 4.9: A: Distance in X direction between two selected particles among five particles when they are sheared in the flow. B: Distance in Y direction between two selected particles. C-G: Configurations of particles for each case: C: Simulation, $W = 4.9R$, $C_{as} = 0.05$, $Re = 0.5$ D: Experiment, $W = 4.9R$, $C_{as} = 0.7$, $Re \sim 10^{-5}$ E: Simulation, $W = 4.9R$, rigid particle, $Re = 0.5$ F: Simulation, $W = 4.9R$, rigid particle, $Re = 0.05$ G: Experiment, $W = 4.5R$, rigid particle, $Re \sim 10^{-5}$

the wall lift force (and thus confinement) plays an essential role in the ordering process.

For completeness, and in order to highlight the role of the lift force, we have increased in simulations the inertial effect, and have taken $Re = 0.5$. There is now a lift force of inertial origin that pushes the rigid particles towards the center, where the particle settle in with small vertical oscillations (dashed line in Figure 4.9 A). However, despite the location of the particle in the center we do not see order. The reason is as follows. The transverse interaction between rigid particles is much weaker than in the case of deformable particles, and order is quite fragile. The dashed line in Figure 4.9 B shows that the distance between two rigid particles,

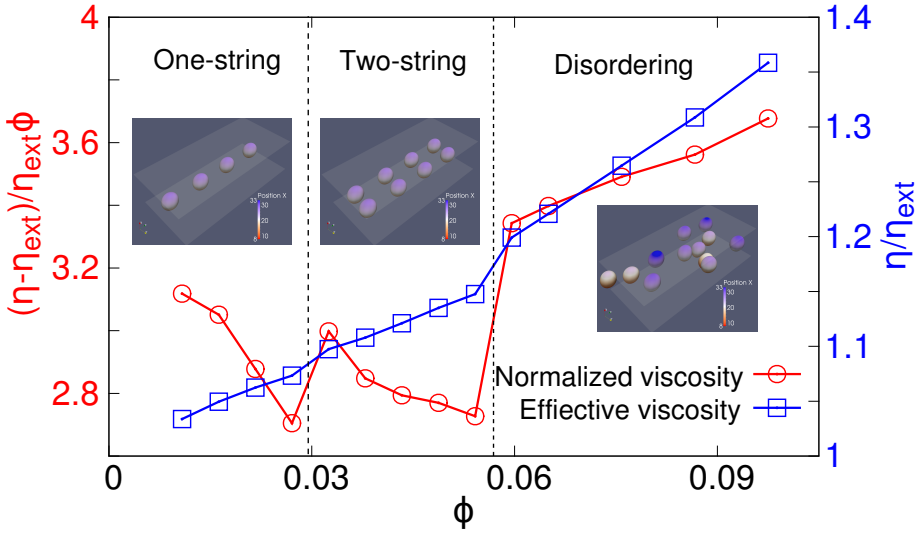

Figure 4.10: Viscosity of deformable particle suspension changes with concentration in shear flow with confinement $W = 4.9R$. The normalized viscosity shows a decrease with increasing concentration when string ordering is formed.

can attain, in some cases, a steady value, leading to some kind of ordering (Figure 4.9 E), albeit not a straight string, in contrast to deformable particles.

4.6 Effect of ordering on rheology

Finally, we briefly discuss the influence of ordering on the rheology of deformable particle suspensions. We have already seen that the string ordering leads a decrease of intrinsic viscosity (or more precisely the normalized viscosity) with increasing suspension concentration in the 2D case. In the 3D case, different orderings are possible, as discussed above. All these orderings have a direct effect on rheology of the suspension. As discussed before, the highest probability of the ordering pattern consist in straight strings. To simplify the question, a small enough computational domain is used here, with $L_Y = 9R$, $L_Z = 18R$ and $W = 4.9R$. In this case, we find a reduced number of configuration: a single string in the dilute regime, two parallel strings for intermediate concentration increase, and disorder for higher concentration. The results are presented in Figure 4.10. We see that the normalized viscosity shows intervals with decreasing trends when ϕ is such that order prevails. When disorder prevails, the normalized viscosity increases with ϕ.

Chapter 5

Inversion of hematocrit partition at microfluidic bifurcations

In this chapter, we perform 2D simulations and microfluidic experiments to investigate the partition of red blood cells at T-shaped bifurcations. The introduction and methods of this work are given in Section 5.1 and Section5.2 respectively. In Section 5.3, we talk about the influence of viscosity contrast on the partition. In Section 5.4, we report on an inversion of Zweifach-Fung effect in diluted case and explain it by the structure of RBCs files in the feeding vessel.

5.1 Introduction

Blood flows through a complex network of the circulatory system – from large arteries to very tiny capillaries – in order to ensure oxygen delivery and to remove metabolic waste. This task is mainly carried out by red blood cells (RBCs) that are remarkably deformable, in healthy conditions, and therefore able to squeeze into tiny capillaries. A change in rheological and flow properties of blood is often associated with hematological diseases or disorders [Fedosov et al., 2011a] (e.g. sickle-cell anemia, malaria, polycythemia vera). Understanding blood flow and its dependence on the mechanical properties of its constituents may improve and lead to new applications in biomedical technology, for example in blood substitutes development and transfusion techniques.

A major open problem in blood circulation is to understand the perfusion in the vasculature networks, especially in the microvasculature where RBCs accomplish their vital functions. For example, an improper hematocrit distribution is observed in heart microcirculation with consequences such as occlusion zones (within many patients with apparently healthy coronary arteries). These abnormal traffic zones cause a lack of oxygen supply to tissues that leads to cardiac ischemic disease [Cokki-

nos et al., 2006]. The precise origin of this dysfunction is still a matter of debate. The principal mechanism that dictates blood heterogeneity in the microvascular networks is the hematocrit partition at the level of bifurcations. RBCs do not behave as passive tracers. Their shape flexibility and dynamics have a decisive role because their size is comparable to that of blood capillaries. A well known phenomenon in microcirculation is the Zweifach-Fung effect [Dellimore et al., 1983; Fenton et al., 1985; Guibert et al., 2010; Pries et al., 1989]: If we consider a bifurcation (as in Figure 5.1), the child branch with the lower flow rate is depleted in RBCs as compared to the parent vessel, while the other, higher flow rate child branch is enriched. That is, if in the parent vessel the total volumetric flow rate is Q_0 and the RBC volumetric flux is N_0, and in the child branch with the lower flow rate this flow rate is Q_1 and the RBC flux N_1, then $N_1/N_0 < Q_1/Q_0$. When the flow rate is sufficiently small, the hematocrit in the child branch can even drop down to zero, while it reaches high values in the other branch. Obviously, this phenomenon has physiological consequences as it alters the transport of oxygen and other essential metabolites, and may even trigger pathological disorders (e.g. occlusions in high hematocrit regions where the viscosity is higher and cell adhesion is favored).

Previous studies have investigated the impact of the confinement [Barber et al., 2008; Chien et al., 1985; Doyeux et al., 2011b; Fenton et al., 1985], the bifurcation geometry [Audet and Olbricht, 1987; Hyakutake and Nagai, 2015; Roberts and Olbricht, 2003, 2006; Woolfenden and Blyth, 2011], the hematocrit [Ditchfield and Olbricht, 1996; Fenton et al., 1985; Roberts and Olbricht, 2003; Yin et al., 2013], and the RBCs deformability [Barber et al., 2008; Li et al., 2012; Xiong and Zhang, 2012; Yin et al., 2013] and aggregation [Sherwood et al., 2012; Yin et al., 2013]. Most of these parameters influence RBCs distribution in the feeding flow, which is believed to dictates the partition at the bifurcation [Doyeux et al., 2011b; Fenton et al., 1985; Li et al., 2012; Yin et al., 2013]. The Zweifach-Fung effect results from the existence of a cell free layer (CFL) close to the walls, which is only occupied by plasma. The feeding flow is divided by a separating streamline into two parts, one feeding the low flow rate branch and the other feeding the high flow rate branch. Due to the CFL, the RBC fraction entering the low flow rate branch is smaller compared to the original RBC fraction in the total feeding flow. The depletion in the low flow rate branch is accompanied by enrichment in the high flow rate branch. In addition to the CFL as the main cause of the Zweifach-Fung effect, it has been argued that there is a relatively small counteracting effect where cells entering the bifurcation tend to be displaced towards the low flow rate branch compared to fluid streamlines (a fact that slightly reduces the Zweifach-Fung effect) [Barber et al., 2008; Doyeux et al., 2011b; Li et al., 2012; Ollila et al., 2013], but this question is still debated [Hyakutake and Nagai, 2015; Xiong and Zhang, 2012].

The existence of a CFL is a consequence of the lateral migration of RBCs towards the vessel center. This migration is a result of the wall-induced lift force due to

hydrodynamic interactions [Callens et al., 2008; Cantat and Misbah, 1999b; Grandchamp et al., 2013], that depends on the nature of RBC dynamics (like tank-treading or tumbling [Abkarian et al., 2007; Dupire et al., 2012]). The final distribution of RBCs in a confined straight vessel is not only due to the lift force, but it is also influenced by other factors: (i) The curved velocity profile of the Poiseuille flow [Coupier et al., 2008b; Farutin and Misbah, 2014; Katanov et al., 2015; Shi et al., 2012], and (ii) The cell-cell hydrodynamic interactions [Grandchamp et al., 2013; Hariprasad and Secomb, 2014; Katanov et al., 2015; Krüger et al., 2014; McWhirter et al., 2009].

In the present work, we study the hematocrit partition at bifurcations using two-dimensional lattice Boltzmann simulations, whose outcomes are validated and supported by microfluidic experiments. We show that RBCs deformability strongly impacts partition as long as the hematocrit is below 20% (within the normal range in microcirculation). RBC deformability is governed by several parameters such as membrane stiffness (shear, dilatation and bending elastic moduli), swelling degree, membrane viscosity and the viscosity contrast between the hemoglobin and the suspending fluid. Here we choose to tune the deformability through the latter parameter, the viscosity contrast, that controls the RBC dynamics (tank-treading, tumbling or swinging) then all the migration mechanisms at the origin of the CFL. On the other hand, and more importantly, this study reveals that hematocrit partition can be completely reversed, that is the low flow rate child branch can be enriched in RBCs compared to the parent vessel. This newly reported effect is an outcome of a subtle RBCs structuration in the microcirculatory system. This highlights the importance of the notion of RBCs spatiotemporal organization as the main non-negligible ingredient to further understand blood perfusion in the microvasculature. Figure

5.2 Methods and parameters

5.2.1 Design of the microfluidic bifurcations

In both simulations and experiments, we use T-shaped bifurcations such as shown in Figure 5.1: A parent channel divides into two child branches with the same width, but with different lengths L_1 and L_2 ($L_1 > L_2$). The ratio of the flow rates in branches 1 and 2 is then given by $Q_1/Q_2 = (\eta_2 L_2)/(\eta_1 L_1)$, where η_1 and η_2 are the apparent viscosities of the suspension in branches 1 and 2, respectively. For dilute suspensions, where the viscosity is close to that of the suspending fluid, we simply have $Q_1/Q_2 = L_2/L_1$. In simulations, we set the width of the channels to $W = 20\mu$m and we vary L_1/L_2 from 1.43 to 3. In experiments, we have $L_1/L_2 = 3$, $W = 20\mu$m and the height of the channel h is 8 μm. The length of the parent

vessel was chosen as long as possible to allow for the development of a stationary distribution of RBCs across the channel in the feeding flow (5 mm in experiments and 1.5 mm in simulations). Microfluidic channels were produced by standard soft lithography techniques, with molded PDMS bonded to glass. The RBC suspensions were perfused by a syringe pump (KDS Legato 180) and imaging were performed by a video camera (Imaging Source DMK 31AF03) mounted on an inverted microscope with motorized stage (Olympus IX71) and a blue filter (434 ± 25 nm) corresponding to an absorption peak of hemoglobin.

5.2.2 Blood preparation

Blood samples were provided by the Etablissement Français du Sang (EFS Rhône-Alpes) from healthy donors. RBCs were isolated by centrifugation after being washed twice in phosphate buffer saline (PBS) supplemented by 0.1 % bovine serum albumin (BSA). To prevent sedimentation of RBCs in channels, the RBCs were re-suspended in density matching PBS and BSA solutions in a mixture of water and iodixanol (Optiprep from Axis-Shield). This iso-dense solution was used either alone (1.94 mPa.s at 20 °C) or after adding 5% dextran of molecular weight 2×10^6 (viscosity 23.4 mPa.s at 20 °C). The viscosity of the internal hemoglobin solution of healthy RBCs is around 20 mPa.s at 20 °C [Kelemen et al., 2001]. This provides two values of the viscosity contrast λ, namely 10.3 and 0.85. The first value corresponds to blood at 20 °C, while the physiological value at body temperature is around 5-6 [Cokelet and Meiselman, 1968]. Note that we chose to vary the viscosity contrast λ as one way to tune deformability, and therefore the dynamics of lift and hydrodynamic interactions of cells. Stiffening cells using diamide or glutaraldehyde was another possibility. However, from the experimental viewpoint, working with hardened cells at high volume fractions in such a confined environment is quite difficult due to jamming. It would have been nearly impossible to inject a suspension of very stiff cells at hematocrits larger than 10%. Also, the dynamics of glutaraldehyde hardened cells is pure tumbling, which corresponds to very high values of the viscosity ratio λ. We do not expect the dynamics (and therefore phase separation) to change much at values of λ greater than 10 and we found more interesting to increase deformability by decreasing λ rather than trying to investigate less deformable cells (with the experimental difficulties mentioned above).

5.2.3 Hematocrit measurements

Local hematocrit measurements were made by comparing suspension flow images to a reference image without RBC, under identical illumination, and using the Beer-Lambert law of absorption. The absorption coefficient was determined by a calibration with images at low hematocrit, where a direct measurement can be made

by counting individual cells. Hematocrit in branch i will be denoted H_i. In experiments, h is small enough (8μm) so that the flow is quasi two-dimensional. To allow a qualitative comparison with 2D numerical simulations, an area hematocrit ϕ_i was also derived by multiplying the number of cells per unit area by the average cross-sectional area of RBCs (S =19.8 μm^2). H_i and ϕ_i are therefore linked by the relationship $H_i = \phi_i v/(Sh)$, where $v = 90$ μm^3 is the average volume of one cell.

5.2.4 Simulation method

In simulations, we use lattice Boltzmann method (LBM) to compute the fluid flow (see Section 2.2). Each RBC is modeled by 60 nodes interconnected by a potential that allows bending, as well as a stretching modulus that penalizes distance variations between two adjacent nodes. This achieves the RBC membrane incompressibility (see Section 2.4). In other words, we set the spring constant to values as large as possible in order to keep the ratio between the membrane perimeter and area constant. We define the reduced area as $4\pi A/C^2$ (with C is the perimeter and A the enclosed area), which we set to 0.7 to produce a RBCs with a biconcave shape. We use the immersed boundary method (IBM) (see Section 2.3) to couple the fluid flow and RBC deformation. For comparison with experiments, we set the viscosity contrast to $\lambda = 1$ and $\lambda = 10$.

5.3 The role of interactions and viscosity contrast in partition

As a guideline, we shall refer to the empirical law of Pries *et al.* taken from refs [Pries et al., 1989, 1990] that gives the hematocrit partition at a bifurcation:

$$\text{logit}\Big(\frac{H_1 Q_1}{H_0 Q_0}\Big) = \alpha \text{logit}\Big(\frac{Q_1/Q_0 - \beta}{1 - 2\beta}\Big), \tag{5.1}$$

where $\alpha = 1 + 6.98(1 - H_{0_F})/a$, $\beta = 0.4/a$ (with a the tube diameter in microns) and $\text{logit}(x) = \ln[x/(1-x)]$. H_0 is the volumetric hematocrit in the parent feeding branch, while H_1 is the hematocrit in a child branch. H_{0_F} is the feeding hematocrit in a reservoir that would be located right before the narrow feeding vessel. Due to the Fåhræus effect, H_{0_F} is larger than H_0 and a relationship between both quantities is also given in Pries et al. [1990]:

$$H_0/H_{0_F} = H_{0_F} + (1 - H_{0_F})(1 + 1.7e^{-0.415a} - 0.6e^{-0.011a}). \tag{5.2}$$

Figure Note that the partition law (Equation 5.1) has been validated through *in-vivo* experiments with rats (thus at body temperature), with narrow capillaries (of diameters a lower than 30 microns), but with feeding hematocrit higher than 20%.

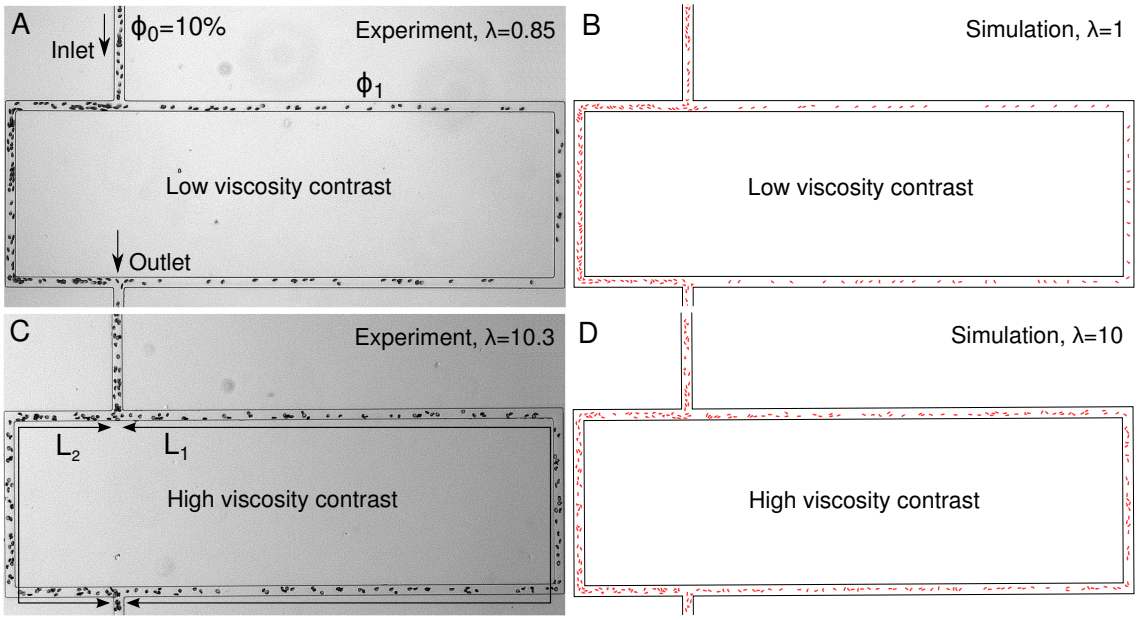

Figure 5.1: Snapshots of the RBCs partition, in both experiments and simulations, when the hematocrit of the feeding flow is around ϕ_0 =10%. The length ratio between the two child branches is set to 3. A, B: Low viscosity contrast (experiments with λ=0.85 and simulation with λ=1). C, D: High viscosity contrast (experiments with λ=10.3 and simulation with λ=10).

As we shall compare predictions for 3D hematocrit in a cylindrical tube with either 2D simulations or experiments in a rectangular channel, we should avoid any direct quantitative comparisons, but rather use Pries *et al.* predictions as a guideline to identify where new behavior is exhibited. For comparison with simulations, we set $a = W$, where W is the channel width, and we shall consider only the hematocrit ratios. For the experiments in rectangular channels, we set a to adjust the cross-sectional areas: $\pi a^2/4 = Wh$.

We analyze in details how RBC deformability affects the hematocrit partition at the bifurcations. Figure 5.1 illustrates the Zweifach-Fung effect, observed in both experiments and simulations, at a feeding area hematocrit of 10%. In both cases, less RBCs enter the low flow rate branch (the long branch) simply due to the flow rates differences between the two child branches. However, the asymmetry is significantly pronounced at low viscosity contrast λ (when the suspending fluid is more viscous than the hemoglobin). To quantify the partition asymmetry, we measure the relative hematocrit ϕ_1/ϕ_0 (or, equivalently, H_1/H_0), in the low flow rate branch, while we vary the hematocrit in the parent branch (Figure 5.2). Either in the simulations

(Figure 5.2A) or in the experiments (Figure 5.2B), we see less RBCs in the low flow rate branch than in the parent one ($\phi_1/\phi_0 < 1$), when the inlet hematocrits (ϕ_0 or H_0) lies between 5% and 45%, which is precisely a manifestation of the Zweifach-Fung effect. When the viscosity contrast is low, we observe a significantly strong reduction of hematocrit in the low flow rate branch, both in experiments and simulations, at moderate inlet hematocrit. This interesting observation suggests that the RBCs mechanical properties can strongly impact the hematocrit partition *in-vivo* since the normal hematocrit is usually less than 20% (typically between 10 and 20 % [Fung, 2013]) in microcirculation.

However, when the hematocrit is high enough, the viscosity contrast plays a minor role. This is clear in simulations (for ϕ_0 larger than 25%, Figure 5.2). Similarly, in the experiments, above $H_0 = 20\%$, data for both λ converge to the Pries *et al.* prediction. The insensitivity to the viscosity contrast beyond a critical hematocrit ($\phi_0 \simeq 25\%$) is a robust phenomenon that is independent of the length ratio between the branches (i.e. roughly the bulk flow rate ratio), as illustrated on Figure 5.3).

It is appealing to suggest that the dependency of the hematocrit partition upon the feeding hematocrit is the result of the up-stream organisation of RBCs in the parent vessel due to hydrodynamic interactions. At low hematocrit flows, the cell-cell interaction is weak and the organisation of RBCs, within the vessel, depends mainly on the dynamics of each RBCs, thus on λ. The RBCs aggregate at the center of the vessel due to the wall-induced lift force, that increases with decreasing λ and increasing RBCs deformability [Grandchamp et al., 2013]. This means that suspensions of RBCs with high viscosity contrasts have wider distributions (smaller CFL) in the channel as compared to suspensions having lower viscosity contrast. As a consequence, the asymmetry in the partition is expected to increase when the viscosity contrast decreases, as shown in Figure 5.3. To support this argument, the CFL thickness in the parent vessel and the configuration of RBCs before the bifurcation are reported in Figure 5.4 A, B. We can clearly see that RBCs distribution at high viscosity contrast (λ=10 in simulations and λ=10.3 in experiments) is wider than that at low viscosity contrast (λ=1 in simulations and λ=0.85 in experiments) when the feeding hematocrit is low (ϕ_0 <20%, see also Figure 5.4 C-I, II).

However, when the hematocrit increases, the contribution of the hydrodynamic interactions among RBCs becomes stronger and stronger. This causes a broadening of the distribution that acts against the lift force. Consequently, the partition between the two branches becomes more symmetric (that is ϕ_1/ϕ_0 becomes close to 1). Interestingly, those broad distributions are quasi independent of the viscosity contrast (see Figure 5.4 A and C-III, IV). Consequently, ϕ_1/ϕ_0 does not depend on λ either (see Figure 5.3).

Thus the distribution is independent of the strength of the interactions between cells and between cells and walls, but it is mainly caused by geometrical constraints. In other words, interaction between cells and the lift forces both depend on λ, and

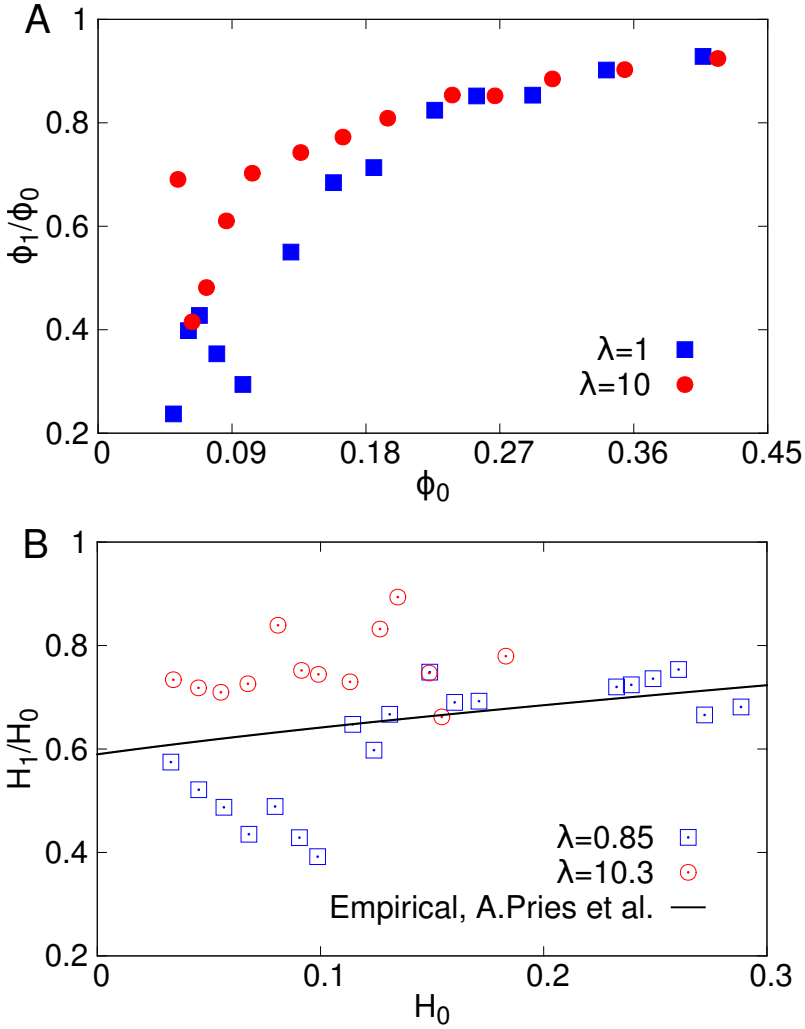

Figure 5.2: The relative hematocrit in the low flow rate branch as a function of the hematocrit in the parent vessel. The length ratio between the branches L_1/L_2 is set to 3. A: Simulations with λ=1 and λ=10. B: Comparison between experiments (λ=0.85 and λ=10.3) and the empirical law of Pries *et al.* [Pries et al., 1990] (solid line), for the same cross-sectional area. The non-monotonous evolution of the relative hematocrit at low H_0 and high λ is related to the inversion of the Zweifach-Fung effect, on which we comment later on (see Figure 5.7).

this result indicates that they depend more or less on λ in the same way. The λ contributions cancel out once a critical feeding hematocrit is reached. Noteworthy, beyond this critical hematocrit the separating ratio ϕ_1/ϕ_0 quasi plateaus which enforces the idea that in this regime, the feeding flow can be considered as a three-

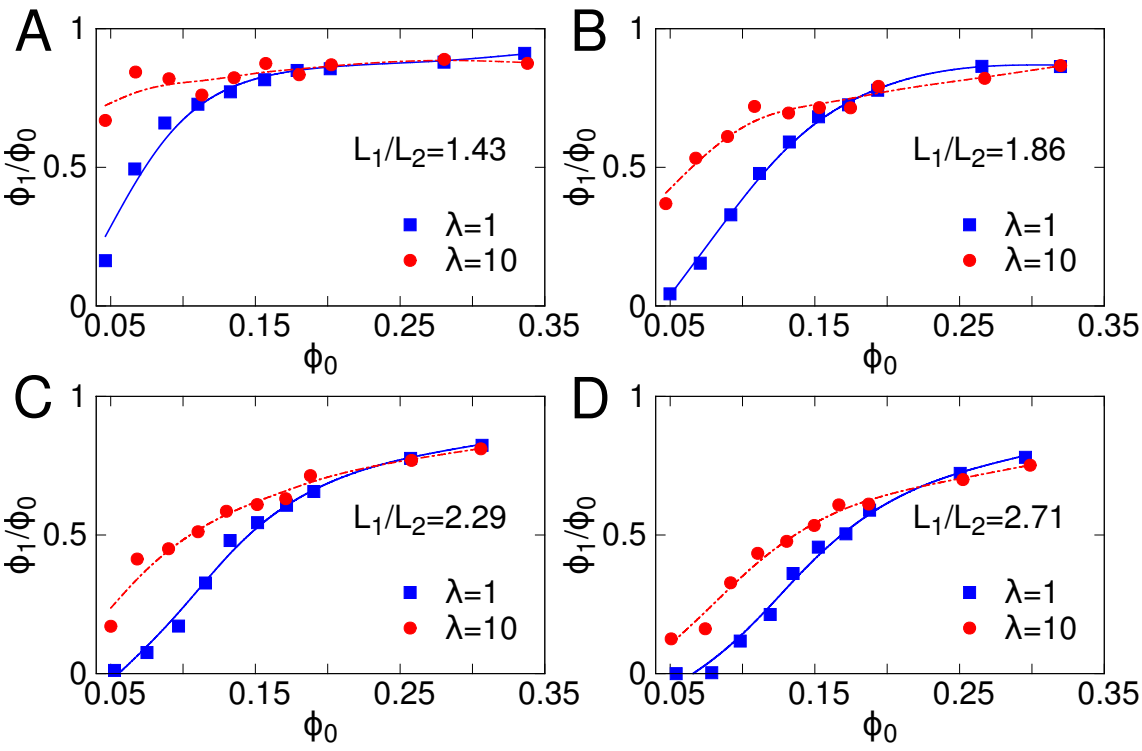

Figure 5.3: Simulations: the relative hematocrit in low flow rate branch ϕ_1/ϕ_0 as a function of the hematocrit in the parent vessel ϕ_0, for several branches length ratios L_1/L_2 and viscosity contrasts λ. At low enough ϕ_0, the asymmetry between the two daughter branches is strongly enhanced as the viscosity contrast λ is decreased, while the partitioning becomes independent on λ for hematocrit above 20%.

layer fluid (fluid-cell-fluid). The width of each layer will depend neither on the strength of interaction (which is related to deformability) nor on the volume fraction.

5.4 Inversion of the Zweifach-Fung effect

Now we focus on the low hematocrit case, for which the partition depends strongly on the detail of the interactions and on the volume fraction. Moreover a peculiar effect arises due to the prevalence of the discrete nature of blood at that scale. For all hematocrits, the distribution of RBCs is not homogeneous, but rather exhibits two lateral peaks (Figure 5.4). This become more pronounced at low hematocrit ($\phi_0 \lesssim 5\%$), where a two-file distribution of RBCs is observed, as shown in Figure 5.5. For λ=10, there is almost no cell flowing in the central part of the vessel, even though the wall-lift force tends to center them. The structure adopted by the suspension

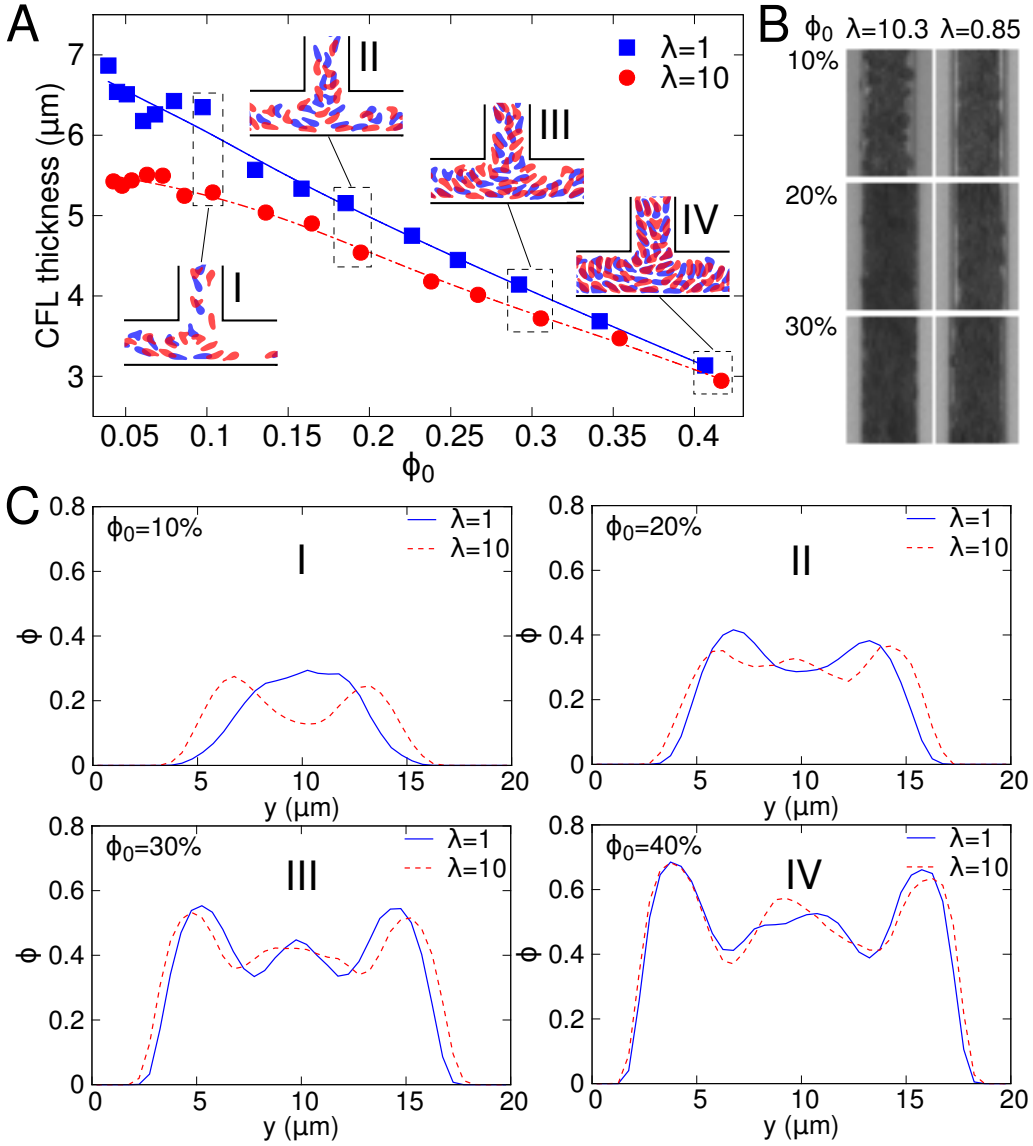

Figure 5.4: A: CFL thickness as a function of the hematocrit in the parent vessel, for λ=1 and λ=10, in simulations. Insets : Snapshots showing the suspension at the bifurcation. We define the CFL as a layer where the integrated concentration profile is below 5% [Kumar et al., 2014]. B: Snapshots from experiments, for λ=0.85 and 10.3, and hematocrit ϕ_0 =10, 20 and 30%. Every snapshot is a superimposition of 10 successive images in order to highlight the CFL in the parent vessel. C: The stationary volume fraction density functions in the parent vessel obtained from simulations.

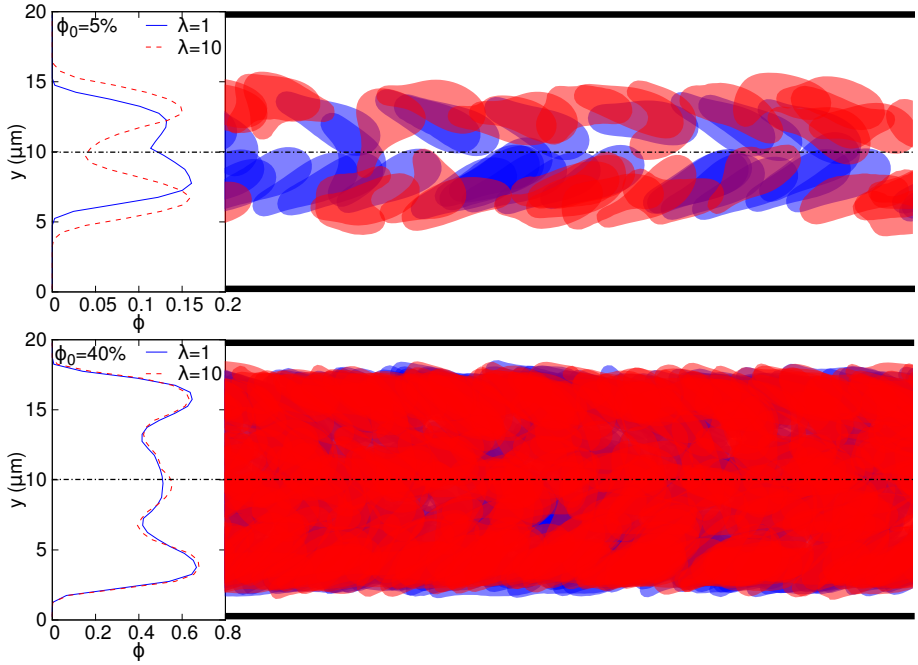

Figure 5.5: The profiles of the hematocrit distribution and the corresponding snapshots of RBCs distribution in the parent vessel. The feeding hematocrits are 5% and 40%, for two different values of λ.

can be viewed as a juxtaposition of layers with high and low hematocrits. For example, as shown in Figure 5.5 (top panel with $\lambda = 10$) the central part is depleted in RBCs, but it is escorted by two enriched layers, which themselves are surrounded by two depleted layers at the periphery (close to the channel walls). This 5-layer configuration (fluid-cell-fluid-cell-fluid) has an extremely interesting impact on the partition. This can be highlighted by measuring ϕ_1/ϕ_0 as a function of the bulk flow rate ratio Q_1/Q_0 between a child branch and the parent vessel, for fixed ϕ_0 (Figure 5.6).

If we focus first on the results for high ϕ_0 ($\phi_0 \simeq 40\%$), we find again the insensitivity to λ. As Q_1/Q_0 is increased from 0 to 0.5, the low flow rate branch 1 recruits first the CFL and then the cells. This implies that ϕ_1 starts at 0 and increases until reaching ϕ_0 when the situation is symmetric ($Q_1 = Q_2 = Q_0/2$). Our results agree with a previous 2D simulation obtained for $\phi_0 \simeq 32\%$ [Yin et al., 2013] as well as with the empirical law of Pries and coworkers [Pries et al., 1990].

An unexpected phenomenon is observed at low enough hematocrit, for $\phi_0 = 5\%$ and at high viscosity contrast $\lambda = 10$, in contrast to the high hematocrit regime (see Figure 5.6 B, $\lambda = 10$). At low Q_1/Q_0, the peripheral CFL in the parent vessel is

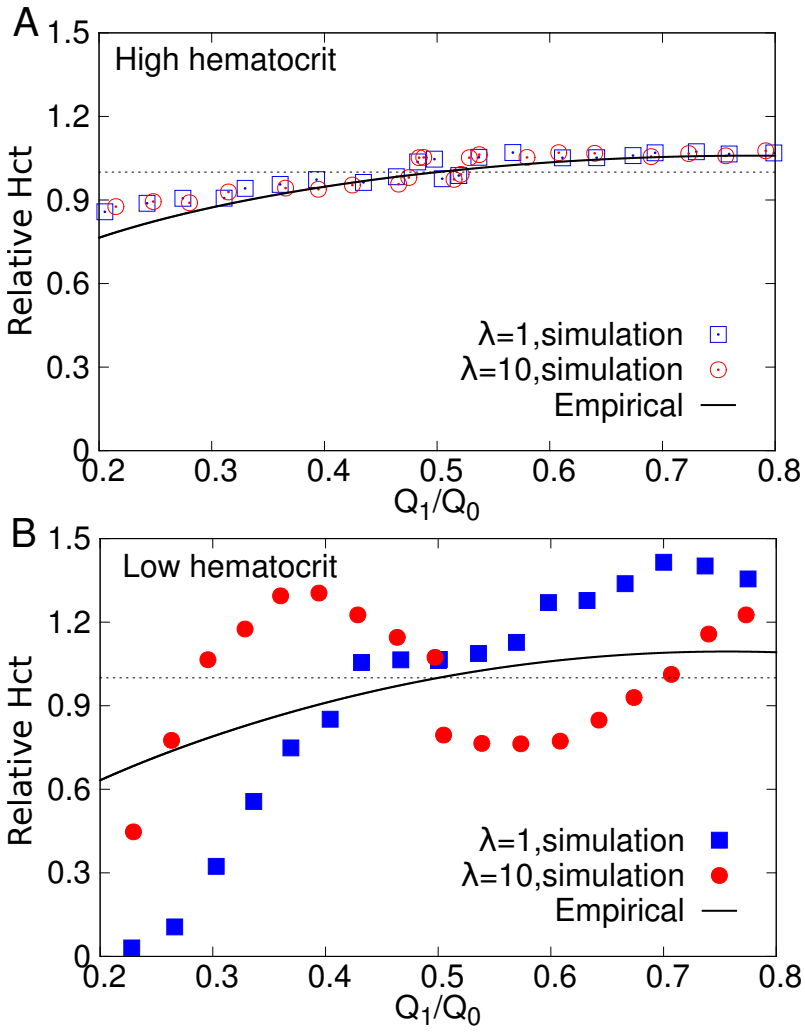

Figure 5.6: The relative hematocrit in one child branch as a function of the bulk flow ratio. Solid lines correspond to the empirical law proposed in ref [Pries et al., 1990], for $a = W$. For simulations, the relative hematocrit is ϕ_1/ϕ_0. For Pries law, it is given by H_1/H_0. A: high hematocrit ($\phi_0 = H_0 = 40\%$). B: low hematocrit ($\phi_0 = H_0 = 5\%$).

recruited by the branch 1 so ϕ_1 starts at 0 and increases when Q_1 increases. Around $Q_1/Q_0 = 0.3$, ϕ_1 becomes larger than ϕ_0. This means the hematocrit is increased in the low flow rate branch, which is the reverse behavior of the Zweifach-Fung effect. The five-layer structure mentioned above is the key ingredient for understanding this unexpected behavior: In the intermediate range $0.3 < Q_1/Q_0 < 0.5$, the low flow rate branch recruits the lateral CFL layer plus the adjacent RBC-rich layer

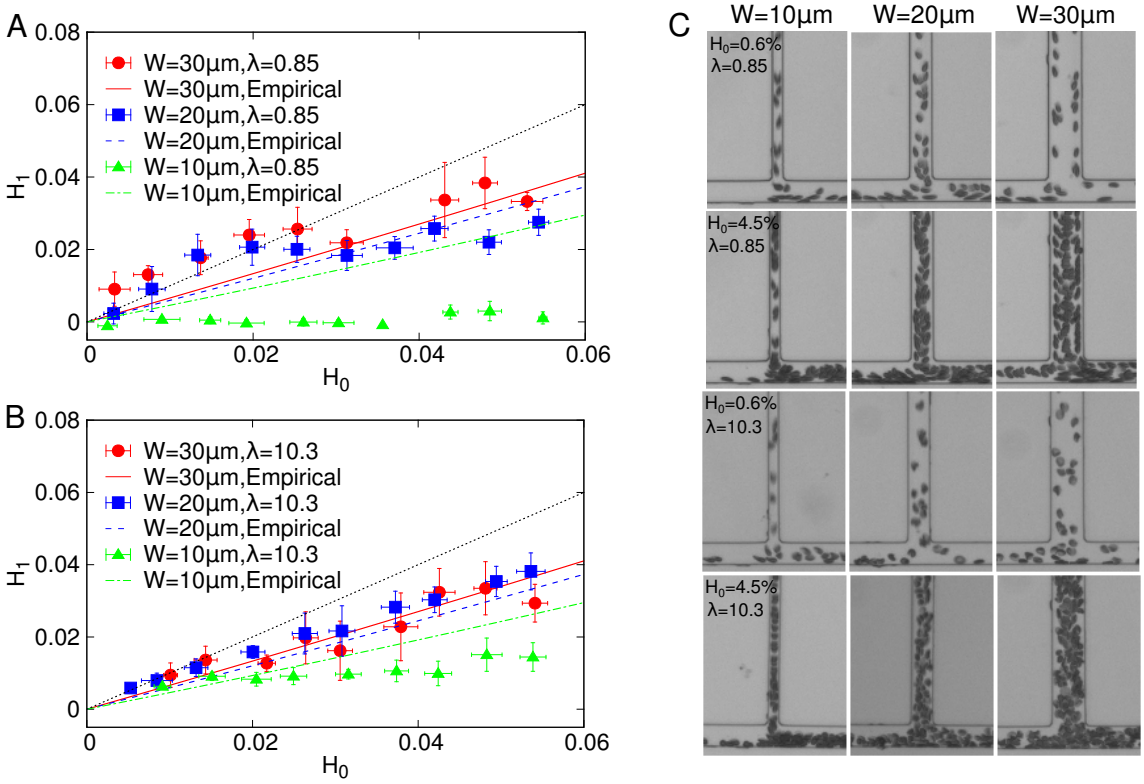

Figure 5.7: Experiments: the hematocrit in the low flow rate branch H_1 as a function of the hematocrit in the parent vessel H_0. A: Low λ ; B: High λ. The length ratio between the branches is set to 3. The width W of the inlet channel is set to 10, 20 and 30 μm. The corresponding empirical laws of Pries *et al.*[Pries et al., 1990] are also shown. The dotted line (the one with highest slope) corresponds to equal partition ($H_1 = H_0$). For $W = 20$ μm, the data are the continuation of the data already reported in Figure 5.2. C: Snapshots for each width W and two concentrations $H_0 = 0.6\%$ and 4.5%. Every snapshot is the superimposition of 10 successive images in order to highlight the structure of the suspension in the parent vessel

among the five layers. By contrast, the high flow rate branch recruits the CFL layer close to the opposite wall plus its adjacent RBC-rich layer (exactly as the low flow rate branch) as well as the central (and depleted) layer. Thus, while both branches recruit approximately the same amount of cells per unit time, those are more dilute in the high flow rate branch, which receives more fluid, while in the classical Zweifach-Fung effect, the high flow rate branch is the one that receives more cells. For $\lambda = 1$ (see Figure 5.6 B with $\lambda = 1$), the two-peak structure is not as marked as in the case of $\lambda = 10$, so the reverse Zweifach-Fung effect is not as

strong. The subtle role played by the suspension structuring at low hematocrit is also supported by our experiments, where the interplay between the diffusion and the wall-lift force is controlled by varying the width W of the inlet channel (see Figure 5.7). When W is low ($W = 10$ μm), the hematocrit in the low flow rate branch is much lower than expected from Pries *et al.* predictions (which were not validated on this confinement range). This is caused by the CFL effect that becomes very strong. As in the simulations, for $Q_1/Q_0 = 0.25$, this effect is more pronounced at low λ, that corresponds to a more important wall lift force. The 5-layer structure is clearly observed also in the experiments for $H_0 < 5\%$, $W = 20$ or 30 μm and at low λ (Figure 5.7 C), but not at high λ, while it was more strongly marked at high λ in the simulations. This indicates that this peculiar structure is very dependent on the mechanical properties of the cells and also on the degree of confinement. Nevertheless, a robust feature is valid in both simulations and experiments: When the two-file structure of RBCs takes place, a clear inversion of the blood partition at the bifurcation is observed. In the experiments, this corresponds to Figure 5.7 A, where some points lie above the equal partition line when $H_0 < 2\%$.

There are also situations in which one of the two branches can be even completely devoid of RBCs (Figure 5.7 C). A corresponding prolonged lack of RBCs perfusion to real blood vessels causes dysfunction and possibly ischemia disease. Because RBC mechanical properties are affected by aging and pathologies, these can induce abnormal partitions of the hematocrit in the vascular network.

Chapter 6

Deformability-influenced delivery of red blood cells in microvascular networks

In this chapter, we present our preliminary simulations regarding the properties of RBC flow in networks. Section 6.1 provides a general introduction about motivation and Section 6.2 will define the system under consideration. In Section 6.3, we report on deformability-induced lateral displacement of RBCs in the network. In Section 6.4, we present a somewhat unexpected result in that the flux of rigid RBCs is higher than that of soft RBCs, in contrast to the flow in a straight channel. Finally, diffusion of RBC clouds in the network and its far-reaching consequences are the subject of Section 6.5.

6.1 Introduction

In vivo, blood flows through a complex network of the microcirculatory system in order to ensure oxygen delivery and remove metabolic waste. Understanding blood flow in microvascular networks and its dependence on the mechanical properties of its constituents are essential to understand some physiological implication in microcirculation. A prominent example is ischemia disease which is often associated with congested blood flow. Indeed, within many patients with even a healthy coronary artery, an improper hematocrit distribution is observed in the heart microcirculation, such as occlusion zones. These abnormal traffic zones cause a lack of oxygen supply to tissues, leading to cardiac ischemia disease, the origin of which is largely not yet elucidated. For example, does the topology of the vascular network have a direct influence on the hematocrit partition, and thus on perfusion properties? Besides helping understand the influence of blood flow on physiology and pathology in

microcirculation, this study may open some applications in biomedical technology and chemical engineering, such as the design of appropriate networks for cell sorting and the conception of tailored microparticles for a targeted drug delivery.

Several factors govern the behavior of RBCs during flow, as we have seen throughout this thesis. For example, we have seen that the deformability of RBCs can have major consequences on lateral migration and thus on hematocrit partition. This migration is a result of the wall induced lift force due to hydrodynamic interactions [Callens et al., 2008; Cantat and Misbah, 1999b; Grandchamp et al., 2013], that depends on the nature of RBC dynamics (like tank-treading or tumbling) [Abkarian et al., 2007; Dupire et al., 2012]. Other factors enter into play in this phenomenon: (i) The curved velocity profile of the Poiseuille flow [Coupier et al., 2008b; Farutin and Misbah, 2014; Katanov et al., 2015; Shi et al., 2012], and (ii) The cell-cell hydrodynamic interactions [Grandchamp et al., 2013; Hariprasad and Secomb, 2014; Katanov et al., 2015; Krüger et al., 2014; McWhirter et al., 2009]. The migration makes RBCs aggregate in the center of the vessel forming a cell depletion layer between the wall and RBC rich region, resulting in a mean velocity of RBCs larger than the mean velocity of the plasma. This leads to the famous Fåhræus effect [Barbee and Cokelet, 1971; Pries et al., 1992], the hematocrit in the tube is smaller than the hematocrit in the reservoir. As the consequence of the Fåhræus effect and the cell depletion layer, the apparent viscosity of blood decreases with decreasing vessel diameter, which is known as the Fåhræus-Lindqvist effect [Pries et al., 1990, 1992], as we have seen earlier.

We have seen in the previous chapter that the depletion layer plays a major role in the partition of RBCs at bifurcations, which is described by the Zweifach-Fung effect [Dellimore et al., 1983; Fenton et al., 1985; Guibert et al., 2010; Pries et al., 1989]: the feeding flow is divided by a separating streamline into two parts, one feeding the low flow rate branch and the other feeding the high flow rate branch. Due to the cell free layer, the RBC fraction entering the low flow rate branch is smaller compared to the original RBC fraction in the total feeding flow, while the other branch, that having higher flow rate is enriched. When the flow rate is sufficiently small in the child branch, the hematocrit in this branch can even drop down to zero, while it reaches high values in the other branch.

Obviously, these above effects have physiological consequences as they alter the rheology of blood and distribution of RBCs and consequently alter the transport of oxygen and other essential metabolites, and may even trigger pathological disorders. Combining the above effects, Pries et al. proposed an empirical model [Pries et al., 1990], which can be used to predict the hematocrit distribution in a network by giving information of the vascular structure and by choosing appropriate boundary conditions. This model is based on the assumption that the flow in the vessel is well developed. However, in real situations, the vascular network consists of many short vessel segments with length of about hundreds micrometers [Popel and Johnson,

2005], which are not long enough to sufficiently allow development of the blood flow, especially in the dilute case. The corpuscular nature of the RBC distribution together with the fact that the flow is not always fully developed in short enough vessels make the problem quite challenging and large deviations can be manifested as compared to the classically adopted picture. We have presented in the last chapter an example where the partition of hematocrit can be inverse to that predicted by continuum models of suspension [Shen et al., 2016]. This points to the fact that simulations taking explicitly the corpuscular nature of blood, is the only present alternative for a firm understanding of blood flow properties.

To better understand the blood flow properties in the microcirculation, direct numerical simulations of RBC suspensions in a 2D network are carried out here. As a first step we consider the network to be ordered, a choice dictated by reducing complexity in order to clarify the sole effect of the branching. A structured network with hexagonal loops is used to make a symmetrical flow at each bifurcation. We examine the effect of the multistage bifurcation. The motion of single RBC in the network is firstly investigated. We shall see that the configurations (such as lateral migration in the channel) of RBC in the downstream position depend on the previous states of RBC in the upstream position (the phenomenon is history-dependent). This results in a quite rich behavior when the RBC meets a bifurcation. For example, a chaotic partition of RBC may take place at bifurcations, and this clearly has an impact on the overall displacement of RBCs in the network. We find that the deformability of RBCs impacts the displacement for low concentrations, up to about 20%, beyond which the crowding effects and cell-cell interactions make no big distinctions among different RBC deformabilities. Since the hematocrit in the microvasculature lies in the range of $5 - 20\%$, the observed phenomena which we will report below are clearly of important relevance in microcirculation.

Besides the above effects, we discover that RBCs exhibit larger flux in the network when they are more rigid and this is in a marked contrast with the scenario in straight tubes. Finally, and probably this is the source of the latter phenomenon, we will see that cells enjoy a faster longitudinal diffusion when they have a smaller deformability.

6.2 Methods and parameters

As before, we use LBM as the NSEs solver (see Section 2.2). We recall that the RBC is modeled as a 2D vesicle by using a spring network with bending elasticity (see Section 2.5). The coupling of membrane and fluid is implemented by the IBM (see Section 2.4).

The geometry of the network has a honeycomb structure (in Figure 6.6). The half-way bounce-back boundary condition (see Section 2.2) is used for the non-slip

condition at the fluid-solid interface. We fix the channel width W at $4R$ ($10\mu m$), recall that R is the radius of RBC. Each vessel segment has a length of $40R$ ($100\mu m$).

Periodic boundary is applied in both X and Y directions. The size of the computational domain is chosen much larger than the size of RBC, so that the influence from periodic boundary conditions can safely be ignored. The length of domain in the Y direction is taken to be $146.6R$, containing two hexagonal loops. Two different domain lengths in the X direction are used in this work. One is equal to $127R$, used for studying lateral displacement of the RBCs in suspension. The other one equals $507.8R$, which is large enough to provide a sufficient space for observing the longitudinal diffusion of RBCs.

A constant body force is applied to drive the fluid, which is equivalent to a pressure-driven flow. By adopting different values of the bending modulus k_b and viscosity contrast $\lambda = \eta_{int}/\eta_{ext}$, we can vary the deformabilities of RBC which affects the behaviors of RBC at bifurcation. The bending elasticity is involved in the capillary number, defined as $C_a = \eta_{ext}R^3\dot{\gamma}/(4k_bl_0)$, here $\dot{\gamma}$ is the mean shear rate calculated by $\dot{\gamma} = U_m/W$, U_m is the maximum velocity of the flow in the absence of RBCs. η_{ext} and η_{int} are the viscosity of external solution and internal fluid enclosed by the RBC membrane.

The initial positions of RBCs are randomly distributed with different concentrations in the whole network when we are interested in the lateral displacements. When we focus on the longitudinal diffusion, the RBCs are concentrated in one fourth of the network to produce a high initial local hematocrit of 28%.

6.3 Lateral displacement of RBCs

6.3.1 Behavior of a single RBC

We will here pay attention to the behavior of a single RBC in the network. Prior to this study we first consider the behavior of a solid spherical particle, which will serve as a reference study. Once the particle enters a given branch at a bifurcation, for example the lower one, it will stay close to the upper wall when it converges into the feeding vessel in the next stage. Since it does not experience any lift force (recall that a rigid spherical particle can not lift-off due to the reversibility of the Stokes equations upon time reversal), once it reaches the next bifurcation it enters the upper branch, afterwards it stays close to the lower wall, enters the lower branch, and so on. In a summary, the particle shows a zigzag-like trajectory without global lateral displacement in the network.

Let us now consider a RBC in the network. On the one hand, the shape of RBC evolves in the course of its flow in a branch. Because of its shape evolution the RBC will experience a lift force which tends to push it towards the center. However,

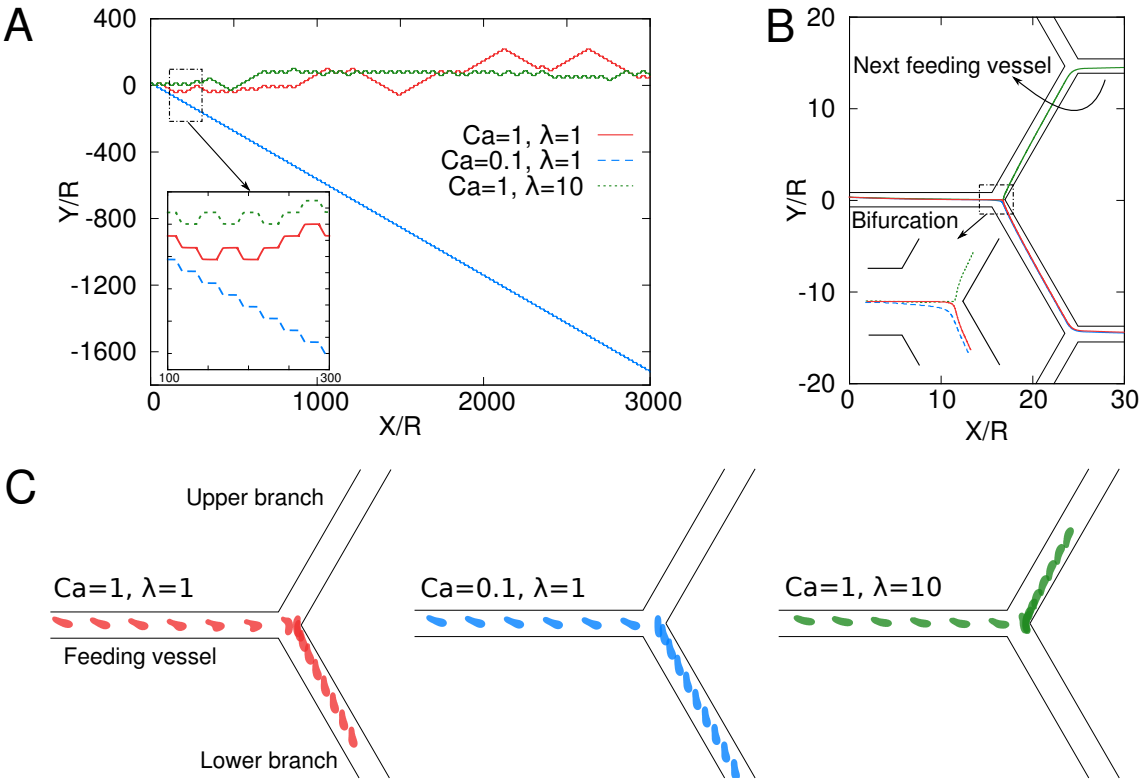

Figure 6.1: Single RBC flows in the network. The red solid line is for the case of $C_a = 1$, $\lambda = 1$, the blue dashed line is for the case of $C_a = 0.1$, $\lambda = 1$ and the green dotted line is for the case of $C_a = 1$, $\lambda = 10$. C_a is the capillary number for membrane bending elasticity. λ is the viscosity contrast. A: The trajectories of RBC mass center in the network. The case of $C_a = 0.1$, $\lambda = 1$ shows a deterministic displacement, while the other two cases show an erratic displacement. B: The trajectories of RBC mass center at one bifurcation within the network. C: The evolution of RBC shape and position at one bifurcation within the network.

if the branch is not long enough the RBC might not have sufficient time to reach the center. In addition, at the bifurcation, because of the deformation of RBCs the choice between the upper and lower branch might be complex since its shape might be quite different from one bifurcation to the next. We thus expect quite rich behaviors. Taking the rigid particle case as a reference, we might be tempted to think that a RBC having a large bending rigidity (and thus not too deformable), may follow the same trend as the rigid particle. Actually, this reasoning fails to predict the real behavior in this case. For example, we find that the behavior of a RBC having a stronger bending rigidity deviates significantly from the behavior

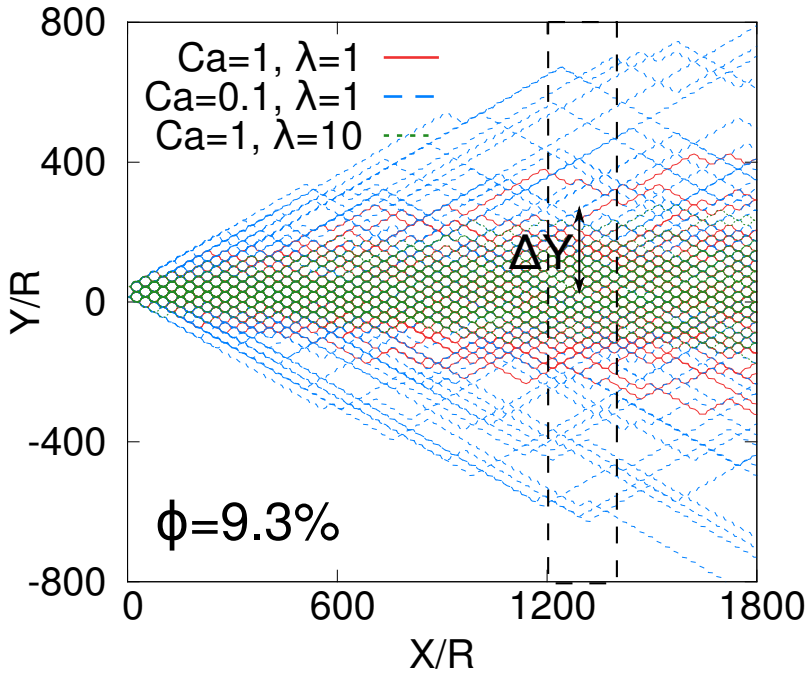

Figure 6.2: The trajectories of all the RBCs for different C_a and λ in the case of low hematocrit (9.3%). The dashed line box identifies the regime used for the average of ΔY in Figure 6.4. The ΔY is the lateral displacement of RBCs from the initial positions.

of a rigid particle, while a softer RBC has a closer behavior as the rigid particle. This counter-intuitive behavior highlights the complexity of the problem. Figure 6.1 presents the trajectories of RBC mass centers for high (blue dashed line, $C_a = 0.1$) and low (red line, $C_a = 1$) membrane rigidity. The understanding of this behavior is subtle. While the particle has a high enough rigidity, its orientation tank-treading angle remains quite constant (Figure 6.1 C bottom, middle) and when it approaches the bifurcation, the orientation is towards the lower branch. Thus the head of RBC is firstly pulled by the lower branch. The trajectory given in the Figure 6.1 B shows that the mass center of the rigid RBC has crossed the centerline into the downward stream regime before it meets the corner. When it impacts the bifurcation solid boundary it rotates in a quite rigid manner (due to its high rigidity) and enters the lower branch, making the RBC stay close to the upper wall in the next feeding vessel, where the RBC finds itself in the same configuration as in the previous feeding vessel, and so on. Overall, the cell will drift indefinitely sideways (either in the lower part or the upper part of the network, depending on initial condition. In Figure 6.1, we have a downward drift. We can refer to this case as a long memory behavior.

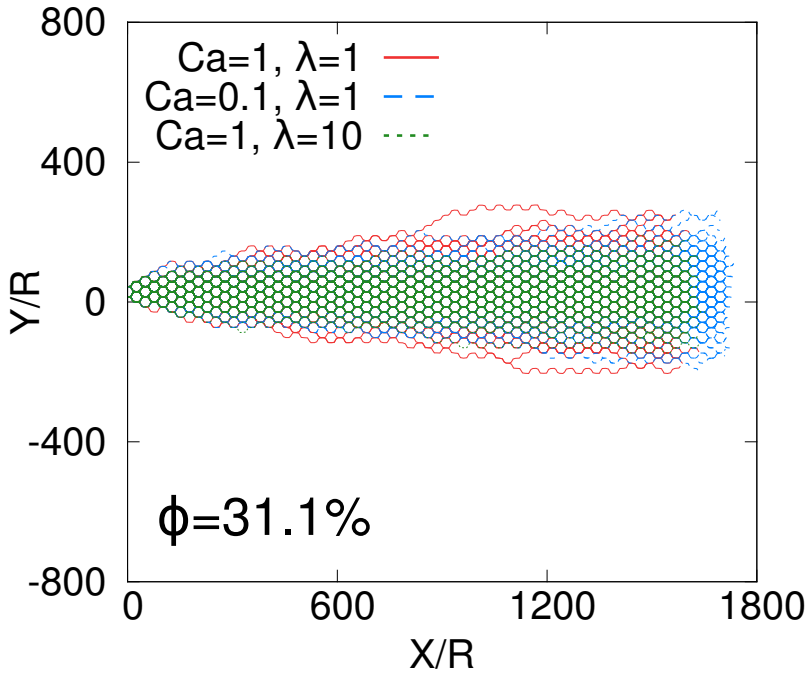

Figure 6.3: The trajectories of all the RBCs for different C_a and λ in the case of high hematocrit (31.1%).

Let us now consider the case of a softer RBC (say $C_a = 1$), red line in Figure 6.1). The cell experiences a lift force, and due to its softness, it assumes a parachute-like shape (in contrast to the previous case with a more rigid cell), but not fully symmetric, before it reaches the bifurcation. Since the RBC is soft it deforms so much during the flow in the vessel so that it will have often quite different shapes from one bifurcation to the next. Due to these rather quite uncontrolled shapes at successive bifurcations (actually at any new branching everything happens as if the initial condition is different, so that at the next bifurcation the shape is likely to be different from the previous one.), one thus expects that the RBC will undergo a zig-zag motion in the network. Due to the shape variability at bifurcations, we can call this case as a short memory behavior.

Finally, another parameter plays an essential role as well: the viscosity contrast λ which acts on the ability of the cell to deform. We investigated the case with $C_a = 1$, but with $\lambda = 10$; in other words, rigidity is now monitored by a more viscous internal fluid. In this case, there is a weaker lift force due to the relatively smaller orientation angle. The cell has not enough time to reach the center (in contrast to the case of $C_a = 1$ and $\lambda = 1$), and in addition, its orientation angle points less towards the lower branch. This results in a zig-zag motion of the cell in

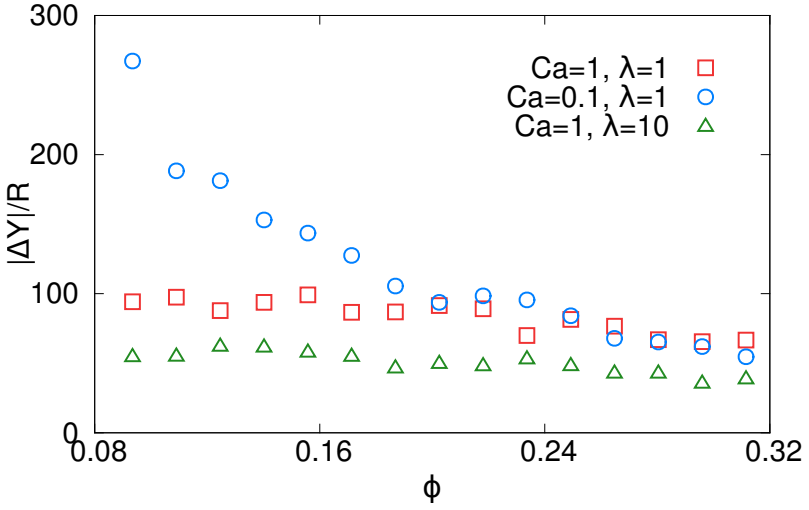

Figure 6.4: The averaged absolute lateral displacement of RBCs in the dash box shown in Figure 6.2 as a function of the hematocrit for different C_a and λ.

this case.

6.3.2 Behavior of a suspension

The study of a single cell may give some hints towards the behavior of a suspension, especially in the dilute enough regime. We have seen above that the membrane rigidity induces different behaviors for a single cell: a rigid cell drifts sideways, while a softer cell undergoes a zig-zag motion. A quite viscous internal fluid show the same trend as the soft RBC (zig-zag motion). We have thus simulated a suspension in a regime where the concentration is not too high, but still consistent with the values encountered in microcirculation. Figure 6.2 shows the result in the network for a concentration of 9.3%. We find interesting results in that the RBCs with high membrane rigidity have the largest lateral displacement while the RBCs with high viscosity contrast have the smallest lateral displacement. While for a single cell with high enough rigidity we had found a sideways drift, the presence of occasional interaction with other cells, initial configuration at the bifurcation might vary, so that the cells can drift both upward and downward in a suspension. However, still the ample lateral displacement can clearly be distinguished between the cells with strong rigidity and those with low rigidity (as well as the cells enclosing a more viscous fluid).

When the concentration becomes high enough, the frequent mutual interactions among cells cause a strong mixing in the orientations and deformation of cells, so that we expect the distinction between the different cell properties (rigidity, viscosity

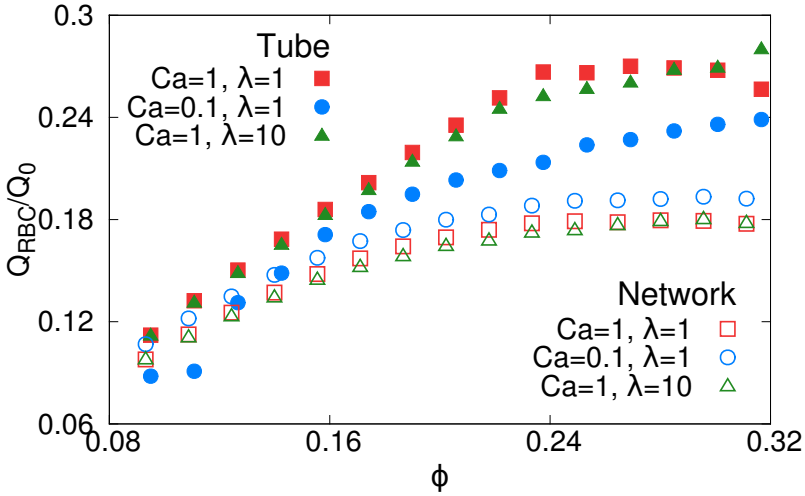

Figure 6.5: The flux of RBCs as a function of hematocrit for different C_a and λ. The solid points present the results for RBCs flowing in the tube. The hollow points present the results for RBCs flowing in the network.

contrast) to weaken as concentration increases. Interestingly enough, we find the distinction is still quite visible as long as the concentration is not too close to 20%, which is the normal situation in microcirculation. When the concentration becomes larger, a quite minor distinction can be detected, as shown in Figure 6.3 where the trajectories of RBCs are plotted for a hematocrit of 31.1%.

Figure 6.4 shows the averaged absolute lateral displacement of RBCs (as defined in Figure 6.2) as a function of the hematocrit. We see that there is a critical value of about 20%, above which the membrane rigidity does not play a role in the lateral displacement of the RBCs. We note that the lateral displacement is independent on the hematocrit either for low viscosity contrast or for high viscosity contrast when the RBCs have low membrane rigidity, while the higher viscosity contrast provides a smaller lateral displacement. Also note that for low enough hematocrit the lateral displacement can be more than 3 times larger for RBCs with high rigidity and small viscosity contrast ($C_a = 0.1$, $\lambda = 1$) than for soft cells with a more viscous fluid ($C_a = 1$, $\lambda = 10$). These findings are not devoid of experimental testability.

6.4 Flux of RBCs

Another important point of the RBC transport is the RBC flux which represents the capacity of RBC to deliver oxygen per unit time in vessel cross section. It is defined as the volume of RBCs passing a vessel cross section per unit time (Q_{RBC})

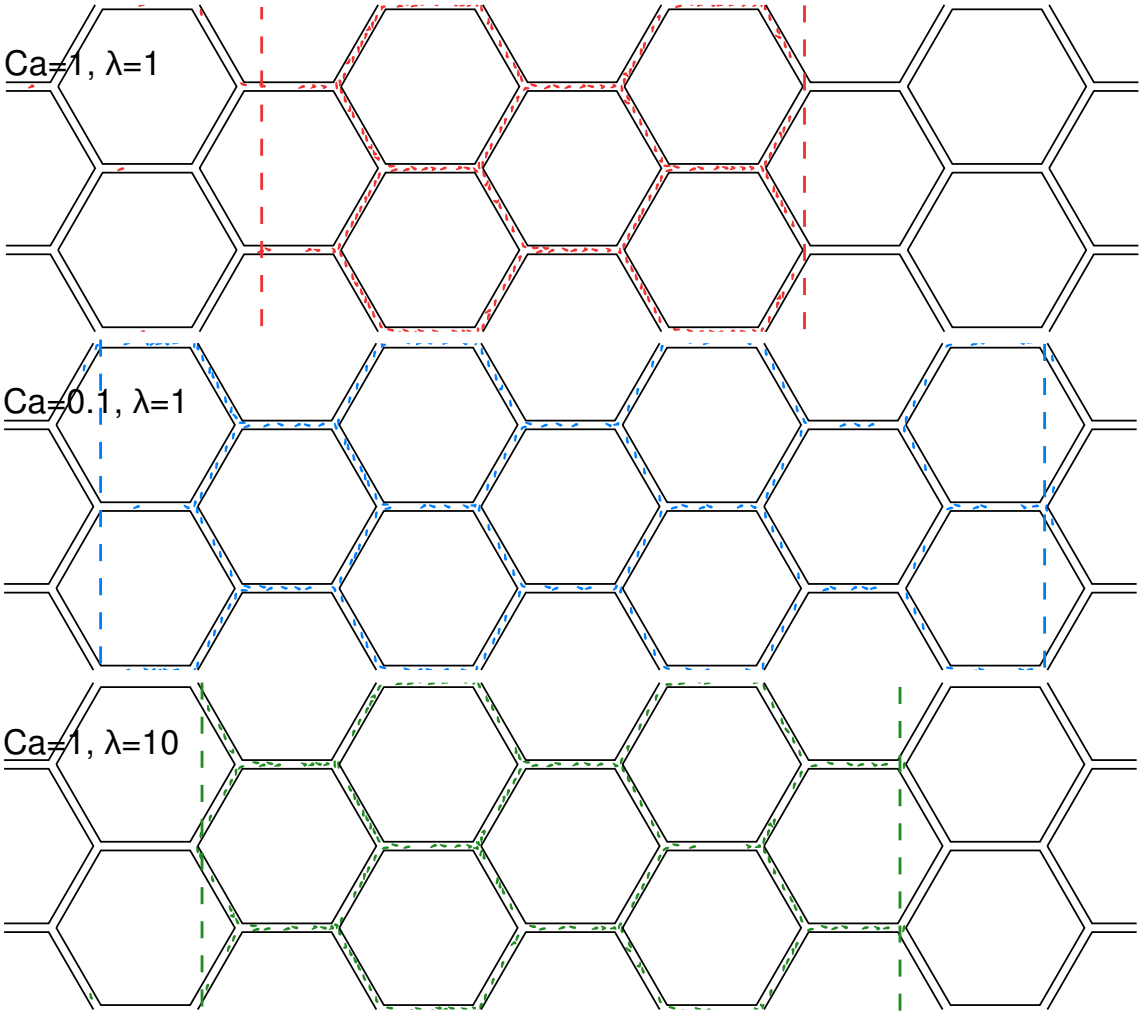

Figure 6.6: Distribution of RBCs in the network after the flow of RBCs is long time developed.

and normalized by the flow rate in the absence of cells (Q_0). A priori, we may expect that a higher hematocrit would lead to a higher flux of oxygen. However, as we know, the viscosity of the RBC suspension increases with the increasing hematocrit, which causes the bulk flow rate to decrease with hematocrit. As a consequence, when the hematocrit increases, the RBC flux firstly increases and then should reach a peak at some hematocrit, before it decreases, as shown in Figure 6.5. Furthermore, we expect the flux to be lower for more rigid cells, and this is confirmed by our simulations.

We have examined this question in a network and compared with the case of

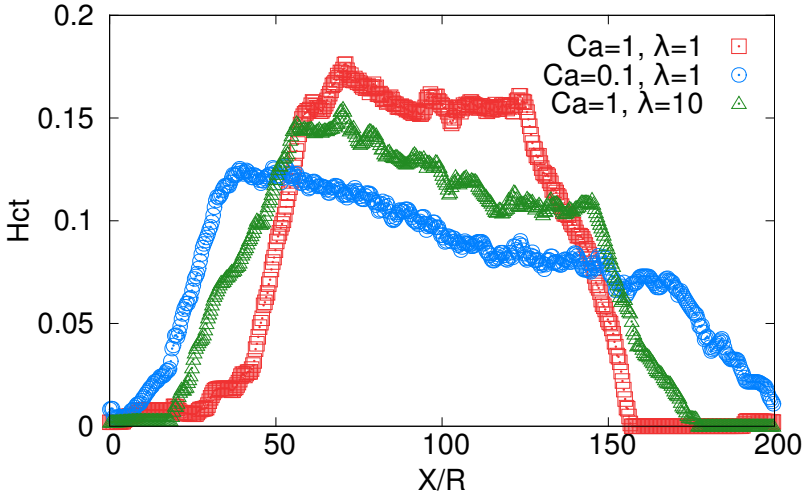

Figure 6.7: The distribution of hematocrit along the flow direction for different C_a and λ.

a straight channel. Surprisingly, we find a counter-intuitive trend in the network regarding the effect of rigidity. In tube, the RBCs with high membrane rigidity have a smaller flux as compared to softer cell (which is the expected result), while the opposite happens in the network (Figure 6.5). Cells with a higher membrane rigidity give rise to a higher viscosity of RBC suspension in tube, that leads to a smaller RBC flux. In network, the situation is quite different, and the membrane rigidity plays less role in the viscosity of suspension since the development of the flow of RBCs is always renewed by the successive bifurcation, which also explains that the RBC flux in network is smaller than the RBC flux in tube because the well developed RBCs in tube receive a higher mean velocity. The membrane rigidity plays a more significant role in the partition as we discussed before. From Figure 6.1 C, we can see that the RBC with high membrane rigidity spends less time at the corner as compared to a softer one, thus enhancing the transit of more rigid cell. This seems to be a plausible explanation for the enhancement of the flux for more rigid cells in network. The viscosity contrast has a minor effect on the RBC flux.

6.5 Longitudinal diffusion of RBCs

As the heterogeneity of RBC distribution often happens in the microcirculation, it is interesting to analyze this question, by considering the behavior of a RBC cloud when it flows in the network. The RBC suspension is taken initially highly concentrated in a quarter of the network with a hematocrit of 28%. During the

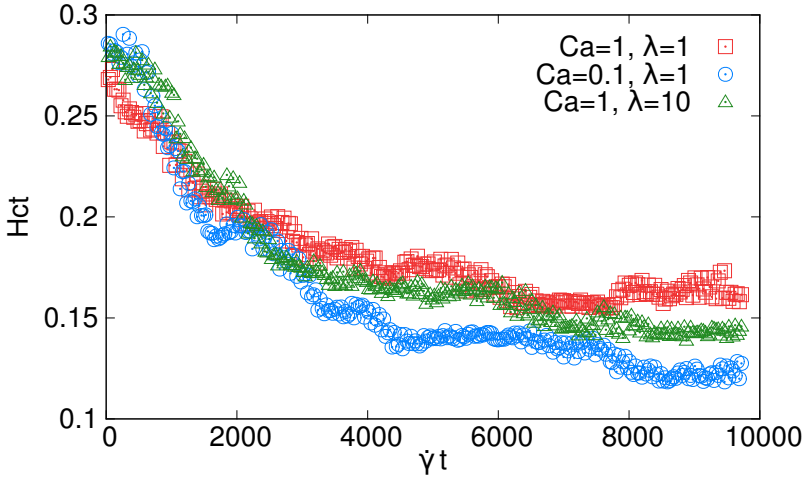

Figure 6.8: The evolution of local hematocrit for different C_a and λ. Here the local hematocrit is calculated by averaging those hematocrit larger than 90% of the maximum.

RBCs flowing, the relative distance between RBCs increases. The RBC suspension shows a diffusion-like behavior with a hematocrit dependent diffusion rate. Finally, the diffusion ceases when the local hematocrit reaches a certain value, depending on the RBC deformability. In Figure 6.6, the final configurations of RBCs distribution are presented. The RBCs with high membrane rigidity ($C_a = 0.1$) form the widest distribution while the softer RBCs with low viscosity contrast ($C_a = 1, \lambda = 1$) are the most concentrated. In Figure 6.7 we plot the hematocrit distribution along the flow direction after long time evolution. The evolution of a local hematocrit in the network is given by Figure 6.8. The results show that the high membrane rigidity ($C_a = 0.1$) sample causes the strongest diffusion (the smallest final local hematocrit and the largest diffusion rate). Comparing the two cases with different viscosity contrasts, we find that the higher viscosity ($C_a = 1, \lambda = 10$) corresponds to stronger diffusion. Also note that the diffusion rate exhibits a nonlinear behavior with hematocrit, and decreases with decreasing hematocrit.

Chapter 7

Conclusions and perspectives

In this chapter we briefly recall the main results and then present a list of questions which should constitute an interesting task for future investigations. The main topic of this thesis has focused on the collective behaviors of RBC suspensions. The main findings and some perspectives are discussed below:

7.1 Summary of Chapter 3 and Chapter 4 and related perspectives

In Chapter 3 and Chapter 4, the hydrodynamic interactions between deformable particles (a model of RBCs) are studied both in 2D and 3D by numerical simulations. The results reveal the mechanism of the self-organization of RBCs under confined linear shear flow in both 2D and 3D. A link between the spatiotemporal organization of the RBC suspension and rheology has been analyzed. The results show that the rheology of the RBC suspension is dramatically affected by the order of RBCs in the presence of confinement. Our findings are of fundamental understanding of many body system and rheology of complex fluids, focusing on the link between microdynamics of RBCs and macrorheology of blood at the global scale. These studies can also open future practical applications, such as diagnosis; for example, order depends on mechanical properties of cells, and so does rheology. Since in microfluidics a small amount of blood (microliters) is required, it is essential to conceive of appropriate architectures to measure order and rheology in miniaturized automated systems.

There are still many perspectives to be carried out in the future:

- A more systematic exploration of the parameters will be important for a deeper understanding of complex fluid behaviors under confinement. For example, how does the shear thinning and shear thickening behavior occur in relation with the organization of suspended entities?

- Regarding the reality of blood in vessel, the flow condition usually presents a pressure-driven channel flow, where the dynamics of the RBC are different from that in linear shear flow. An extended study in confined Poiseuille flow is needed for a more comprehensive understanding of blood rheology.

- Here we have examined the case of purely hydrodynamical interactions. Other factors, like plasma proteins, contribute to RBCs aggregation under physiological conditions. An extension of this work to the case including the aggregation between cells will constitute an interesting task for having a more complete description of blood flow.

- When the suspension is not homogeneous (as found in this work), the notion of an overall effective viscosity is ill-defined, since it is assumed that the shear rate is constant in the gap. Thus we have to resort to an analysis of local rheology, which is a question of primary importance for any complex fluid (confined or not) which exhibits an inhomogeneous structure of the suspended entities (like shear bands, organization of files as found in this work, etc...). It is hoped to investigate this matter in the future.

7.2 Summary of Chapter 5 and Chapter 6 and related perspectives

In Chapter 5 and Chapter 6, the partition of RBCs at the level of bifurcations is addressed by means of computer simulations and in vitro experiments. The RBC transit is investigated through simulations of a large number of RBCs flowing in a network pattern structured as a honeycomb. Our findings suggest that the deformabilities of RBC must be taken into consideration and carefully analyzed in order to have a firm understanding of the blood perfusion and the RBC transit in microcirculation. The results of our present work provide a valuable background needed to pinpoint the various RBCs properties that govern the blood perfusion, and thus oxygen delivery in the microcirculation in general. The results also have significance in the practical applications, such as cell sorting and chemical analysis.

Some perspectives of this work are outlined here:

- Since our numerical and experimental results on hematocrit partition in hemodilution contrast with the common belief, this points to the fact that existing models have to be revisited in order to capture this effect. However, it is not clear that continuum models will still adequately give the apparently prevalent nature of the discrete property of blood. Prior to that, 3D simulations should first be implemented in the future in order to seek for a more direct quantitative comparison with experiments.

- A systematic study on the influence of the network structure on the RBC distribution will be considered in the future. Firstly, it will be important to link the network topology to the perfusion nature. Secondly, medical images can be extracted in order to model the real vessel network, for a systematic simulations on real networks, and for potential practical applications.

- It will be an interesting task to implement oxygen diffusion in the present model, in order to simulate oxygen transport tissues with complex vessel networks. This should provide better background for a better understanding of the physiology and pathology of microcirculation.

Chapter 8

Des conclusions et des perspectives

Dans ce chapitre, nous rappelons brièvement les principaux résultats et puis présentons une série de questions qui devrait constituer une tâche intéressante pour des études futures. Le sujet principal de cette thèse est concentré sur les comportements collectifs des suspensions de RBC. Les principaux résultats et certaines perspectives sont discutés ci-dessous:

8.1 Résumé du chapitre 3 et du chapitre 4 and et des perspectives associées

Au chapitre 3 et Chapter 4, les interactions hydrodynamiques entre les particules déformables (un modèle de RBCs) sont étudiées en 2D et 3D par des simulations numériques. Les résultats rapportenet sur le mécanisme de l'auto-organisation des RBCs sous écoulement de cisaillement linéaire confiné en 2D et 3D. Le lien entre l'organisation spatio-temporelle de la suspension de RBC et la rhéologie a été analysée. Les résultats montrent que la rhéologie de la suspension de RBC est affectée dramatiquement par l'ordre des RBCs en présence d'écoulement. Nos résultats fournissent une compréhension fondamentale qui s'insère dans la problématique de la rhéologie des fluides complexes, en se concentrant ici essentiellement sur le lien entre la microdynamique des RBCs et la macrorhéologie du sang à l'échelle globale. Ces études peuvent également ouvrir des applications pratiques à venir, tels que le diagnostic; par exemple, l'ordre dépend des propriétés mécaniques des cellules, et cet ordre affecte la rhéologie. Comme en microfluidique une faible quantité de sang (microlitres) est nécessaire, il est essentiel de concevoir des architectures adaptées pour me surer l'ordre et la rhéologie dans les systèmes automatisés miniaturisés.

Il reste encore de nombreuses questions ouvertes, qui constituent un sujet riche

de perspectives, comme décrit ci-après.

- Une exploration plus systématique des paramètres sera très utile pour mieux comprendre les comportements des fluides complexes sous confinement. Par exemple, il serait intéressant d'étudier la rhéofluidité et le rhéoépaississement et leurs relations avec l'organisation des entités suspendues.
- In vivo l'écoulement est imposé par une différence de pression, où les dynamiques des RBC sont différentes de celles obtenues dans un écoulement de cisaillement linéaire. Une Étude complémentaire en écoulement Poiseuille confiné est nécessaire pour une meilleure compréhension de la rhéologie du sang.
- Ici nous avons examiné le cas d'interactions hydrodynamiques. D'autres facteurs, comme les protéines du plasma, contribuent à l'agrégation des RBC dans les conditions physiologiques. Une extension de ce travail prenant en compte l'agrégation entre les cellules constituera une tâche intéressante pour disposer d'une description plus complète de l'écoulement sanguin.
- Lorsque la suspension n'est pas homogène (comme démontré dans ce travail), la notion d'une viscosité effective globale est mal définie. En effet, une hypothèse sous-jacente à cette définition est que le taux de cisaillement est constant dans le gap. Si tel n'est pas le cas, il devient donc nécessaire de recourir à une analyse de la rhéologie locale, qui constitute une question d'une importance primordiale pour tout fluide complexe (confiné ou non) qui présente une structure inhomogène (comme les bandes de cisaillement, organisation en files, comme rapporté dans ce travail , etc...).

8.2 Résumé du chapitre 5 et du chapitre 6 et des perspectives associées

Au chapitre 5 et chapitre 6, la répartition des RBCs au niveau d'une bifurcation est abordée dans nos simulations sur ordinateur et par des expériences in vitro. Le transit de RBC est étudié par simulations d'un grand nombre de RBCs circulant dans un réseau structuré comme un nid d'abeilles. Nos résultats suggèrent que la déformabilité de RBC doit être prise en considération et analysée avec soin afin d'avoir une bonne compréhension de la perfusion du sang et du transit de RBC en microcirculation. Les résultats de nos travaux actuels fournissent un fondement utile, nécessaire pour identifier les diverses propriétés des RBCs qui régissent la perfusion sanguine, et par là même mieux comprendre les problèmes d'acheminement de l'oxygène en microcirculation en général. Les résultats revêtent également une

certaine importance vis-à-vis d'applications pratiques, telles que le tri cellulaire et l'analyse chimique.

Il reste cependant beaucoup à faire, comme commenté succinctement ci-après.

- Étant donné que nos résultats numériques et expérimentaux sur la partition d'hématocrite dans le hémodilution contrastent avec la conviction commune, ceci suggère une révision des modèles actuels continus en vue de capturer cet effet. Cependant, il n'est pas clair s'il existe des modèles continues adéquats pour des situations où la nature discrète du sang est bien prononcée. Avant d'entreprendre ce travail, il sera d'abord utile de se pencher sur une simulation 3D afin d'obtenir une comparaison plus quantitative directe avec les expériences.

- Une étude systématique concernant l'influence de la structure de réseau sur la distribution de RBC sera à prendre en considération. En premier lieu, il sera important de relier la topologie du réseau à la qualité de la perfusion. Deuxièmement, il sera d'une grande importance de pouvoir disposer d'images médicales numérisées et utilisés afin de modéliser les réseaux vasculaires réels, en vue d'accompagner des études médicales.

References

M. Abkarian, C. Lartigue, and A. Viallat. Tank treading and unbinding of deformable vesicles in shear flow: determination of the lift force. *Phys. Rev. Lett.*, 88(6):068103, 2002. 41

M. Abkarian, M. Faivre, and A. Viallat. Swinging of red blood cells under shear flow. *Phys. Rev. Lett.*, 98(18):188302, 2007. 3, 41, 74, 87

B. J. Ackerson and P. N. Pusey. Shear-induced order in suspensions of hard spheres. *Phys. Rev. Lett.*, 61(8):1033, 1988. 61

J. K. Armstrong, R. B. Wenby, H. J. Meiselman, and T. C. Fisher. The hydrodynamic radii of macromolecules and their effect on red blood cell aggregation. *Biophys. J.*, 87(6):4259–70, Dec 2004. 4

D. M. Audet and W. L. Olbricht. The motion of model cells at capillary bifurcations. *Microvasc. Res.*, 33:377–396, 1987. 73

P. Bagchi and R. M. Kalluri. Dynamics of nonspherical capsules in shear flow. *Phys. Rev. E*, 80(1):016307, 2009. 41

P. Bagchi and R. M. Kalluri. Rheology of a dilute suspension of liquid-filled elastic capsules. *Phys. Rev. E*, 81(5):056320, 2010. 41

P. Bagchi and R. M. Kalluri. Dynamic rheology of a dilute suspension of elastic capsules: effect of capsule tank-treading, swinging and tumbling. *J. Fluid Mech.*, 669:498–526, 2011. 41

J. H. Barbee and G. R. Cokelet. The fahraeus effect. *Microvasc. Res.*, 3(1):6–16, 1971. 9, 41, 87

K. A. Barbee, P. F. Davies, and R. Lal. Shear stress-induced reorganization of the surface topography of living endothelial cells imaged by atomic force microscopy. *Circ. Res.*, 74(1):163–171, 1994. 8

J. O. Barber, J. P. Alberding, J. M. Restrepo, and T. W. Secomb. Simulated two-dimensional red blood cell motion, deformation, and partitioning in microvessel bifurcations. *Ann. Biomech. Eng.*, 36:1690–1698, 2008. 73

M. Baron, J. Bławzdziewicz, and E. Wajnryb. Hydrodynamic crystals: Collective dynamics of regular arrays of spherical particles in a parallel-wall channel. *Phys. Rev. Lett.*, 100(17):174502, 2008. 61

D. Barthès-Biesel. Motion and deformation of elastic capsules and vesicles in flow. *Annu. Rev. Fluid Mech.*, 48:25–52, 2016. 41

T. Beatus, T. Tlusty, and R. Bar-Ziv. Phonons in a one-dimensional microfluidic crystal. *Nat. Phys.*, 2(11):743–748, 2006. 61

T. Beatus, R. Bar-Ziv, and T. Tlusty. Anomalous microfluidic phonons induced by the interplay of hydrodynamic screening and incompressibility. *Phys. Rev. Lett.*, 99(12):124502, 2007. 61

S. Biagi, L. Rovigatti, F. Sciortino, and C. Misbah. Surface wave excitations and backflow effect over dense polymer brushes. *arXiv preprint arXiv:1501.06882*, 2015. 8

T. Biben and C. Misbah. Tumbling of vesicles under shear flow within an advected-field approach. *Phys. Rev. E*, 67(3):031908, 2003. 15

T. Biben, K. Kassner, and C. Misbah. Phase-field approach to three-dimensional vesicle dynamics. *Phys. Rev. E*, 72(4):041921, 2005. 15

T. Biben, A. Farutin, and C. Misbah. Three-dimensional vesicles under shear flow: Numerical study of dynamics and phase diagram. *Phys. Rev. E*, 83(3):031921, 2011. 41

M. Bouzidi, M. Firdaouss, and P. Lallemand. Momentum transfer of a boltzmann-lattice fluid with boundaries. *Phys. Fluids*, 13:3452, 2001. 20

G. Breyiannis and C. Pozrikidis. Simple shear flow of suspensions of elastic capsules. *Theor. Comp. Fluid Dyn.*, 13(5):327–347, 2000. 41

M. Brust, O. Aouane, M. Thiébaud, D. Flormann, C. Verdier, L. Kaestner, M. W. Laschke, H. Selmi, A. Benyoussef, T. Podgorski, et al. The plasma protein fibrinogen stabilizes clusters of red blood cells in microcapillary flows. *Sci. Rep.*, 4, 2014. 4

R. Busse and I. Fleming. Regulation of endothelium-derived vasoactive autacoid production by hemodynamic forces. *Trends Pharmacol. Sci.*, 24(1):24–29, 2003. 8

N. Callens, C. Minetti, G. Coupier, M.-A. Mader, F. Dubois, C. Misbah, and T. Podgorski. Hydrodynamic lift of vesicles under shear flow in microgravity. *Europhys. Lett.*, 83:24002, 2008. 74, 87

I. Cantat and C. Misbah. Lift force and dynamical unbinding of adhering vesicles under shear flow. *Phys. Rev. Lett.*, 83(4):880, 1999a. 15, 41

I. Cantat and C. Misbah. Lift force and dynamical unbinding of adhering vesicles under shear flow. *Phys. Rev. Lett.*, 83:880–883, 1999b. 74, 87

S. Chen and G. D. Doolen. Lattice boltzmann method for fluid flows. *Annu. Rev. Fluid Mech.*, 30(1):329–364, 1998. 16, 18

S. Chen, D. Martinez, and R. Mei. On boundary conditions in lattice boltzmann methods. *Phys. Fluids*, 8:2527, 1996. 19

X. Cheng, X. Xu, S. A. Rice, A. R. Dinner, and I. Cohen. Assembly of vorticity-aligned hard-sphere colloidal strings in a simple shear flow. *Proc. Natl. Acad. Sci.*, 109(1):63–67, 2012. 61

S. Chien and L. A. Sung. Physicochemical basis and clinical implications of red cell aggregation. *Clin. Hemorheol*, 7:71–91, 1987. 3

S. Chien, C. D. Tvetenstrand, M. A. Epstein, and G. W. Schmid-Schonbein. Model studies on distributions of blood cells at microvascular bifurcations. *Am. J. Physiol. Heart Circ. Physiol.*, 248:H568–H576, 1985. 73

G. R. Cokelet and H. J. Meiselman. Rheological comparison of hemoglobin solutions and erythrocyte suspensions. *Science*, 162:275–377, 1968. 75

D. V. P. Cokkinos, C. Pantos, G. Heusch, and H. Taegtmeyer. *Myocardial ischemia: from mechanisms to therapeutic potentials*, volume 21. Springer Science & Business Media, 2006. 2, 72

G. Coupier, B. Kaoui, T. Podgorski, and C. Misbah. Noninertial lateral migration of vesicles in bounded Poiseuille flow. *Phys. Fluids*, 20(11):111702, 2008a. 41

G. Coupier, B. Kaoui, T. Podgorski, and C. Misbah. Noninertial lateral migration of vesicles in bounded Poiseuille flow. *Phys. Fluids*, 20:111702, 2008b. 74, 87

G. Danker and C. Misbah. Rheology of a dilute suspension of vesicles. *Phys. Rev. Lett.*, 98(8):088104, 2007. 41

M. Dao, C. T. Lim, and S. Suresh. Mechanics of the human red blood cell deformed by optical tweezers. *J. Mech. Phys. Solids*, 51(11):2259–2280, 2003. 6

W. M. Deen, M. J. Lazzara, and B. D. Myers. Structural determinants of glomerular permeability. *Am. J. Physiol.-Renal*, 281(4):F579–F596, 2001. 8

J. W. Dellimore, M. J. Dunlop, and P. B. Canham. Ratio of cells and plasma in blood flowing past branches in small plastic channels. *Am. J. Physiol. Heart Circ. Physiol.*, 244:H635–H643, 1983. 10, 73, 87

D. E. Discher, D. H. Boal, and S. K. Boey. Simulations of the erythrocyte cytoskeleton at large deformation. ii. micropipette aspiration. *Biophys. J.*, 75(3): 1584–1597, 1998. 6

R. Ditchfield and W. L. Olbricht. Effects of particle concentration on the partitioning of suspensions at small divergent bifurcations. *J. Biomech. Eng.*, 118:287–294, 1996. 73

S. K. Doddi and P. Bagchi. Effect of inertia on the hydrodynamic interaction between two liquid capsules in simple shear flow. *Int. J. Multiphas. Flow*, 34(4):375–392, 2008. 41, 42

V. Doyeux, Y. Guyot, V. Chabannes, C. Prud'Homme, M. Ismail, et al. Simulation of two phase flow using a level set method: Application to bubbles and vesicle dynamics. In *Fifth International Conference on Advanced COmputational Methods in ENgineering*, pages 1–10, 2011a. 15

V. Doyeux, T. Podgorski, S. Peponas, M. Ismail, and G. Coupier. Spheres in the vicinity of a bifurcation: elucidating the Zweifach-Fung effect. *J. Fluid Mech.*, 674:359, 2011b. 73

J. Dupire, M. Socol, and A. Viallat. Full dynamics of a red blood cell in shear flow. *Proc. Natl. Acad. Sci.*, 109(51):20808–20813, 2012. 74, 87

E. C. Eckstein, D. G. Bailey, and A. H. Shapiro. Self-diffusion of particles in shear flow of a suspension. *J. Fluid Mech.*, 79(01):191–208, 1977. 60

C. D. Eggleton and A. S. Popel. Large deformation of red blood cell ghosts in a simple shear flow. *Phys. Fluids*, 10:1834, 1998. 16

E. A. Evans. Bending elastic modulus of red blood cell membrane derived from buckling instability in micropipet aspiration tests. *Biophys. J.*, 43(1):27, 1983. 6

E. A. Evans and R. M. Hochmuth. Membrane viscoelasticity. *Biophys. J.*, 16(1): 1–11, 1976. 6

A. Farutin and C. Misbah. Symmetry breaking of vesicle shapes in poiseuille flow. *Phys. Rev. E*, 84(1):011902, 2011. 15

A. Farutin and C. Misbah. Squaring, parity breaking, and s tumbling of vesicles under shear flow. *Phys. Rev. Lett.*, 109(24):248106, 2012. 6, 15, 43

A. Farutin and C. Misbah. Analytical and numerical study of three main migration laws for vesicles under flow. *Phys. Rev. Lett.*, 110(10):108104, 2013. 15, 41

A. Farutin and C. Misbah. Symmetry breaking and cross-streamline migration of three-dimensional vesicles in an axial poiseuille flow. *Phys. Rev. E*, 89(4):042709, 2014. 15, 74, 87

D. A. Fedosov, B. Caswell, S. Suresh, and G. E. Karniadakis. Quantifying the biophysical characteristics of plasmodium-falciparum-parasitized red blood cells in microcirculation. *Proc. Natl. Acad. Sci.*, 108(1):35–39, 2011a. 72

D. A. Fedosov, W. Pan, B. Caswell, G. Gompper, and G. E. Karniadakis. Predicting human blood viscosity in silico. *Proc. Natl. Acad. Sci.*, 108(29):11772–11777, 2011b. 14

D. A. Fedosov, H. Noguchi, and G. Gompper. Multiscale modeling of blood flow: from single cells to blood rheology. *Biomech. Model Mechanobiol.*, 13(2):239–258, 2014. 41

B. M. Fenton, R. T. Carr, and G. R. Cokelet. Nonuniform red cell distribution in 20 to 100 μm bifurcations. *Microvasc. Res.*, 29:103–126, 1985. 10, 73, 87

T. M. Fischer, M. Stohr-Lissen, and H. Schmid-Schonbein. The red cell as a fluid droplet: tank tread-like motion of the human erythrocyte membrane in shear flow. *Science*, 202(4370):894–896, 1978. 3, 41

U. Frisch, B. Hasslacher, and Y. Pomeau. Lattice-gas automata for the navier-stokes equation. *Phys. Rev. Lett.*, 56(14):1505, 1986. 16

W. F. M. Fulton. Immersion radiography of injected specimens. *Brit. J. Radiol.*, 36 (429):685–688, 1963. viii, 7

Y.-C. Fung. *Biomechanics: circulation*. Springer Science & Business Media, 2013. 41, 78

G. Ghigliotti, H. Selmi, B. Kaoui, G. Biros, and C. Misbah. Dynamics and rheology of highly deflated vesicles. In *Esaim: proceedings*, volume 28, pages 211–226. EDP Sciences, 2009. 15

G. Ghigliotti, T. Biben, and C. Misbah. Rheology of a dilute two-dimensional suspension of vesicles. *J. Fluid Mech.*, 653:489–518, April 2010. 15, 38, 41

G. Ghigliotti, H. Selmi, L. El Asmi, and C. Misbah. Why and how does collective red blood cells motion occur in the blood microcirculation? *Phys. Fluids*, 24: 101901, 2012. 15

I. Ginzbourg and P. M. Adler. Boundary flow condition analysis for the three-dimensional lattice boltzmann model. *J. Phys. II*, 4(2):191–214, 1994. 20

P.-Y. Gires, A. Srivastav, C. Misbah, T. Podgorski, and G. Coupier. Pairwise hydrodynamic interactions and diffusion in a vesicle suspension. *Phys. Fluids (1994-present)*, 26(1):013304, 2014. 41, 42

G. Gompper and M. Schick. *Soft Matter: Volume 4-Lipid Bilayers and Red Blood Cells*, volume 4. Wiley-VCH, 2008. 6

Y. Goto and H. Tanaka. Purely hydrodynamic ordering of rotating disks at a finite reynolds number. *Nat. Commun.*, 6, 2015. 61

X. Grandchamp, G. Coupier, A. Srivastav, C. Minetti, and T. Podgorski. Lift and down-gradient shear-induced diffusion in red blood cell suspensions. *Phys. Rev. Lett.*, 110(10):108101, 2013. 41, 74, 78, 87

R. Guibert, C. Fonta, and F. Plouraboue. A New Approach to Model Confined Suspensions Flows in Complex Networks: Application to Blood Flow. *Transport Porous Med.*, 83:171–194, 2010. 10, 73, 87

Z. Guo, C. Zheng, and B. Shi. Discrete lattice effects on the forcing term in the lattice Boltzmann method. *Phys. Rev. E*, 65(4):046308, April 2002. 18

D. S. Hariprasad and T. W. Secomb. Two-dimensional simulation of red blood cell motion near a wall under a lateral force. *Phys. Rev. E*, 90:053014, 2014. 74, 87

Xiaoyi He, Qisu Zou, Li-Shi Luo, and Micah Dembo. Analytic solutions of simple flows and analysis of nonslip boundary conditions for the lattice boltzmann bgk model. *J. Stat. Phys.*, 87(1-2):115–136, 1997. 20, 22

D. J. Holdych, D. R. Noble, J. G. Georgiadis, and R. O. Buckius. Truncation error analysis of lattice boltzmann methods. *J. Comput. Phys.*, 193(2):595–619, 2004. 22

Y. Huang, C. M. Doerschuk, and R. D. Kamm. Computational modeling of rbc and neutrophil transit through the pulmonary capillaries. *J. Appl. Physiol.*, 90 (2):545–564, 2001. 11

K. J. Humphry, P. M. Kulkarni, D. A. Weitz, J. F. Morris, and H. A. Stone. Axial and lateral particle ordering in finite reynolds number channel flows. *Phys. Fluids (1994-present)*, 22(8):081703, 2010. 61

T. Hyakutake and S. Nagai. Numerical simulation of red blood cell distributions in three-dimensional microvascular bifurcations. *Microvasc. Res.*, 97:115 – 123, 2015. 73

P. J. A. Janssen, M. D. Baron, P. D. Anderson, J. Blawzdziewicz, M. Loewenberg, and E. Wajnryb. Collective dynamics of confined rigid spheres and deformable drops. *Soft Matter*, 8(28):7495–7506, 2012. 61

V. Kantsler and V. Steinberg. Transition to tumbling and two regimes of tumbling motion of a vesicle in shear flow. *Phys. Rev. Lett.*, 96(3):036001, 2006. 3, 41

B. Kaoui, G. Biros, and C. Misbah. Why do red blood cells have asymmetric shapes even in a symmetric flow? *Phys. Rev. Lett.*, 103(18):188101, 2009a. 15

B. Kaoui, A. Farutin, and C. Misbah. Vesicles under simple shear flow: Elucidating the role of relevant control parameters. *Phys. Rev. E*, 80(6):061905, 2009b. 15, 38

B. Kaoui, J. Harting, and C. Misbah. Two-dimensional vesicle dynamics under shear flow: Effect of confinement. *Phys. Rev. E*, 83(6):066319, 2011. 24, 41

B. Kaoui, T. Krüger, and J. Harting. How does confinement affect the dynamics of viscous vesicles and red blood cells? *Soft Matter*, 8(35):9246–9252, 2012. 41

B. Kaoui, R. J. W. Jonk, and J. Harting. Interplay between microdynamics and macrorheology in vesicle suspensions. *Soft Matter*, 10(26):4735–4742, 2014. 41

D. Katanov, G. Gompper, and D. A. Fedosov. Microvascular blood flow resistance: Role of red blood cell migration and dispersion. *Microvasc. Res.*, 99:57–66, 2015. 74, 87

C. Kelemen, S. Chien, and G. M. Artmann. Temperature transition of human hemoglobin at body temperature: effects of calcium. *Biophys. J.*, 80(6):2622–2630, 2001. 63, 75

S. R. Keller and R. Skalak. Motion of a tank-treading ellipsoidal particle in a shear flow. *J. Fluid Mech.*, 120:27–47, 1982. 3, 40

Y. Kim, K. Kim, and Y. Park. *Measurement techniques for red blood cell deformability: recent advances*. INTECH Open Access Publisher, 2012. viii, 6

M. Kraus, W. Wintz, U. Seifert, and R. Lipowsky. Fluid vesicles in shear flow. *Phys. Rev. Lett.*, 77(17):3685, 1996. 3, 40

I. M. Krieger and T. J. Dougherty. A mechanism for non-newtonian flow in suspensions of rigid spheres. *Trans. Soc. Rheol*, 3(1):137–152, 1959. 56

T. Krüger. *Computer simulation study of collective phenomena in dense suspensions of red blood cells under shear*. Springer, 2012. 16, 18, 22, 26, 33, 62

T. Krüger, F. Varnik, and D. Raabe. Shear stress in lattice boltzmann simulations. *Phys. Rev. E*, 79(4):046704, 2009. 56

T. Krüger, B. Kaoui, and J. Harting. Interplay of inertia and deformability on rheological properties of a suspension of capsules. *J. Fluid Mech.*, 751:725–745, 2014. 74, 87

A. Kumar, R. G. Henríquez Rivera, and M. D. Graham. Flow-induced segregation in confined multicomponent suspensions: effects of particle size and rigidity. *J. Fluid Mech.*, 738:423–462, 1 2014. xiii, 81

E. Lac, A. Morel, D. Barthes-Biesel, et al. Hydrodynamic interaction between two identical capsules in simple shear flow. *J. Fluid Mech.*, 573(1):149–169, 2007. 41, 42

A. Lamura and G. Gompper. Dynamics and rheology of vesicle suspensions in wall-bounded shear flow. *EPL (Europhys. Lett.)*, 102(2):28004, 2013. 41

L. Lanotte, S. Guido, C. Misbah, P. Peyla, and L. Bureau. Flow reduction in microchannels coated with a polymer brush. *Langmuir*, 28(38):13758–13764, 2012. 8

L. Lanotte, G. Tomaiuolo, C. Misbah, L. Bureau, and S. Guido. Red blood cell dynamics in polymer brush-coated microcapillaries: A model of endothelial glycocalyx in vitro. *Biomicrofluidics*, 8(1):014104, 2014. 8

D.-V. Le and K.-H. Chiam. Hydrodynamic interaction between two nonspherical capsules in shear flow. *Phys. Rev. E*, 84(5):056322, 2011. 41, 42

W. Lee, H. Amini, H. A. Stone, and D. Di Carlo. Dynamic self-assembly and control of microfluidic particle crystals. *Proc. Natl. Acad. Sci.*, 107(52):22413–22418, 2010. 61

J. Li, M. Dao, C. T. Lim, and S. Suresh. Spectrin-level modeling of the cytoskeleton and optical tweezers stretching of the erythrocyte. *Biophys. J.*, 88(5):3707–3719, 2005. 6

J. Li, G. Lykotrafitis, M. Dao, and S. Suresh. Cytoskeletal dynamics of human erythrocyte. *Proc. Natl. Acad. Sci.*, 104(12):4937–4942, 2007. 6

X. Li, A. S. Popel, and G. E. Karniadakis. Blood-plasma separation in y-shaped bifurcating microfluidic channels: a dissipative particle dynamics simulation study. *Phys. Biol.*, 9:026010, 2012. 73

S.-C. Liu, L. H. Derick, and J. Palek. Visualization of the hexagonal lattice in the erythrocyte membrane skeleton. *J. Cell Biol.*, 104(3):527–536, 1987. 6

Y. Liu, L. Zhang, X. Wang, and W. Liu. Coupling of navier–stokes equations with protein molecular dynamics and its application to hemodynamics. *Int. J. Numer. Meth. Fl.*, 46(12):1237–1252, 2004. 27

S. Lorthois and F. Cassot. Fractal analysis of vascular networks: insights from morphogenesis. *J. Theor. Biol.*, 262(4):614–633, 2010. 2

S. Lorthois, F. Cassot, and F. Lauwers. Simulation study of brain blood flow regulation by intra-cortical arterioles in an anatomically accurate large human vascular network. part ii: flow variations induced by global or localized modifications of arteriolar diameters. *Neuroimage*, 54(4):2840–2853, 2011. 11

M.-A. Mader, V. Vitkova, M. Abkarian, A. Viallat, and T. Podgorski. Dynamics of viscous vesicles in shear flow. *Eur. Phys. J. E*, 19(4):389–397, 2006. 41

J. L. McWhirter, H. Noguchi, and G. Gompper. Flow-induced clustering and alignment of vesicles and red blood cells in microcapillaries. *Proc. Natl. Acad. Sci.*, 106(15):6039–6043, 2009. 14, 74, 87

R. Mei, L. Luo, P. Lallemand, and D. d'Humières. Consistent initial conditions for lattice boltzmann simulations. *Comput. Fluids*, 35(8):855–862, 2006. 22

B. Metzger, P. Pham, and J. E. Butler. Irreversibility and chaos: Role of lubrication interactions in sheared suspensions. *Phys. Rev. E*, 87(5):052304, 2013a. 60

B. Metzger, O. Rahli, and X. Yin. Heat transfer across sheared suspensions: role of the shear-induced diffusion. *J. Fluid Mech.*, 724:527–552, 2013b. 60

C. Misbah. Vacillating breathing and tumbling of vesicles under shear flow. *Phys. Rev. Lett.*, 96(2):028104, 2006. 3, 40, 55

J. A. Nagy, L. Benjamin, H. Zeng, A. M. Dvorak, and H. F. Dvorak. Vascular permeability, vascular hyperpermeability and angiogenesis. *Angiogenesis*, 11(2): 109–119, 2008. 8

A. Narváez, T. Zauner, F. Raischel, R. Hilfer, and J. Harting. Quantitative analysis of numerical estimates for the permeability of porous media from lattice-boltzmann simulations. *J. Stat. Mech.-Theory E.*, 2010(11):P11026, 2010. 23

B. Neu and H. J. Meiselman. Depletion-mediated red blood cell aggregation in polymer solutions. *Biophys. J.*, 83(5):2482–2490, 2002. 4

H. Noguchi and G. Gompper. Fluid vesicles with viscous membranes in shear flow. *Phys. Rev. Lett.*, 93(25):258102, 2004. 3, 14, 40

H. Noguchi and G. Gompper. Shape transitions of fluid vesicles and red blood cells in capillary flows. *Proc. Natl. Acad. Sci. of the United States of America*, 102(40): 14159–14164, 2005. 14

H. Noguchi and G. Gompper. Swinging and tumbling of fluid vesicles in shear flow. *Phys. Rev. Lett.*, 98(12):128103, 2007. 3, 14, 40

U. Olgac and V. Kurtcuoglu. Renal oxygenation: preglomerular vasculature is an unlikely contributor to renal oxygen shunting. *Am. J. Physiol.-Renal*, 308(7): F671–F688, 2015. 11

S. T. T. Ollila, C. Denniston, and T. Ala-Nissila. One- and two-particle dynamics in microfluidic t-junctions. *Phys. Rev. E*, 87:050302, 2013. 73

R. Pal. Rheology of concentrated suspensions of deformable elastic particles such as human erythrocytes. *J. Biomech.*, 36(7):981–989, 2003. xi, 54

Y. K. Park, C. A. Best, T. Auth, N. S. Gov, S. A. Safran, G. Popescu, S. Suresh, and M. S. Feld. Metabolic remodeling of the human red blood cell membrane. *Proc. Natl. Acad. Sci.*, 107(4):1289–1294, 2010. 6

Z. Peng, X. Li, I. V. Pivkin, M. Dao, G. E. Karniadakis, and S. Suresh. Lipid bilayer and cytoskeletal interactions in a red blood cell. *Proc. Natl. Acad. Sci.*, 110(33): 13356–13361, 2013. 6

C. S. Peskin. Numerical analysis of blood flow in the heart. *J. Comput. Phys.*, 25 (3):220–252, 1977. 15

C. S. Peskin. The immersed boundary method. *Acta numer.*, 11(0):479–517, 2002. 24, 26

D. J. Pine, J. P. Gollub, J. F. Brady, and A. M. Leshansky. Chaos and threshold for irreversibility in sheared suspensions. *Nature*, 438(7070):997–1000, 2005. 60

I. V. Pivkin and G. E. Karniadakis. Accurate coarse-grained modeling of red blood cells. *Phys. Rev. Lett.*, 101(11):118105, 2008. 14

A. S. Popel and P. C. Johnson. Microcirculation and hemorheology. *Annu. Rev. Fluid Mech.*, 37:43, 2005. 3, 8, 9, 87

C. Pozrikidis. *Boundary integral and singularity methods for linearized viscous flow.* Cambridge University Press, 1992. 15

C. Pozrikidis. Finite deformation of liquid capsules enclosed by elastic membranes in simple shear flow. *J. Fluid Mech.*, 297:123–152, 1995. 15

C. Pozrikidis. Numerical Simulation of the Flow-Induced Deformation of Red Blood Cells. *Ann. Biomed. Eng.*, 31(10):1194–1205, November 2003. 41

G. Prado, A. Farutin, C. Misbah, and L. Bureau. Viscoelastic transient of confined red blood cells. *Biophys. J.*, 108(9):2126–2136, 2015. 6

A. R. Pries and T. W. Secomb. Rheology of the microcirculation. *Clin. Hemorheol. Micro.*, 29(3):143–148, 2003. 41

A. R. Pries, K. Ley, M. Claassen, and P. Gaethgens. Red cell distribution at microvascular bifurcations. *Microvasc. Res.*, 38:81–101, 1989. 10, 73, 76, 87

A. R. Pries, T. W. Secomb, P. Gaehtgens, and J. F. Gross. Blood flow in microvascular networks. experiments and simulation. *Circ. Res.*, 67(4):826–34, 1990. xiii, xiv, 11, 76, 79, 82, 83, 84, 87

A. R. Pries, D. Neuhaus, and P. Gaehtgens. Blood viscosity in tube flow: dependence on diameter and hematocrit. *Am. J. Physiol.*, 263(6 Pt 2):H1770–8, Dec 1992. viii, 9, 10, 87

A. R. Pries, T. W. Secomb, T. Gessner, M. B. Sperandio, J. F. Gross, and P. Gaehtgens. Resistance to blood flow in microvessels in vivo. *Circ. Res.*, 75(5):904–915, 1994. 10, 41

C. Quéguiner and D. Barthès-Biesel. Axisymmetric motion of capsules through cylindrical channels. *J. Fluid Mech.*, 348:349–376, 1997. 15

B. W. Roberts and W. L. Olbricht. Flow-induced particulate separations. *AIChE J.*, 49:2842–2849, 2003. 73

B. W. Roberts and W. L. Olbricht. The distribution of freely suspended particles at microfluidic bifurcations. *AIChE J.*, 52:199–206, 2006. 73

P. Schall, D. A. Weitz, and F. Spaepen. Structural rearrangements that govern flow in colloidal glasses. *Science*, 318(5858):1895–1899, 2007. 61

L. Scheffer, A. Bitler, E. Ben-Jacob, and R. Korenstein. Atomic force pulling: probing the local elasticity of the cell membrane. *Eur. Biophys. J.*, 30(2):83–90, 2001. 6

H. Schmid-Schönbein and R. Wells. Fluid drop-like transition of erythrocytes under shear. *Science*, 165(3890):288–291, 1969. 6

U. Seifert. Configurations of fluid membranes and vesicles. *Adv. Phys.*, 46(1):13–137, 1997. 41

U. Seifert. Hydrodynamic lift on bound vesicles. *Phys. Rev. Lett.*, 83(4):876, 1999. 41

X. Shan and G. Doolen. Diffusion in a multicomponent lattice boltzmann equation model. *Phys. Rev. E*, 54(4):3614, 1996. 16

I. Shani, T. Beatus, R. H. Bar-Ziv, and T. Tlusty. Long-range orientational order in two-dimensional microfluidic dipoles. *Nat. Phys.*, 10(2):140–144, 2014. 61

Z. Shen, G. Coupier, B. Kaoui, B. Polack, J. Harting, C. Misbah, and T. Podgorski. Inversion of hematocrit partition at microfluidic bifurcations. *Microvasc. Res.*, 105:40–46, 2016. 88

J. M. Sherwood, E. Kaliviotis, J. Dusting, and S. Balabani. Hematocrit, viscosity and velocity distributions of aggregating and non-aggregating blood in bifurcating microchannel. *Biomicrofluidics*, 6:024119, 2012. 73

L. Shi, T. W. Pan, and R. Glowinski. Numerical simulation of lateral migration of red blood cells in poiseuille flows. *Int. J. Numer. Methods Fluids*, 68(11): 1393–1408, 2012. 74, 87

R. Skalak, S. Chien, and R. Mates. Handbook of bioengineering, 1987. 6

P. A. Skordos. Initial and boundary conditions for the lattice boltzmann method. *Phys. Rev. E*, 48(6):4823, 1993. 22

J. M. Skotheim and T. W. Secomb. Red blood cells and other nonspherical capsules in shear flow: oscillatory dynamics and the tank-treading-to-tumbling transition. *Phys. Rev. Lett.*, 98(7):078301, 2007. 3, 40

S. Succi. *The lattice Boltzmann equation: for fluid dynamics and beyond*. Oxford university press, 2001. 22

M. H.-Y. Tan, D.-V. Le, and K.-H. Chiam. Hydrodynamic diffusion of a suspension of elastic capsules in bounded simple shear flow. *Soft Matter*, 8(7):2243–2251, 2012. 41

G. I. Taylor. The formation of emulsions in definable fields of flow. *Proc. R. Soc. Lond. A Math. Phys. Sci.*, pages 501–523, 1934. 55

M. Thiébaud and C. Misbah. Rheology of a vesicle suspension with finite concentration: A numerical study. *Phys. Rev. E*, 88(6):062707, 2013. 15

M. Thiébaud, Z. Shen, J. Harting, and C. Misbah. Prediction of Anomalous Blood Viscosity in Confined Shear Flow. *Phys. Rev. Lett.*, 112(23):238304, June 2014. 15, 41

R. Trozzo, G. Boedec, M. Leonetti, and M. Jaeger. Axisymmetric boundary element method for vesicles in a capillary. *J. Comput. Phys.*, 289:62–82, 2015. 15

K. Tsubota and S. Wada. Effect of the natural state of an elastic cellular membrane on tank-treading and tumbling motions of a single red blood cell. *Phys. Rev. E*, 81(1):011910, 2010. 28

K. Tsubota, S. Wada, and T. Yamaguchi. Particle method for computer simulation of red blood cell motion in blood flow. *Comput. Meth. Prog. Bio.*, 83(2):139–146, 2006. 28

S. K. Veerapaneni, D. Gueyffier, D. Zorin, and G. Biros. A boundary integral method for simulating the dynamics of inextensible vesicles suspended in a viscous fluid in 2d. *J. Comput. Phys.*, 228(7):2334–2353, 2009. 15

D. Vincent, C. Vincent, C. Prud'homme, and M. Ismail. Simulation of vesicle using level set method solved by high order finite element. In *ESAIM: Proceedings*, volume 38, 2012. 15

P. M. Vlahovska, T. Podgorski, and C. Misbah. Vesicles and red blood cells in flow: From individual dynamics to rheology. *C. R. Phys.*, 10(8):775–789, 2009. 41

R. E. Waugh and R. M. Hochmuth. Mechanics and deformability of hematocytes. *The biomedical engineering handbook*, 35:474–486, 1995. 6

D. Wolf-Gladrow. A lattice boltzmann equation for diffusion. *J. Stat. Phys.*, 79 (5-6):1023–1032, 1995. 16

S. Wolfram et al. *Theory and applications of cellular automata*, volume 1. World scientific Singapore, 1986. 16

H. C. Woolfenden and M. G. Blyth. Motion of a two-dimensional elastic capsule in a branching channel flow. *J. Fluid Mech.*, 669:3–31, 2 2011. 73

Y. Wu, D. Derks, A. van Blaaderen, and A. Imhof. Melting and crystallization of colloidal hard-sphere suspensions under shear. *Proc. Natl. Acad. Sci.*, 106(26): 10564–10569, 2009. 61

W. Xiong and J. Zhang. Two-dimensional lattice boltzmann study of red blood cell motion through microvascular bifurcation: cell deformability and suspending viscosity effects. *Biomech. Model. Mechanobiol.*, 11:575–583, 2012. 73

X. Yang, X. Zhang, Z. Li, and G. He. A smoothing technique for discrete delta functions with application to immersed boundary method in moving boundary simulations. *J. Comput. Phys.*, 228(20):7821–7836, 2009. 25

X. Yin, T. Thomas, and J. Zhang. Multiple red blood cell flows through microvascular bifurcations: Cell free layer, cell trajectory, and hematocrit separation. *Microvasc. Res.*, 89:47 – 56, 2013. 73, 82

J. Zhang, P. C. Johnson, and A. S. Popel. An immersed boundary lattice boltzmann approach to simulate deformable liquid capsules and its application to microscopic blood flows. *Phys. Biol.*, 4(4):285, 2007. 16, 24

H. Zhao and E. S. G. Shaqfeh. The dynamics of a non-dilute vesicle suspension in a simple shear flow. *J. Fluid Mech.*, 725:709–731, 2013. 41

H. Zhao, A. H. G. Isfahani, L. N. Olson, and J. B. Freund. A spectral boundary integral method for flowing blood cells. *J. Comput. Phys.*, 229(10):3726–3744, 2010. 15

Q. Zou and X. He. On pressure and velocity boundary conditions for the lattice boltzmann bgk model. *Phys. Fluids*, 9:1591, 1997. 20, 21

Summary

Dynamics and rheology of a 2D confined suspension of vesicles (a model for RBCs) is studied numerically by using an immersed boundary-lattice Boltzmann method (IB-LBM). We pay special attention to the link between the spatiotemporal organization of the suspension and rheology. We first analyze situations in which vesicles perform tank-treading. The pair of vesicles settles into an equilibrium state with constant relative distance, which is regulated by the confinement. The equilibrium distance increases with the gap between walls following a linear relationship. However, no stable equilibrium distance between two tumbling vesicles is observed. The presence or the lack thereof of an equilibrium distance between two vesicles dictates the spatiotemporal organization of the suspension (order or disorder). Ordering of the suspension is accompanied with quite ample oscillation of normalized viscosity as a function of concentration, while the effective viscosity exhibits plateau. The amplitude of oscillations of normalized viscosity is suppressed when disordered pattern prevails.

Besides the interactions in the shear plane discussed in 2D framework, the interactions in the vertical direction to the shear plane are also analyzed by 3D simulations of capsules (a model for RBCs) and experiments. We show that in a confined blood suspension, RBCs spontaneously organize in a crystalline-like structure under the sole effect of hydrodynamic interaction. It is further shown that when RBCs are substituted by rigid particles, order disappears in favor of disorder. Various crystalline orders take place depending on concentration and confinement. The intercellular distance of the crystalline structure is a linear function of confinement. Order appears as a subtle interplay between the lift force that pushes RBCs away from walls towards the center and hydrodynamic interactions in the vertical of shear flow plane. This study introduces a new paradigm in the field of dilute non-colloidal suspensions where the prevalence of disorder was up-to date the rule.

The partition of RBCs at the level of bifurcations is addressed in our computer simulations and in vitro experiments, which reveal that the hematocrit partition strongly depends on the viscosity contrast between the viscosities of the RBC hemoglobin and the suspending fluid, as long

as hematocrit is less than 20% (which is the normal range in microcirculation). In the extreme hemodilution, our results exhibit a new phenomenon: the low flow rate branch may receive higher hematocrit than the high flow rate branch, in opposition to the well-known Zweifach-Fung effect. This phenomenon is observed under moderate confinement and is the result of a peculiar structuring of the cell suspension. Our findings suggest that the various RBCs properties must be taken into consideration and carefully analyzed in order to have a firm understanding of RBC distribution in microcirculation and thus oxygen delivery in the microcirculation in general.

Finally, we carry out numerical simulations of a large number of RBCs flowing in a network that is structured in a honeycomb pattern. Our results reveal that as long as the hematocrit is less than 20% the RBCs with higher membrane rigidity show a larger lateral displacement in the network. Furthermore, we discover a deviation of RBC flux in network from that in straight tube where the more rigid RBCs get the smaller flux. Oppositely, the larger RBC flux is observed for the more rigid RBCs in the network. Finally, we report on the manifestation of a faster longitudinal diffusion of crowded RBCs with smaller deformability in the network. Our results provide interesting information on the RBC delivery in the network, which should be significant not only in the understanding of the blood perfusion and the RBC transit in the microcirculation but also in practical applications such as cell sorting and chemical analysis.

Sommaire

La dynamique et la rhéologie d'une suspension 2D confinée de vésicules (un modèle de RBCs (globules rouges)) sont étudiées numériquement en utilisant une méthode de Boltzmann sur réseau frontière immergée (IB-LBM). Nous portons une attention particulière au lien entre l'organisation spatio-temporelle de la suspension et la rhéologie. Nous analysons d'abord les situations dans lesquelles les vésicules effectuent le mouvement de chenille de char. Des paires de vésicules se placent dans un état d'équilibre avec une distance relative constante et régulée par le confinement. La distance d'équilibre augmente avec l'intervalle entre les parois suivant une relation linéaire. Cependant, aucune distance d'équilibre stable entre deux vésicules en mouvement de tumbling n'est observée. La présence ou l'absence d'une distance d'équilibre entre deux vésicules dicte l'organisation spatio-temporelle de la suspension (ordre ou désordre). L'organisation de la suspension s'accompagne d'assez amples oscillations de la viscosité normalisée variant en fonction de la concentration, tandis que la viscosité effective ne varie pas. Les amplitudes d'oscillation de la viscosité normalisée sont supprimées lorsque le motif désordonné prévaut.

En plus des interactions dans le plan de cisaillement décrites en 2D, les interactions dans la direction verticale par rapport au plan de cisaillement sont également analysées par des simulations en 3D de capsules (un modèle de RBCs) et des expériences. Nous montrons que dans une suspension confinée de sang, les RBCs s'organisent spontanément en une structure cristalline sous le seul effet de l'interaction hydrodynamique. Il est en outre démontré que lorsque les RBCs sont remplacés par des particules rigides, l'ordre disparait pour laisser place au désordre. Différents ordres cristallins peuvent apparaître selon la concentration et le confinement. La distance intercellulaire de la structure cristalline est une fonction linéaire du confinement. L'ordre apparaît comme une interaction subtile entre la force de portance qui pousse les RBCs des murs vers le centre et l'interaction hydrodynamique dans la verticale du plan d'écoulement de cisaillement. Cette étude introduit un nouveau paradigme dans le domaine des suspensions non-colloïdales diluées où la prévalence des désordres était mise à jour la règle.

La répartition des RBCs au niveau d'une bifurcation est abordée dans nos simulations sur ordinateur ainsi que dans des expériences in vitro. Ces études révèlent que la répartition des globules rouges dépend fortement du contraste de viscosité entre la viscosité de l'hémoglobine du RBC et le fluide suspendant, tant que l'hématocrite est inférieure à 20% (ce qui est la gamme normale de la microcirculation). Pour des dilutions importantes, nos résultats montrent un nouveau phénomène : la branche de faible débit peut recevoir une concentration plus élevé que la branche de haut débit, en opposition à l'effet Zweifach-Fung. Ce phénomène est observé sous confinement modéré et est le résultat d'une structuration particulière de la suspension cellulaire. Nos résultats suggèrent que les différentes propriétés des RBCs doivent être prises en compte et soigneusement analysées afin d'avoir une bonne compréhension de la distribution de RBCs dans la microcirculation et donc de la livraison de l'oxygène dans la microcirculation en général.

Enfin, nous réalisons des simulations numériques d'une grande quantité de RBCs, circulant dans un réseau qui est structuré selon un motif en nid d'abeilles. Nos résultats montrent que tant que l'hématocrite est inférieure à 20%, les RBCs dont la membrane est plus rigide présentent un déplacement latéral plus important dans le réseau. En plus, nous découvrons une différence par rapport à la circulation de RBCs dans un tube droit où le débit pour des globules rigides est plus petit. Au contraire, un débit plus important est observé pour les RBCs plus rigides dans le réseau. Enfin, nous présentons la manifestation d'une diffusion longitudinale plus rapide d'une suspension dense de RBCs de faible déformabilité dans le réseau. Nos résultats fournissent des informations intéressantes sur la livraison de RBCs dans le réseau, ce qui pourrait être important non seulement sur la compréhension de la perfusion du sang et le transit de RBC dans la microcirculation, mais aussi sur des applications pratiques, comme le tri cellulaire. et l'analyse chimique.